Innovative Designs and Testing: A Comparative Study of SPARCS, STRUVE, and EXCITE Missions

by

Johnathan Roger Gamaunt

A Dissertation Presented in Partial Fulfillment
of the Requirements for the Degree
Doctor of Philosophy

Approved March 2024 by the
Graduate Supervisory Committee:

Paul Scowen, Co-Chair
Nathaniel Butler, Co-Chair
Alfred de Wijn
Christopher Groppi
Daniel Jacobs

ARIZONA STATE UNIVERSITY

May 2024

ABSTRACT

This dissertation explores the design, testing, and implementation of cutting-edge spaceborne instrumentation through the investigation of three distinct projects: SPARCS, STRUVE, and EXCITE. The SPARCS astrophysics project focuses on the development of a thermal vacuum chamber for testing contamination-sensitive hardware, alongside the design of ground support equipment (GSE) tailored to SPARCS' performance requirements. STRUVE, a heliophysics CubeSat mission concept, is examined for its mechanical and thermal design strategies, as well as thermal sensitivity studies crucial for mission success. The EXCITE project, an infrared spectrometer balloon-based astrophysics mission, is analyzed for its opto-mechanical design and comprehensive coefficient of thermal expansion (CTE) stress analysis. Throughout the dissertation, each project's challenges, innovations, and solutions are meticulously documented, providing insights into the intricacies and demands of space instrumentation design and testing. The introduction sets the stage by contextualizing the significance of spaceborne instrumentation projects and outlining the scope of the dissertation. The chapters present detailed examinations of SPARCS, STRUVE, and EXCITE, and discuss the engineering complexities and advancements achieved in each project. In conclusion, the dissertation reflects on the lessons learned, implications for future space missions, and the broader impact of SPARCS, STRUVE, and EXCITE on the field of spaceborne instrumentation. This research contributes to the ongoing discourse surrounding space technology innovation and underscores the importance of interdisciplinary collaboration in pushing the boundaries of space exploration.

TABLE OF CONTENTS

CHAPTER Page

LIST OF TABLES

LIST OF FIGURES

Figure Page

Figure Page

Figure Page

CHAPTER 1

EMBARKING ON THE JOURNEY: CONTEXTUALIZING SPARCS, STRUVE, AND EXCITE

Introduction

The dissertation adopts a systems-engineering approach, aligning with NASA's methodology, which emphasizes a multidisciplinary perspective to manage and coordinate technical aspects within complex engineering projects. This study involves three distinct projects, each engaged at different stages of their mission life cycles, which typically consist of seven phases as defined by NASA.

The first project, focusing on the Star-Planet Activity Research CubeSat (SPARCS), is in preparation of Phase D of the mission lifecycle, where assembly, integration, and testing activities take place. Here, the primary tasks involves designing a test apparatus and setting up test configurations to facilitate the thorough assembly and testing of the instrument.

The second project, centered around the Solar Transition Region UltraViolet Explorer (STRUVE), occurs during the Pre-Phase A stage, primarily serving as a concept study with the intent of advancing the project further. During this phase, proof-of-concept activities are undertaken, demonstrating the feasibility of integrating the payload into a CubeSat form factor. Additionally, a preliminary opto-mechanical design of the instrument is developed, alongside an assessment of the thermal environments to establish the viability of a stable thermal system.

The third project, concerning the EXoplanet Climate Infrared Telescope (EXCITE), spans across Phases B and C of the mission lifecycle. In these stages, the focus is on advancing the opto-mechanical design from its preliminary concept to a finalized version, supported by thorough analysis to ensure its robustness and effectiveness.

By engaging with these projects at various stages of their life cycles, this dissertation illustrates the practical application of systems-engineering principles in addressing the diverse challenges encountered across different phases of complex engineering endeavors within the realm of space exploration and research.

Star Planet Activity Research CubeSat (SPARCS)

SPARCS is a NASA-funded CubeSat mission looking to provide insight into the habitability of planets around M-dwarf stars. M-dwarfs are a common type of star found in the galaxy, 40 billion are expected to host at least one planet in the “habitable zone” (Ardila et al., 2018). M-dwarfs tend to be highly active in the ultraviolet (UV) region which negatively impacts the habitability of planets by leading to atmospheric loss. SPARCS objectives are to measure the short- and long-term variability of M-stars in the near ultraviolet (280 nm) and far ultraviolet (162 nm) wavelengths and flare frequency and energy (Ardila et al., 2018).

Figure 1.

Overview of the SPARCS Payload.

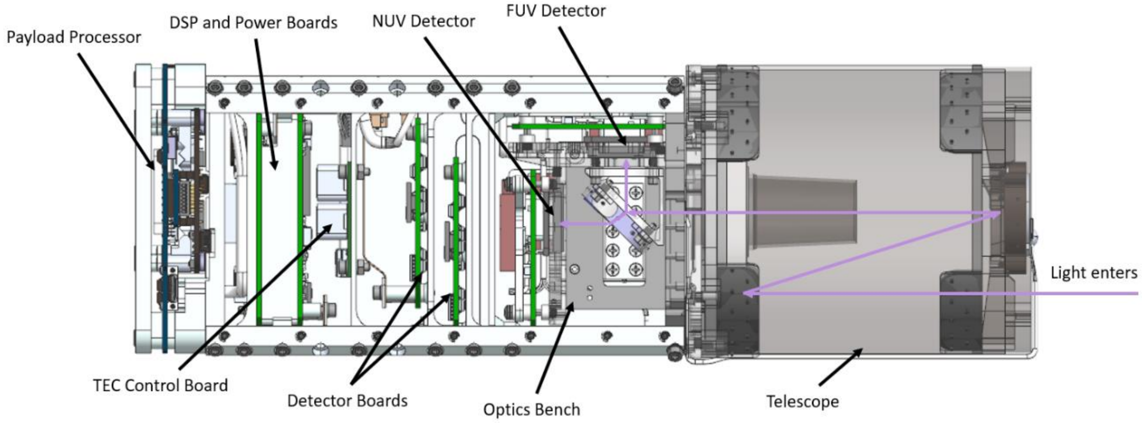

The SPARCS payload is a 3U photometer with a two-channel UV camera. Light enters the 9 cm Ritchey-Chrétien telescope and is passed into the optics bench where the light is split into two beams with the dichroic. The dichroic reflects the far ultraviolet (FUV) band to the FUV detector and passes the near ultraviolet (NUV) band to the NUV detector (Figure 1). The detectors are high-sensitivity UV 2D-doped detectors (Nikzad et al., 2012) and serve as the technology demonstration aspect of the mission. The sensors are actively cooled to -35°C for operation using a thermoelectric cooler (TEC). The two detectors have aluminum heat sinks bonded to the back of the detector packages which are then mechanically connected to thermal straps to create the thermal path from the detectors to the TEC. The TEC dissipates the excess heat to the dedicated payload radiator on the spacecraft which is then radiated to space.

SPARCS being a FUV mission, it is highly susceptible to molecular contamination. The FUV can see as much as 45% throughput degradation with just a 2 nm thick layer of molecular contaminants (Figure 2). The SPARCS mission has a strict

Figure 2.

Degradation of FUV Band with Molecular Contamination

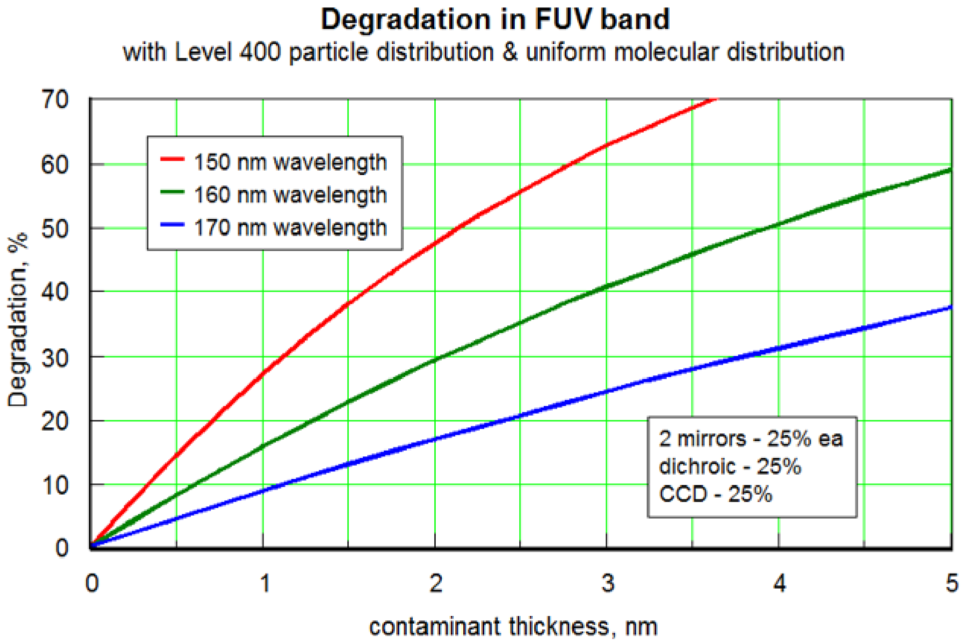

Note. This plot shows the degradation of the FUV band as the contamination thickness increases on the phase of each optic in the SPARCS payload. It can be seen that at 150 nm wavelength sees close to a 50% degradation with only a 2 nm thick layer of molecular contaminants on the surface.

Plot is by Jim Austin, contamination consultant for SPARCS

contamination control plan (CCP) that it follows throughout the assembly integration and testing (AI&T) phase of the mission to minimize the contaminants that may condense on critical surfaces. The CCP is a major driver in the work done for SPARCS detailed in this paper. Early in the SPARCS mission, it is determined that commercial thermal vacuum (TVAC) testing facilities are too "dirty" to meet the requirements laid out in the CCP and it would cost the mission too much to have a facility spend the time to clean a chamber in order to meet the cleanliness requirements. The SPARCS team and Arizona State University (ASU) partner in funding the development of a clean facility that is suitable for the AI&T of SPARCS as well as a CubeSat testing chamber that meets the contamination requirements in the SPARCS CCP. The chamber allows for on-site vacuum and thermal testing of the SPARCS payload and spacecraft in a clean environment where contamination can be monitored and mitigated.

Thermal Vacuum Testing

Thermal vacuum testing is an essential part of verifying the performance and survivability of a spacecraft and payload. Thermal testing is done at various levels of a spacecraft mission, from unit level to fully integrated spacecraft level. There are two types of thermal testing, and they can be done for various levels of hardware (unit, subsystem, instrument, spacecraft). Thermal cycle tests mean to stress the hardware to look for workmanship issues that could lead to infant mortality failures (*NASA-STD-7002B*, 2023). Thermal balance testing is used to verify the thermal control subsystem and correlate the thermal model. These test phases also simulate cold and hot conditions to verify all aspects of the thermal hardware and software (Gilmore, 2002).

Thermal testing at different levels can have different objectives. Unit level thermal testing is done primarily for environmental stress screening, performance verification, and demonstration of survival and turn on capability (Gilmore, 2002). Design issues should be found in qualification testing while acceptance testing should find any workmanship issues. Failures tend to decrease with cycle count with the failures tending to happen in the early cycles instead of the latter cycles. The rate of failures drops drastically after the first few cycles (Gilmore, 2002).

Subsystem level or payload level thermal testing would come after unit testing. It can be challenging to stress all the hardware as different units the assembly may have different temperature limits. The system will usually be constrained to the lower temperature limits as to not hurt the units with the lower temperature requirements. Looking at the system in this way may help identify what hardware needs to be tested at the unit level prior to the subsystem level. Testing at the subsystem level can be advantageous as problems are much easier to isolate and get to the root cause (Gilmore, 2002). A lot can be said about the confidence gained by doing subsystem level testing that the payload will perform at the system level.

System level testing has an emphasis on end-to-end performance and achieving the mission requirements. Here interfaces between subsystems are demonstrated and assured that the subsystems can work together. The primary goal of the system level thermal vacuum test is to prove workmanship and flightworthiness (Gilmore, 2002). The thermal system should be verified and calibrated, heater controls should be tuned as well as demonstrating performance. Thermal balance testing should consist of a hot and cold operational phase as well as non-operational phases. These tests should be based on the hot and cold cases seen from analysis. Extreme conditions should be used so that flight predictions do not exceed the tested simulated phases.

Contamination Control Methods

A main source of contamination for a space mission is due to outgassing when the system is put under vacuum. It is vital to choose materials that are in accordance with ASTME-595-77/84 [total mass loss (TML) <1.0% and collected volatile condensable mass (CVCM) <0.10%] (*Llis, 1999)*. The NASA outgassing database (Powers, 2023) is a great resource for identifying materials that are compatible with cleanliness requirements.

It is important to maintain the cleanliness of hardware throughout the entire AI&T process. Hardware should be precision cleaned upon acceptance in a clean area. Precision cleaning is done with ultra-sonic cleaning and solvent rinses/wiping in a clean environment (*Llis, 1999)*. Hardware should routinely be cleaned when handled to maintain cleanliness. Contact transfer of contamination is also a significant contributor to contamination so all surfaces and tools that come in contact with the flight hardware must be clean. To remove contaminants from critical surfaces that are sensitive to solvents the surface can be blown off with gaseous nitrogen and to remove molecular contaminants the surface may need to undergo thermal bakeout. When the surface undergoes thermal bakeout, heat is added into the system and the heat excites the molecules enhancing the rate at which molecules are removed from the surface (Figure 3).

Figure 3.

Removing Contamination with Heat

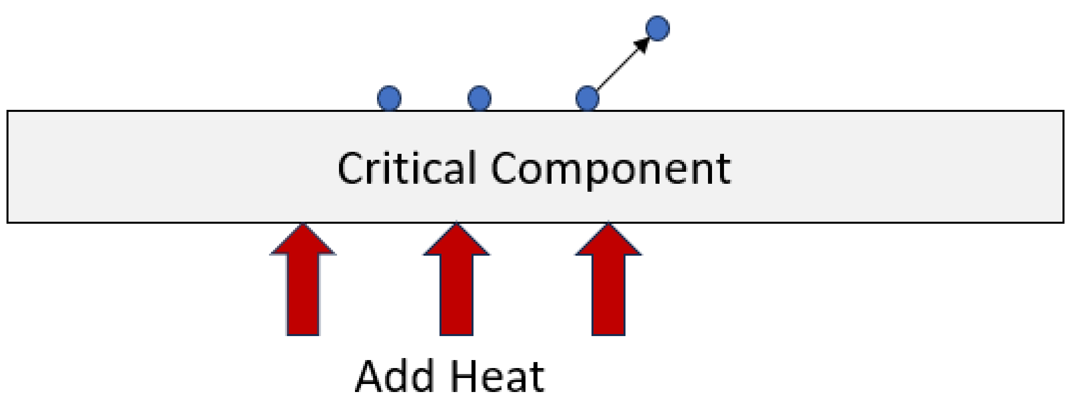

Note. The figure is a symbolic view of thermally baking out a critical component to remove molecular contaminants. Heat is added to the surface, contaminant is excited and leaves the surface.

To monitor contamination, a black light can be used to determine the presence of particulate contamination. If contaminants are present, a tape lift can be used to collect the contaminants and then used to determine the number and size distribution per area of the contamination. Molecular contamination levels are verified using a solvent wash, the solvent wash is used to collect a sample of the contamination where it is then analyzed using spectrometry to determine the contamination make up (*Llis, 1999)*.

When under vacuum, contamination is monitored using advanced equipment such as a residual gas analyzer (RGA) and a thermoelectric quartz crystal microbalance (TQCM). The RGA is a quadrupole mass spectrometer and is used to measure residual gases allowing for monitoring and interpretation of gas compositions in the chamber at low pressures. The TQCM has a matched pair of crystals and is used to measure mass loading. One crystal is the reference crystal while the other is the measurement. The output of the TQCM is a frequency, the crystals are both oscillating and as contaminants condense on the measurement crystal the frequency will change. The difference in frequency between the reference and measurement crystal can be converted to a mass. To determine the mass condensed onto a 15 MHz crystal, equation 1 from the CrystalTEC

$$m = 1.96 * 10^{-9}\ g/cm^2 Hz \tag{1}$$

TQCM Product Guide converts change in frequency to mass. Additionally, as frequency can fluctuate with temperature variations, a TEC is used to regulate the crystal's temperature within the range of -59°C to 80°C.

The RGA and TQCM are vital to monitoring contamination throughout all vacuum testing operations. During TVAC testing the payload will be cycled from hot to cold, it is critical to monitor contamination with the RGA and TQCM prior to cooling the payload. During cold operations condensable are monitored on the TQCM ensuring contaminants stay within the allowed contamination specifications.

Solar Transition Region UltraViolet Explorer (STRUVE)

STRUVE is a proposed CubeSat mission equipped with a slit-scanning, full Stokes spectropolarimeter designed to observe the Sun within a spectral range of 259 to 281nm. With an impressive resolving power of 41,500 and boasting high signal-to-noise (SNR) capabilities, STRUVE aims to address two primary scientific objectives: Firstly, to gain insights into the magneto-fluid conditions at the base of the corona and the dynamics of magnetic energy buildup and release (Gamaunt et al., 2022). Secondly, to investigate the variations in magnetic and plasma properties between open and closed magnetic structures at the base of the solar corona. The observed wavelength region includes crucial lines such as Mg II h and k, along with numerous Fe I and II lines. These collectively enable the determination of magnetized plasma parameters across the solar atmosphere, spanning from the photosphere through the chromosphere and into the transition region at the corona's base.

The work conducted on STRUVE is supported NASA under Grant 80NSSC21K1792 issued through the Heliophysics Flight Opportunities Studies (H-FOS) program as part of a concept study. This study aims to assess the feasibility of the STRUVE instrument in achieving its scientific objectives using the 12U CubeSat platform. One of the main challenges facing STRUVE is minimizing the movement of the image on the slit and detector while it is pointed at its target. The yaw and pitch pointing stability requirement for STRUVE is ≤ 0.417”, as specified in (Berner et al., 2022). To meet this requirement, a high-performance attitude determination and control system (ADCS) system is utilized in conjunction with a tip/tilt mirror system mounted on the secondary mirror of the telescope. Additionally, careful consideration of the thermal environment surrounding STRUVE is crucial to mitigate thermal-induced optomechanical distortion, which can lead to misalignments.

The movement of the image at the slit or detector directly impacts the polarimetric accuracy of measurements and must be limited to a small fraction of the spatial resolution during a modulation cycle (~0.8 seconds). During observations, light enters STRUVE through a slit and then passes through a polarimetric modulator. Temporal modulation is achieved using a spinning retarder, effectively encoding the polarization signal in a series of sequential measurements.

Orbital Thermal Environment

The thermal environment of STRUVE can be analyzed at both the spacecraft and instrument levels. At the spacecraft level, the focus is on the orbital thermal environment, identifying external factors that induce heat loads or act as heat sinks. This includes variations in solar radiation, planet loads, and reflective loads. The orbital thermal environment is highly dynamic and subject to constant change, influenced by factors such as orbital altitude, inclination, and orientation.

Conversely, the instrument level focuses more on the thermal conditions generated by the spacecraft itself. This involves internal thermal management systems, heat dissipation mechanisms, and insulation aimed at maintaining optimal operating temperatures for instrument components. A comprehensive understanding and management of the thermal environment at both levels are imperative for ensuring the reliability and performance of STRUVE throughout its mission duration.

Understanding the primary sources of environmental heating in Earth's orbit is crucial for comprehending the orbital thermal environment. These sources primarily include direct sunlight, albedo (reflected light from Earth), and planet shine (infrared light emitted from Earth) as depicted in Figure 4. The spacecraft's temperature results from a balance between absorbed and emitted energy. Particularly in a low Earth orbit (LEO), where the spacecraft has a limited view of the globe, variations in Earth's environment can significantly impact spacecraft temperature, especially with a short time constant.

Direct sunlight serves as the predominant environmental heat source that the spacecraft must contend with. Solar intensity at 1 AU measures 1367 W/m^2, but due to Earth's elliptical orbit around the sun, this intensity fluctuates between 1414 W/m^2 at the closest point and 1322 W/m^2 at the furthest (Gilmore, 2002). Factoring these fluctuations into worst-case thermal analyses is crucial.

Albedo refers to sunlight reflected off the planet or moon, typically presented as a fraction of light reflected back. Calculating albedo accurately is challenging due to variables in the Earth’s surface and the difference in how light reflects off of it (continental or oceanic regions, snow or ice coverage) while also being dependent on the spacecraft's position relative to the subsolar point. As the spacecraft moves away from this point, albedo decreases and approaches near zero at the terminator (Gilmore, 2002).

Planet shine represents the heat load from Earth itself, and is light emitted within the same wavelength range as that emitted by the spacecraft and cannot be reflected like direct sunlight. In the wavelengths related to radiating at room temperature (~10 um), the spacecraft radiators would ideally act as a black body making it a good emitter and absorber of energy at those wavelengths. Radiators with a view of Earth experience

Figure 4.

Simplified View of Orbital Loads and Heat Sink for a Spacecraft

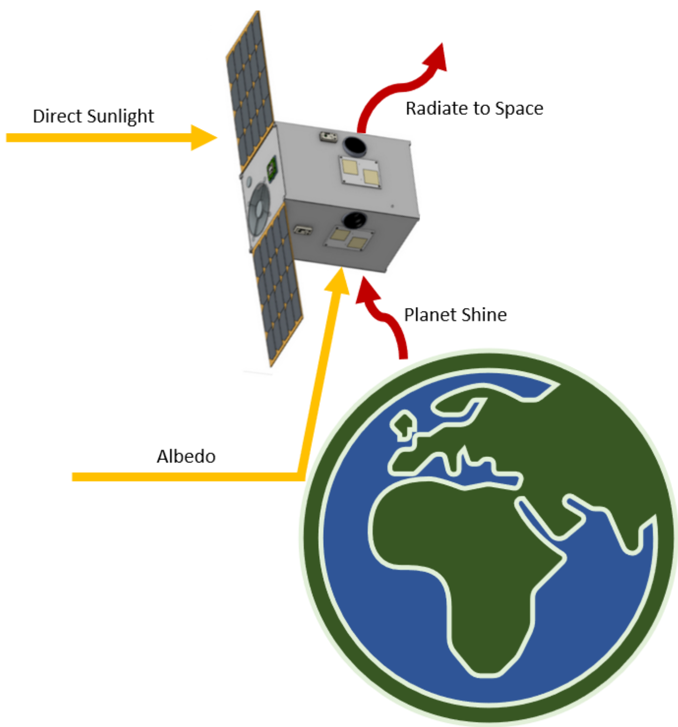

Note. The principal elements of the thermal environment are depicted in the figure showing direct sunlight, albedo, planet shine, and the heat loss to space (Gilmore, 2002).

significant backloading due to this effect. Simplifying analysis involves initially disregarding Earth when calculating view factors to space and then adding planet shine energy as an "incoming" heating rate (Gilmore, 2002). The “Spacecraft Thermal Control Handbook” (Gilmore, 2002) is an excellent reference that has recommended values to use for planet shine and albedo.

When talking about orbits there are many important parameters that are used to describe an orbit. A common parameter used, especially when talking about low Earth orbits, by thermal analysts is the orbit beta angle. The beta angle is useful when trying to visualize the orbit thermal environment (Figure 5). The orbit beta angle is the angle between the orbit plane and the solar vector and can vary from -90 to +90 deg (Gilmore, 2002).

Figure 5.

Beta Angle Definition

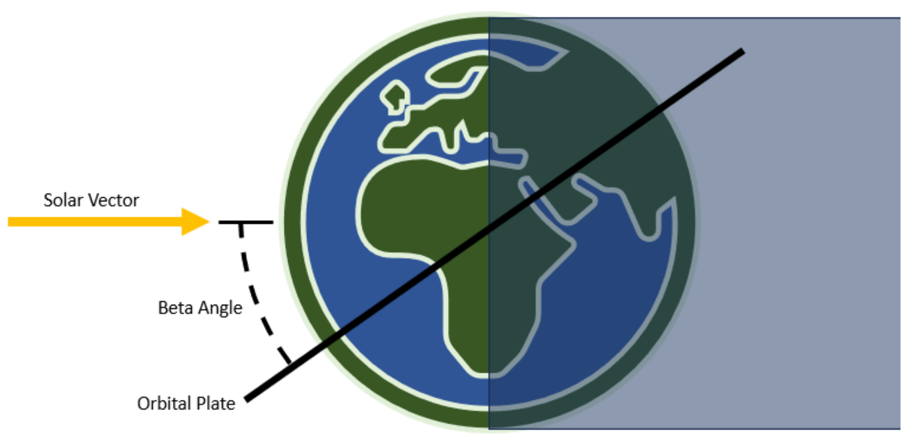

Note. The beta angle is the angle between the solar vector and the orbital plane. The beta angle is 0° when the orbital plane is in line with the solar vector and ±90° when perpendicular to the solar vector.

This figure was adapted from the “Spacecraft Thermal Control Handbook.”

Types of Thermal Control

In spacecraft thermal control, two primary methodologies are utilized: passive thermal control and active thermal control. Typically, the design process begins with a passive system and incorporates active solutions as necessary. This sequential approach is preferred due to the numerous advantages offered by passive thermal systems, including simpler designs, lower costs, reduced volume, and lower risk.

Passive thermal control technologies encompass a range of methods, including multilayer insulation (MLI), surface coatings/films, louvers, sun shields, thermal switches, thermal straps, and phase change materials. During the design phase, careful consideration is given to material selection, spacecraft orientation, thermal interfaces, and thermal path designs to optimize passive thermal control effectiveness.

Active thermal control systems become necessary when precise temperature regulation is required. These systems, which require input power for operation, include resistance heaters, cryocoolers, thermoelectric coolers, and fluid loops. While active systems offer the advantage of precise temperature control, they also entail increased costs and design complexity compared to passive systems. However, their incorporation is indispensable for achieving the tight temperature tolerances often demanded in some spacecraft or instrument operations.

The Exoplanet Climate Infrared Telescope (EXCITE)

EXCITE, a NASA-funded high-altitude balloon mission, aims to measure spectroscopic phase curves of hot Jupiter-type exoplanets in the near-infrared range (0.8-4 um) (Nagler et al., 2019). By collecting phase curve measurements of transiting exoplanets, the spectrograph onboard EXCITES provides valuable insights into the compositions and energy distribution of exoplanet atmospheres.

The mission employs a Ritchey-Chrétien telescope with a 0.5 m diameter primary mirror to capture light from the target exoplanets (Nagler et al., 2019). A cold spectrograph operating at 120K, positioned behind the telescope, receives the collected light. The light enters the spectrograph through a 100-micron slit and is then directed to an off-axis parabola for collimation. Following collimation, the light is dispersed using a CaF_2 prism and focused again with another off-axis parabola (Bernard et al., 2022). The beam is split into long and short wavelength channels, and both channels are imaged at two distinct areas on the same detector. This setup allows for comprehensive spectroscopic analysis of the exoplanet data gathered during the mission.

Mounting Optics

The primary objective of optics mounts is to ensure the precise positioning and alignment of optical components. Ideally when constraining optics, one would aim to use the kinematic principles to effectively constrain all six degrees of freedom (three translational and three rotational) without introducing redundancy and over constraining the system (Yoder, 2008). When a system is over constrained it can lead to less than ideal effects such as increased stress and warping. When developing opto-mechanical mounts, several critical factors must be considered. Stability is paramount; mounts should effectively prevent undesired movement or vibration-induced perturbations that could compromise optical performance. Additionally, thermal stability is essential as thermal expansion or contraction can adversely affect optic alignment and performance.

Therefore, opto-mechanical systems must maintain stability across the entire operational temperature range. These considerations are crucial for ensuring the optimal performance and reliability of optical systems in various applications and environmental conditions.

In the design of optical interfaces, flexure can be utilized to provide controlled motion or flexibility in specific directions. By incorporating flexures into a system's design, components can be protected from damage caused by shock or vibration. Flexures are often employed to compensate for thermal effects. At interfaces with different coefficients of thermal expansion (CTE), flexures can offer compliance and stress relief. This proves particularly useful in avoiding the imposition of excessive stress on an optic, which could affect its performance.

CHAPTER 2

TEST BED DEVELOPMENT AND SOLUTIONS: DESIGNING A THERMAL VACUUM CHAMBER AND SUPPORT HARDWARE FOR SPARCS

Motivation for the Development of the SPARCS Testing Chamber

SPARCS is a 6U CubeSat mission focused on astrophysics with a concurrent technology demonstration component (Ardila et al., 2018). The CubeSat's primary objective is to monitor M-dwarf stars in two distinct UV photometric bands: the NUV band (260-300nm) and the FUV band (153-171nm). A notable feature of SPARCS is its distinction as the first CubeSat mission to measure flares of M-dwarf stars. Moreover, SPARCS is contributing to the advancement of UV detector technology by deploying in space for the first-time high quantum efficiency (QE), UV-optimized detectors developed at JPL (Nikzad et al., 2012). These delta-doped detectors have a history of successful use in various applications, including industrial settings, ground-based telescopes, and sounding rockets. Notably, they demonstrate over 5 times the sensitivity of the detectors utilized in GALEX, the most recent dedicated UV mission (Jewell et al., 2018). SPARCS is expected to lay the groundwork for the application of these detectors in future missions, such as the Habitable Worlds Observatory

Table 1

SPARCS Requirements to be Verified in Chamber

Requirement ID	Requirement	Rational
PL 3.9, Payload Annealing	The payload shall have the ability to heat the payload to 60°C	The annealing procedure involves heating the detectors to +57°C for a period of 48 hours
PL 3.11, Blur Spot Size	The payload shall provide a blur spot with an RMS radius <0.1Â±0.03 pix over 10 minutes at the field center	Flow down of F2.4 Jitter + PSF + Aberrations come from the photometric model and exposure time calculator (ETC)
PL 3.12, NUV Sensitivity	In a 10-minute exposure, the payload NUV imager system shall be capable of measuring with a S/N = 21 a flux of 0.7mJy	Based on V9 of ETC, minus airglow, jitter, background, and red leak, it allows for observation of the target list
PL 3.13, FUV Sensitivity	In 10 minutes, the payload FUV imager system shall be capable of measuring with S/N = 19 a flux of 0.8mJy	Based on V9 of ETC, minus airglow, jitter, background, and red leak, it allows for observation of the target list
PL 3.14, Field of View Size	The payload shall have a 20-arcminute diameter of corrected FOV	Relative calibration ancillary science
PL 3.16, FUV Channel Photometric Stability (FOV)	The payload shall maintain the same FUV sensitivity within 10% over a 40' diameter FOV	Allows for observation of target list
PL 3.18, NUV Channel Photometric Stability (FOV)	The payload shall maintain the same NUV sensitivity within 10% over a 40' diameter FOV	Allows for observation of target list
PL 3.19, Total Throughput Measurement	The payload total system throughput shall be known to 5% per wavelength point, for all wavelengths for 120 nm to 1000 nm	Throughput is defined as Area x Optical system reflectivity x dichroic transmissivity (& reflectivity) x filter throughput x detector QE. This requirement assumes a 10% red leak and results in 3% precision in the total number of counts
PL 3.20, Total Throughput Measurement Precision	The payload total system throughput shall be measured every 5 nm overall and 1 nm within ± 2 FWHM of the band center to requirement PL 3.19	The dichroic is expected to show high-frequency excursions that need to be fully characterized on the ground. Other elements of the system are expected to show less spectral variation and, therefore, be a subdominant contribution to the dichroic. However, here we set the requirement on the total system
PL 3.45, Bandpass FUV Center	The payload FUV channel mean wavelength shall be 162 nm	Should encompass C IV and HE II
PL 3.46, Bandpass FUV Width	The payload FUV channel spectral response shall be between 18 nm to 60 nm FWHM, with the goal of maximizing S/N	Transition Region emits in the far UV (FUV)
PL 3.47, Bandpass NUV Center	The payload NUV channel mean wavelength shall be 280nm	The strongest NUV emission lines are Mg II lines at 280 nm
PL 3.48, Bandpass NUV Width	The payload NUV channel spectral response shall be between 40 nm to 60 nm FWHM, with the goal of maximizing the S/N	The chromosphere emits in the near UV (NUV)
PL 3.57, Detector Cooling	The payload shall cool its detector by conducting heat to the spacecraft interface as specified in the SPARCS Spacecraft to Payload ICD	Need to dissipate detector heat from each of the two detectors to cool to operating temperature
OB 4.7, NUV Camera Placement	The optical bench shall position the NUV focal plane 40 mm from the backplane of the telescope as measured down the optical axis of the system to within 0.14 mm	Need to keep the NUV camera in focus to meet the requirements set by the photometric model
OB 4.8, FUV Camera Placement	The optical bench shall position the FUV focal plane 40 mm from the backplane of the telescope as measured down the optical axis of the system to within 0.14 mm	Need to keep the FUV camera in focus to meet the requirements set by the photometric model

Note. This table lists the requirements that will be verified by the SPARCS test chamber. These requirements are the driving requirements for the development of the chamber. The table lists the requirement ID, the requirement, and the rationale.

Assembly Integration and Testing (AI&T) phases of SPARCS are taking place at Arizona State University. To tackle the inherent challenges related to molecular contamination in the FUV region and mitigate contamination risks throughout the AI&T process for SPARCS, the creation of a dedicated test chamber was essential. The formulation of the SPARCS test tank followed a rigorous systems engineering approach, wherein the design requirements were derived from the fundamental functionalities essential for the contamination control and testing of SPARCS.

These design requirements adhere to a systematic framework, emphasizing the verification of SPARCS' specific functionality while ensuring adaptability for subsequent CubeSat payload and spacecraft testing. The delineated requirements, as outlined in Table 1, Are the payload requirements to be verified through testing in the test chamber.

Half of the chamber's funding is provided by the SPARCS mission, with the remaining half being funded by ASU. The university's condition for funding half of the chamber is that its design must be adaptable for future CubeSat missions. The expanded budget from the university has allowed us to enhance the test tank's capabilities to include TVAC testing. This upgrade is particularly advantageous for the SPARCS mission due to a significant risk associated with potential contamination in offsite facilities during TVAC testing. With the new TVAC capabilities, we can monitor and maintain the cleanliness of the chamber, reducing the mission's overall risk.

This chamber plays a pivotal role in conducting TVAC tests for both the instrument and the spacecraft: a crucial step in showcasing their capabilities and verifying workmanship under realistic flight conditions applying the philosophy “test as you fly.”

Additionally, the chamber facilitates thermal balance testing for the SPARCS payload: an essential process for validating the thermal control subsystem and correlating the thermal model. Notably, correlating the thermal model with test data has proven effective in reducing the standard deviation of flight temperature data from 9°C to 5.6°C (Welch, 2006).

Beyond TVAC testing and thermal balance assessments, the chamber assumes a vital role in the contamination control plan. Serving as the final bake and confirmation site for cleanliness, the chamber ensures the integrity of the payload hardware before integration.

Chamber Overview

The development of the chamber employes a systems engineering approach, catering to the needs of two primary stakeholders: the SPARCS project and ASU. The design requirements are crafted based on the chamber's functions, aiming to facilitate the verification of SPARCS payload performance requirements and to maintain flexibility for future CubeSat payload/spacecraft testing. The chamber is designed to:

1. Provide a thermal environment similar to what the payload would experience in LEO for verifying payload requirements PL 3.9 and PL 3.57.
2. Ensure a clean vacuum environment in adherence to the SPARCS contamination control plan.
3. Furnish a high vacuum environment ($\leq 10^{-5}$ torr), replicating the conditions the payload would encounter in LEO.

The final chamber design (Figure 6) is a customized 2 feet (height) x 2 feet (width) x 2 feet (depth) from Kurt J. Lesker Company. The overall size is driven by the fact that the chamber and its cart need to fit through a standard door frame while also providing enough space for testing of a CubeSat payload. This chamber incorporates a plumbed platen and shroud for effective cooling. The platen, measuring 22” x 22”, features a 1” x 1” ¼-20 hole pattern, facilitating the secure attachment of test hardware. The chamber is equipped with a total of 9 feedthroughs, serving various purposes:

- Two 4.5” ConFlat (CF) feedthroughs are designated for the plumbed platen and shroud.
- Two 8” feedthroughs, one for the residual RGA and the other with a 50-pin D-sub connector.
- Two 2.5” CF feedthroughs are allocated for a burst disk and the light source (monochromator).
- One 6” CF feedthrough is designated for the turbo pump.
- One 2.75” viton seal feedthrough is provided for the vent valve.
- One 6.25” CF feedthrough accommodates two 50-pin D-sub connectors.

Notably, the chamber boasts a temperature range from -175°C to 100°C, enabling effective chamber bake-out and the creation of a cold-space-like environment. These features enhance the versatility and functionality of the chamber design.

Figure 6

Chamber Overview

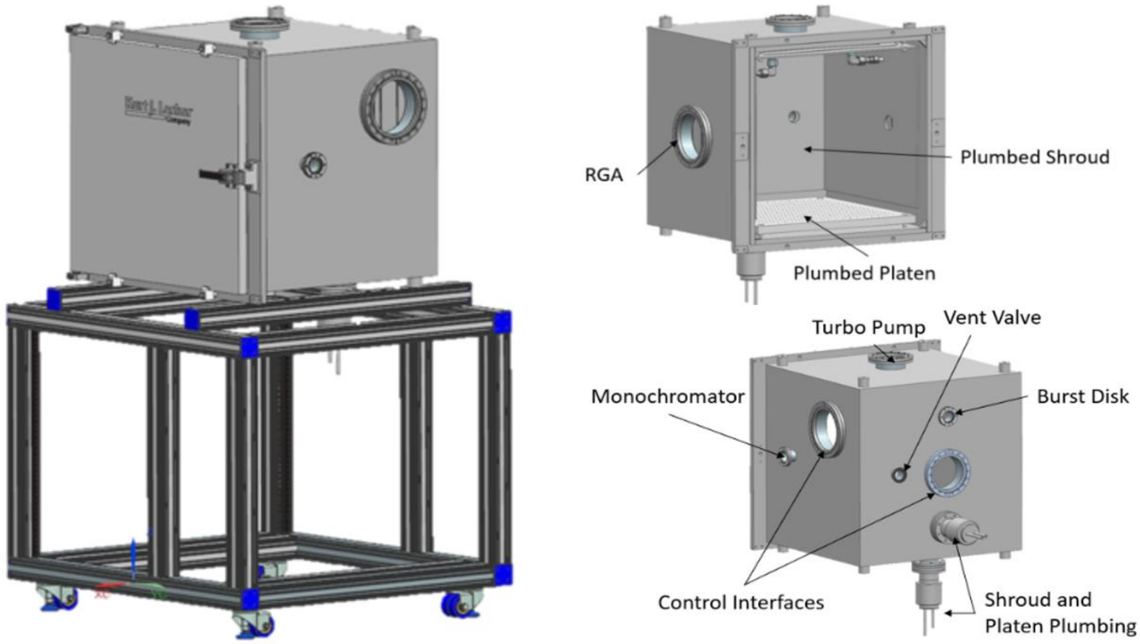

Note. This figure shows images of the CAD model of the chamber detailing the locations of the feedthroughs and their purposes.

Chamber Heating and Cooling System Trade Study

A trade study was done to determine the thermal control solution for the chamber to be utilized. Three distinct systems or methods are evaluated: the Hermetic Refrigerating and Heating Circulator (HRHC) dynamic temperature control system, a liquid nitrogen (LN2) system with resistance heaters, and a combination of both. Each system presents its unique advantages and drawbacks. The primary goal of this trade study is to identify the key criteria most relevant to the project and assess the choices based on these criteria.

The decision-making criteria encompass:

1. **Price:** Evaluating the cost implications and financial considerations associated with each system.
2. **Payload Testing Temperature Range:** Assessing each system's ability to meet the required temperature range for payload testing.
3. **Ease of Use/Setup:** Measuring the user-friendliness and ease of system setup and operation.
4. **Temperature Control:** Examining the precision and reliability of each system in maintaining the desired temperature.
5. **Leak Risk:** Evaluating the likelihood of introducing contaminants into the chamber that would be detrimental to the mission.

Table 2

Thermal Control Trade Study

Decision Matrix for Chamber Thermal Control			LN2 and Heaters (1)	HRHC-625 Chiller Unit (2)	HRHC-625 Chiller and LN2 (3)
Criteria	Mandatory (Y=1/N= 0)	Weight	Scores	Scores	Scores
Price	1	0.3	4	3	1
Temperature Testing Range	1	0.25	5	3	4
Ease of Use/Setup	0	0.1	3	1	1
Temperature Control	1	0.2	5	4	5
Leak Risk	0	0.15	5	1	1
Total		1	0.9	0.54	0.51

Note. The table presents the decision matrix used to determine the chamber's cooling system. The criteria outline the factors deemed significant for the decision-making process, while the scores indicate the performance of each solution based on these criteria. Ultimately, the LN2 and heaters option emerged as the preferred choice for the chamber. High scores are based on a 1 to 5 scale, with 1 being the least supportive and 5 being the most supportive of the criteria. For example, a 5 in price would mean the option best fits in the budget.

Each of these criteria has been assigned a specific weight and given a score. The breakdown of these criteria, their respective weights, and scores is detailed in Table 2. This comprehensive analysis will guide the selection of the most suitable thermal control method, aligning with the project's unique needs and priorities.

Based on the trade study's outcomes, the LN2 and resistance heaters solution emerged as the most favorable choice. In terms of the overall price point, this solution came out to be the most cost-effective, especially after talking to facility management about incorporating either solution. To accommodate the HRHC-625 chiller unit, the SPARCS project would additionally need to pay for the facility to install the required power line and outlet.

Regarding the temperature testing range, the LN2 and Heaters demonstrate a significant advantage by offering a much broader testing range. The LN2 system can cool the platen and shrouds to approximately -175°C and heat them to +100°C, with the chamber's painted surfaces being the limiting factor. In contrast, the HRHC-625 Chiller unit had a specified range of -60°C to 100°C.

A pivotal factor in favor of the LN2 and heater solution was the ease of use and setup criteria. Investigation revealed that implementing the chiller unit in the lab would necessitate the installation of a new power line and outlet to accommodate the unit's power requirements. The prospect of additional costs associated with power line installation, coupled with the convenience factor, weighed heavily in the decision-making process.

The final determinant was the leak risk. In the event of a leak occurring during vacuum conditions, the LN2 system presented an advantage as it would release dry nitrogen into the chamber, minimizing the risk of contamination. In contrast, the chiller unit would potentially leak the cooling/heating medium, often a silicone thermal fluid, into the chamber, posing a higher contamination risk.

In sum, the comprehensive evaluation of these factors led to the preference for the LN2 and resistance heaters solution, aligning with the project's specific requirements and priorities.

Chamber Heating System

The chamber's heating system utilizes closed-loop thermal control and is comprised of five temperature-controlled zones and one passive zone, with each temperature-controlled zone consisting of a temperature sensor and heaters. These

Figure 7

Chamber Heater Layout

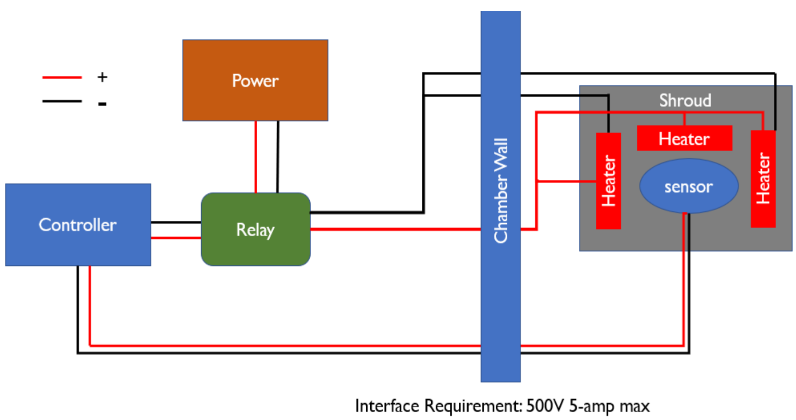

Note. In the overall layout, each zone comprises three heaters, a sensor, control, a relay, and a power supply. Additionally, the diagram illustrates the chamber interface requirements, with each pin having a limit of 500V and 5 amps.

thermal zones encompass the platen and the shroud, with each face of the shroud representing a single thermal zone. The chamber's door serves as the passive zone. Figure 7 provides a visual representation of each thermal control zone. Type T thermocouples are employed as the temperature sensors in the chamber design due to their stability, reliability, and accuracy within the -200°C to 200°C temperature range.

Control over the heaters is facilitated by Omega's Universal 6 channel controller (CN616A), utilizing solid-state relays for their enhanced reliability during cycling. To maintain cost-effectiveness, the heating system was designed using off-the-shelf components, guided by specific design requirements listed in Table 3. Voltage and amperage interface requirements are limited to the maximum allowable values for the chamber interface pins. To meet operational needs, ramp rate requirements ensure a

Table 3

Chamber Thermal Requirements

Requirement ID	Requirement	Rational
TTH-6.1	The voltage interface at the chamber shall be less than 500 volts	Maximum voltage a connector pin on the chamber can handle
TTH-6.2	The current at the chamber interface shall be less than 5 amps	Maximum current a connector pin on the chamber can handle
TTH-6.3	The heating system shall be capable of heating the platen with a minimum ramp rate of 0.5 °C/min	Ensure the platen can heat up at a reasonable rate without damaging flight hardware
TTH-6.4	The heating system shall be capable of heating the shrouds with a minimum ramp rate of 0.5 °C/min	Ensure the shroud can be heated at a reasonable rate
TTH-6.5	The heating system shall be capable of maintaining the temperature of the shroud to the stability of ± 2 °C of the set temperature for extended durations (minimum 1 day)	Produce a stable thermal environment for thermal balance testing of flight hardware
TTH-6.6	The heating system shall be capable of maintaining the temperature of the platen to the stability of ± 2 °C of the set temperature for extended durations (minimum 1 day)	Produce a stable thermal environment for thermal balance testing of flight hardware

gradual heating process. Thermal balance tests dictate the temperature stability requirement, which influences temperature soaks in steady-state instrument conditions.

To appropriately size the heaters, it is essential to consider the factors influencing the required heater power. In this scenario, there are two key drivers: first, the heater power needed to maintain the temperature at a constant 80°C, and second, the heater power necessary to achieve a temperature ramp rate of 0.5°C/min for both the platen and shrouds.

Assuming efficient insulation for the shrouds and platen, the predominant driver for the heater power is the requirement to meet the specified ramp rate. To calculate the power (Q) essential for achieving this ramp rate, we can derive the power needed using equation 2 (Cengel & Ghajar, 2020).

$$m * Cp * \frac{dT}{dt} = Q \tag{2}$$

Given that the platen has a mass (m) of 19.7 kg, is primarily composed of 6061 aluminum with a specific heat of 896 J/kg/K (Gilmore, 2002), and the required ramp rate (dT/dt) is 0.5 °C/min; the total heater power needed for the platen is 147.1 W. Adding a 15% margin to the 147.1 W will ensure the heaters are appropriately sized to meet the thermal control requirements of the system.

Figure 8

Chamber Heating Circuit Diagram

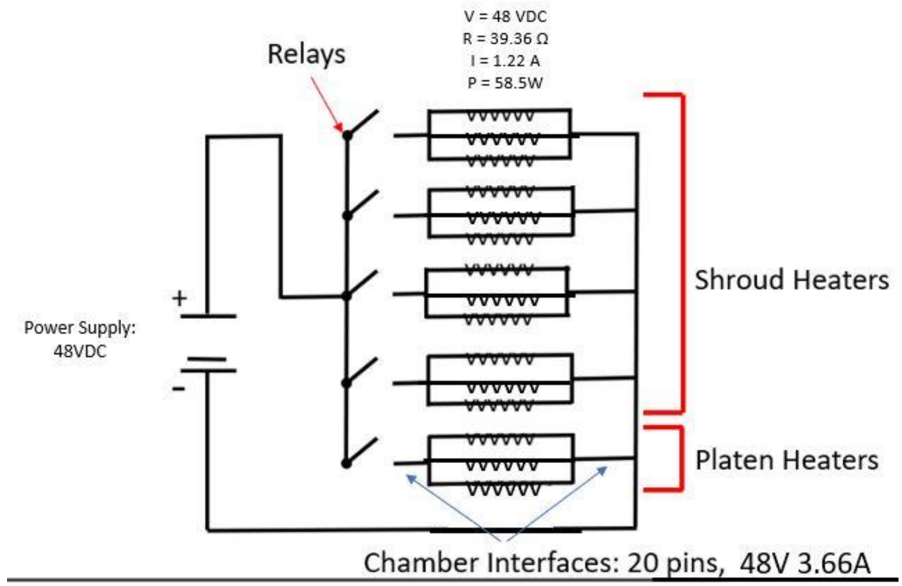

Note. This figure shoes the heater circuit. The circuit is powered with a 48V power supply. All heaters are wired in parallel. To limit the number of pins needed to interface with the chamber, wires have a junction on the inside of the chamber where they split up into three parallel heaters. Due to the heaters being in parallel if a heater were to fail the others would still be able to provide power.

The shroud is broken up into four thermal control zones due to each face being a relatively larger thin plate, and to reduce gradients, each face is controlled on its own with 3 heaters across the face. Each face of the shroud is ~4.4kg and made of 6061 aluminum. Using equation 1 and the required minimum ramp rate, the minimum power per face comes out to be 32.7 W.

Minco All-Polyimide Themofoil heaters are the optimal choice for the heating element due to their advantageous features, such as low outgassing properties and a wide temperature range. From the available off the shelf options, the HAP6949 heaters stood out for several reasons, including their 3x5 inch dimensions, 39.36-ohm resistance, and capacity to handle up to 115 V.

To ensure efficient heat dispersion, three of these heaters are strategically distributed within each heating zone. With a 48V power supply, each heater generating approximately 58.5 W, resulting in a watt density of 4.36 W/in^2. The wiring configuration, as depicted in Figure 8, provided a consistent 48V and 3.66 amps at the chamber interface.

Each heating zone produces a power output of 175.5W, exceeding the minimum required heating of 147.1W for the platen and allowing for a significant 19.3% heating power margin. This configuration guarantees robust and dependable thermal control within the chamber. Notably, the 175.5W on each face of the shroud significantly surpasses the minimum requirement of 32.7W. The decision to choose these heaters was primarily influenced by their larger footprint, outweighing the consideration of lower wattage offered by other off-the-shelf heater options. This choice ultimately aligns with the specific heating requirements of the project, ensuring effective and reliable performance.

A thermal model of the chamber is constructed using Thermal Desktop (*Thermal Desktop | C&R Technologies*, n.d.), aiding in determining the ideal placement of heaters and sensors within each thermal zone, as depicted in Figure 9. The chamber shrouds and platen were modeled to match the actual components' thermal radiative properties, thermophysical properties, and size. The heaters in the thermal model were patterned after the previously selected and designed heating system to simulate their performance with various orientations. The chosen orientation, as seen in Figure 9, results in minimal

Figure 9

Chamber Thermal Model Snapshot

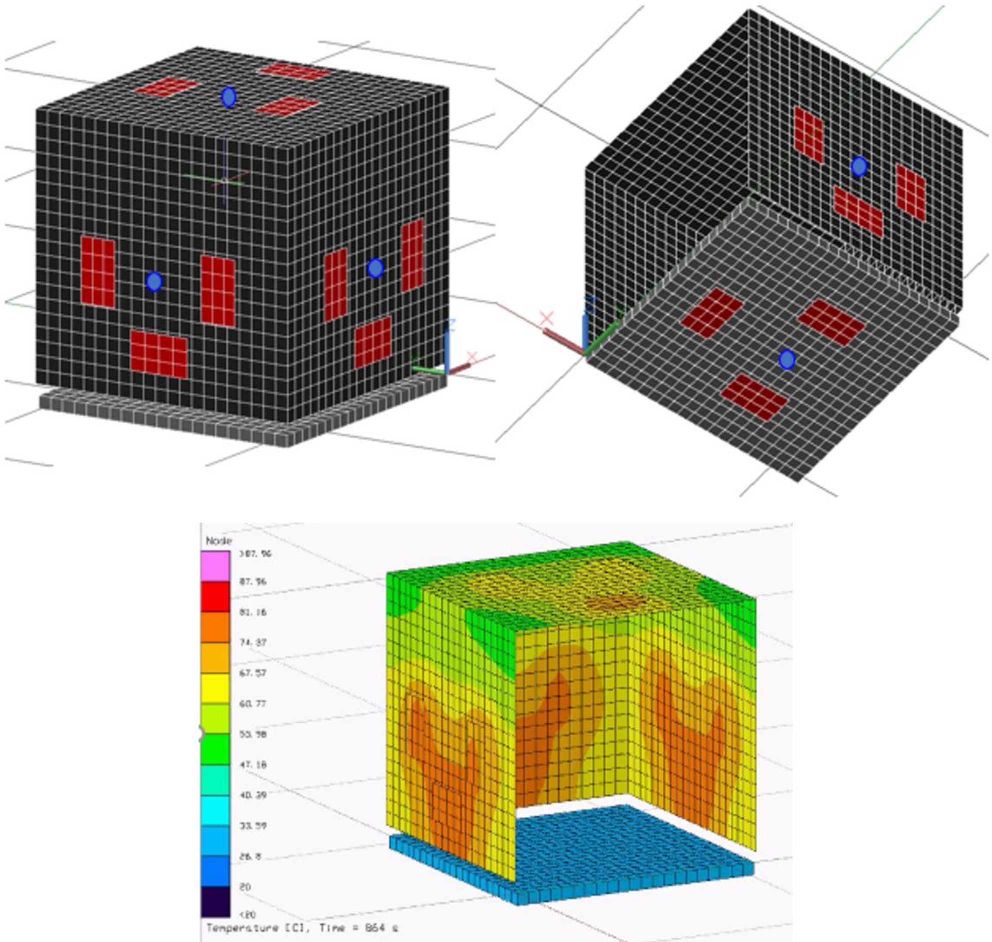

Note. The above figure is a look at the thermal model in Thermal Desktop. In the top views, the red rectangles are the heater locations on the shroud and platen while the blue dots are the temperature sensor locations. The image at the bottom shows a snapshot from the model transient results, and the heaters can be seen warming the shroud and platen. The platen lags behind the shroud due to its larger thermal mass and less total heating power.

temperature gradients across the shrouds and platen. Figure 10 illustrates the heater performance at an 80°C set point with on (79°C) and off (81°C) control.

Figure 10

Chamber Thermal Model Results, Temperature vs. Time

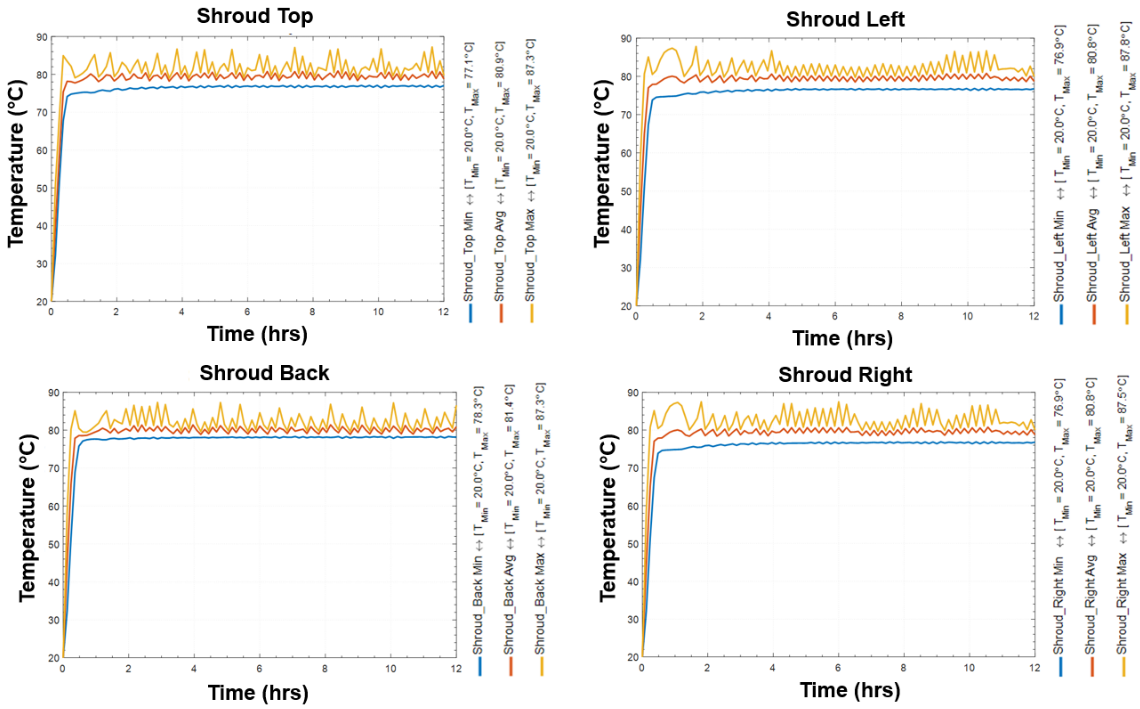

Note. The above plots show the predicted performance of the heating system over a 12-hour period from the Thermal Desktop model. Shroud Left, Right, Back Top are all referenced from looking into the chamber standing in front of the door.

The integration and testing of the heating system takes place throughout the fall of 2020. The process begins with the removal of the thermal shroud and platen from the chamber. All surfaces where the heaters and thermocouples would be placed are surface prepped by cleaning the surface with isopropyl alcohol (IPA), abrading the area where the heaters are be applied, and then cleaning the surface again where a water break test is done. Heaters and thermocouples are affixed using EP21TCHT-1 adhesive, chosen for its thermal conductivity, electrical insulation, cryogenic suitability, high-temperature resistance, low outgassing, and ambient temperature curing. After application, 3m 425

Figure 11

Heater Installation on Chamber

Note. The above images show different stages of integrating the heating system into the chamber. Image of shroud after uninstalling it from the chamber (Top Left). Image of the shroud with prepped heater and thermocouple locations (Top Middle). Image of the shroud with heaters and thermocouples epoxied to shroud (Top Right). Image of the shroud with heaters taped over with 3M 425 Aluminum foil tape (Bottom Left). Platen with heaters taped over (Bottom Middle Left). The chamber with platen and shroud was reinstalled (Bottom Middle Right).

aluminum foil tape was placed over the heaters to promote heat spread and reduce radiative heat transfer from the heaters themselves. Before reinstalling the shroud and platen into the chamber, a complete bench test of the heating circuit is conducted, ensuring all wiring was without defects and the system functions as expected outside the chamber.

TVAC Cooling System

The chamber's cooling system uses LN2 to cool both the platen and the shroud. Two LN2 Dewars supply the system, and there are two inlets for seamless Dewar switching. To facilitate control, the system is equipped with two 230L Dewars and two cryogenic solenoid valves. The cooling system utilizes closed-loop control, with the same Omega CN616A controller used for the heating system governing the cooling system.

Figure 12

Chamber Cooling System Schematic

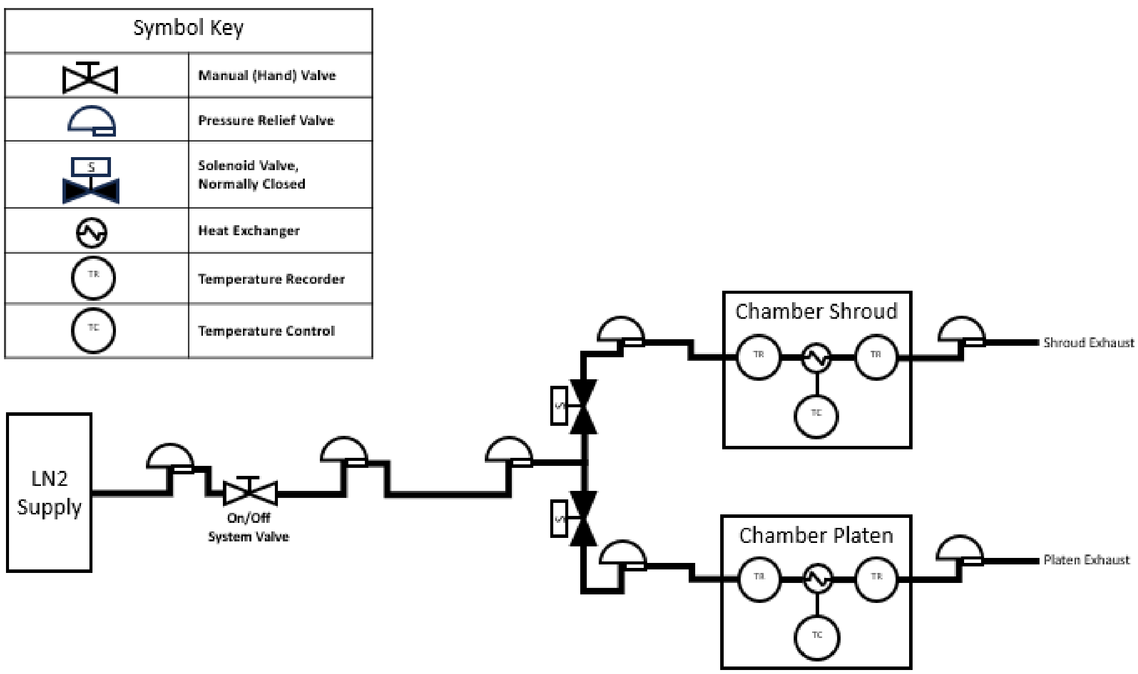

Note. The schematic above is an overview of how the cooling system on the chamber works. The system strategically has pressure relief valves in locations to ensure if LN2 gets trapped it does not over-pressurize the system and, as it warms up and becomes a gas. From left to right, the system has an LN2 supply, goes to an On/Off valve, then splits to two solenoid valves. The solenoid valves control the LN2 flow to the chamber shroud and platen. Excess LN2 or nitrogen leaves the system through the platen and shroud exhausts.

For the shroud, all faces are constrained to be on the same cooling circuit due to design limitations. To control the cooling effectively, the sensor closest to the shroud's inlet is used. This approach ensures a controlled and gradual cooling process, preventing over-pressurization. Conversely, using the sensor farthest from the inlet can lead to over-pressurization, causing leaks in the shroud plumbing to form and resulting in nitrogen leaking into the vacuum.

Users can change which sensor is used for solenoid control of the shroud as each panel cools to the set temperature along the circuit's path. However, this design limitation results in an extended duration for the shroud to cool down. Fortunately, for SPARCS payload testing, where the payload operates in a relatively "warm" in-flight environment, the shrouds do not need rapid or extensive cooling. This tailored approach addresses the specific constraints in the shroud design while meeting the requirements of the SPARCS mission.

TVAC Chamber Performance

To evaluate the thermal performance of the chamber, the performance of the temperature control is analyzed. Chamber temperature data from the qualification test of the SPARCS TEC was used for this analysis. In this test, the TEC mount is fastened to a fixture mounted to the chamber platen. The platen was used to drive the TEC to the predefined upper and lower temperature limits (Figure 13). This test requires the temperature of the platen to be cycled to thermal cycle the TEC to ensure its functionality and identify any potential workmanship issues prior to integration into the payload.

Figure 13

Chamber Temperatures vs. Time Plot from the TEC Test

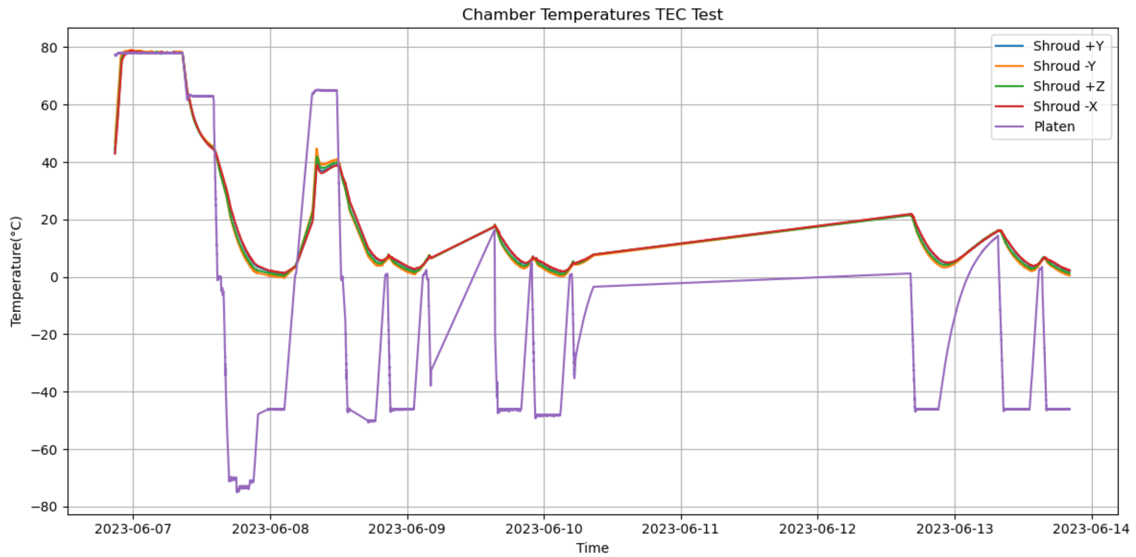

Note. This plot is temperature data for the chamber during the SPARCS TEC test. The data shows the temperature of the platen and each shroud. At the beginning, the shroud and platen are heated to 78°C and stays there for about 12 hours. The platen is then cooled, and the shroud controls are turned off leaving it to "float."

For the first plateau, the shroud and platen are set to 78°C (Table 4). The platen demonstrates exceptional control exceeding the required stability by maintaining an average temperature of 78.01°C. The narrow standard deviation of 0.04°C and a

Table 4

Table of Chamber Heater Stability Control at Bake Out

		Chamber Heater Control		
Control Zone	Set Temperature (°C)	Mean(°C)	Standard Deviation (°C)	Range (°C)
Zone 1 (Shroud +Y)	78	78.12	±0.16	0.74
Zone 2 (Shroud +Z)	78	78.09	±0.17	0.70
Zone 3 (Shroud -X)	78	78.11	±0.18	0.92
Zone 4 (Shroud -Y)	78	78.29	±0.25	1.20
Zone 5 (Platen)	78	78.01	±0.04	0.32

Note. The table details the performance of the heater thermal control zones in the chamber. Each zone is set to 78°C, the mean temperature, the standard deviation, and the peak-to-peak range for each zone during the first 9-hour hot soak.

maximum peak-to-peak fluctuation of 0.32°C over a 9-hour period further emphasizes its robust stability and control. Similarly, the least effective panel of the shroud (-Y) surpasses the specified requirements, recording an average temperature of 78.29°C, with a standard deviation of 0.25°C and a maximum peak-to-peak variation of 1.2°C.

During this particular test, only the platen underwent active cooling, while the shroud is allowed to thermally "float." Analysis of one of the cold plateaus showcases the consistent stability of the platen. With a setpoint of -46°C, the platen maintained an average temperature of -46.07°C, exhibiting a low standard deviation of 0.09°C and a maximum peak-to-peak fluctuation of 1.11°C (Figure 14). Notably, the maximum peak-

Figure 14

Platen Cold Dwell Temperature vs. Time from the TEC Test

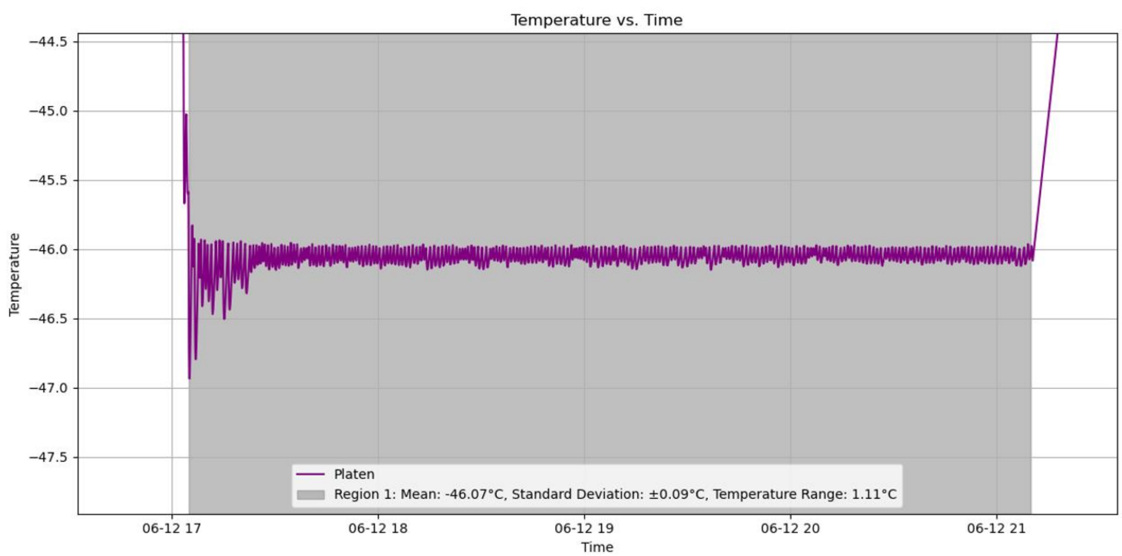

Note. This plot is a zoom in of the third to last cold dwell from the TEC test. The shaded region is what was analyzed. The set temperature was -46°C. The system was able to keep a mean temperature of -46.07 °C with a standard deviation of +/- 0.09 °C and a peak-to-peak temperature range of 1.11 °C. Note that the 1.11°C temperature range was only seen at the beginning of the dwell and the peak-to-peak temperature range significantly dropped as the dwell went on.

to-peak variation occurs at the beginning of the plateau, after which the platen settled into a much smaller peak-to-peak cycle. This analysis of the chamber's thermal performance emphasizes the chamber's robust thermal control capabilities during critical qualification testing of flight hardware.

TVAC Testing for SPARCS

TVAC testing serves the dual purpose of demonstrating unit performance in a relevant environment and identifying any potential workmanship issues. In the context of the SPARCS payload's AI&T process, TVAC testing is conducted in three testing phases.

Phase 1 involves testing the partially assembled payload in a vacuum environment, allowing for detector alignment adjustments. Alignment is done in a vacuum environment, so the atmosphere does not absorb the signal source.

Figure 15

SPARCS Test Flow

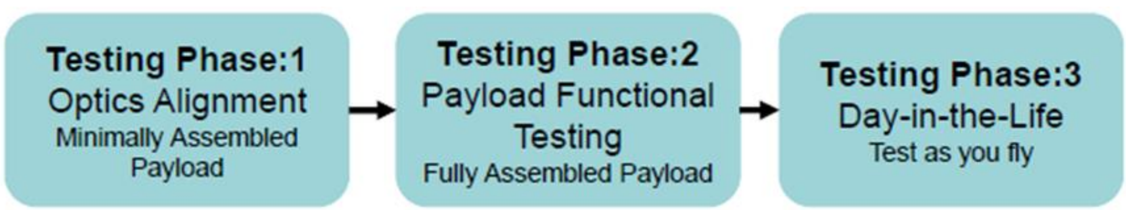

Note. A simplified view of the test phases showing the flow. Phase 1 is the alignment of the optics and verification of the optical alignment; phase 2 is the functional and characterization testing of the fully assembled, and phase 3 is the day-in-the-life test for the payload, which would be accompanied by the typical thermal cycles and thermal balance testing seen in TVAC tests.

Phase 2 marks the full assembly of the payload, during which comprehensive functional testing is performed. This phase establishes a performance baseline for the instrument before workmanship testing commences.

Phase 3 represents the comprehensive TVAC test conducted following the vibration test. In this stage, the payload undergoes thermal cycling, performance testing, and thermal balance tests for model correlation. The results of these performance tests are compared to the baseline data collected in phase 2 to assess potential damage and verify continued adherence to performance requirements.

Test Optics Support Fixture

The optics support stand serves as testing support equipment designed to elevate the optics assembly for testing the SPARCS payload within the vacuum chamber to intercept the diverging light entering the chamber, as seen in Figure 16 (Jensen et al., 2022). The test optics within the chamber simulate a star, facilitated by a monochromator supplying a controlled FUV and NUV light source for calibrating instrument. The initial optic, a pick-off mirror, redirects the light towards an on-axis parabola. This parabola folds the light back upon itself, rendering the diverging rays parallel and focused at infinity to emulate a star. Subsequently, the beam is reflected off a larger second-fold mirror into the payload aperture. The optics support stand must offer stable support for these three optics during chamber testing. Maintaining a consistent distance between the parabola and the monochromator exit is crucial for the focus of the system depth of focus 100 microns. Therefore, the optics are mounted atop a thermally controlled aluminum

Figure 16

Testing Light Source

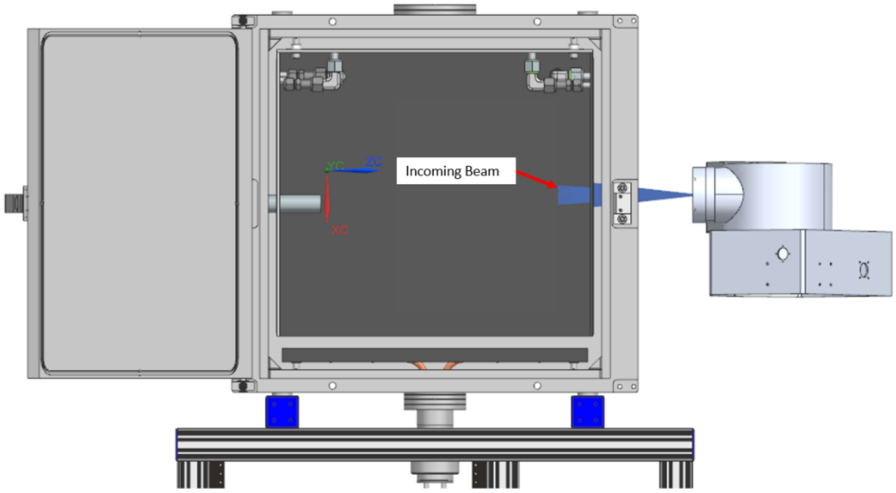

Note. The testing source light beam enters the chamber from the +Z side with the center of the beam 11” above the platen. The optics stand provides a stable platform for to elevate the optics test assembly to intercept the light source.

Figure 17

Test Optics Overview

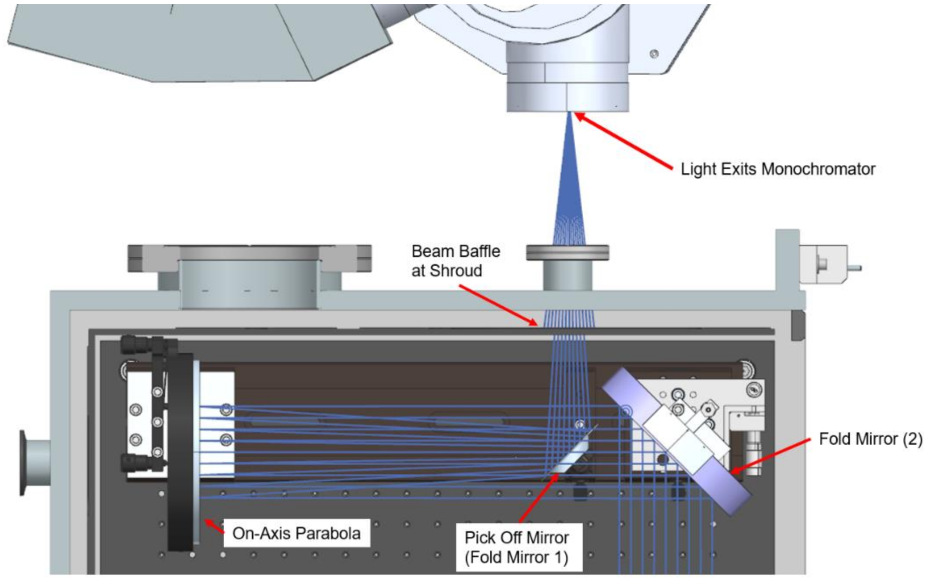

Note. Top-down view of the optics assembly inside the chamber. The light exits the monochromator (note the through tube is hidden in the model) and enters the chamber. The light is stopped down at the thermal shroud. The first fold mirror picks off the beam and sends it toward an on-axis parabola where the light is collimated and send back to the second fold mirror where it is redirected into the payload.

plate, maintained at room temperature (22°C) to minimize path length variations due to temperature changes.

The optics are mounted to a 6061-aluminum optics rail on top of an aluminum plate. The fixture is fixed to the platen and will be cycling from +60°C to -95°C during testing. Such temperature fluctuations cause changes in the optics plate dimensions. Utilizing the linear thermal expansion (The Engineering ToolBox, 2008), the change in length (dL) along an axis can be calculated. The initial length (L_0) is multiplied by the CTE (α) and multiplied by the difference between the final temperature (T_1) and the initial temperature (T_0).

$$dL = L_0 \alpha (T_1 - T_0) \tag{3}$$

The path length between the pick-off mirror and the parabola is about 341 mm, while the CTE of aluminum is 2.238 x 10^{-5} °C^{-1}. If the plate the optics were mounted to were to go from room temperature to -95°C, that would be a change in temperature of -117 °C and result in the path length between the two mirrors shortening by 892 um, 8.92 times the depth of focus. Rewriting the linear thermal expansion equation, the temperature range that the optics rail needs to stay within to preserve the path length between the parabola and pick-off mirror can be calculated.

$$dT = \frac{dL}{L_0 \alpha} \tag{4}$$

Figure 18

Optics Stand Overview

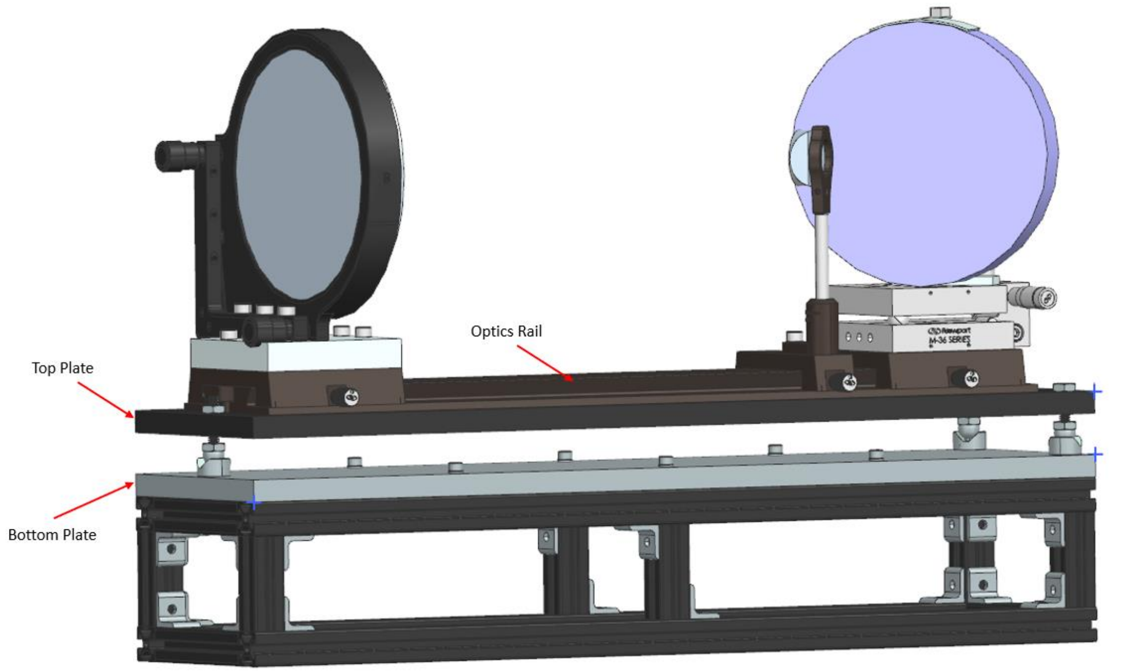

Note. The figure is a view of the full optics stand fixture. The Maxwell kinematic system is located between the top plate and the bottom plate. The top plate is thermally controlled and has the heater on the bottom of the top plate with a control thermocouple on the top surface.

The temperature change that results in a change of length of 100 um is about 13°C. Assuming the system is aligned and focused at 22 °C, the temperature range for the optics rail is 9 °C to 35 °C. To maintain this temperature range, the optics rail is mounted on a thermally controlled aluminum plate. The plate is controlled using an identical heater control system as the chamber, a 58.5 W heater is placed mounted to the bottom of the plate and utilizes a type T thermocouple to provide feedback to the CN616A temperature controller.

Controlling the top plate of the optics stand would create a larger temperature gradient between the base of the stand at the platen and the heated optics plate. To mitigate the thermal stresses and warping caused by the gradient, a Maxwell kinematic system is used to fix the heated plate to the stand. The Maxwell kinematic system is thermally stable and highly repeatable, allowing for repeatable de-mating and mating of the system (Bal-tec, 2023). The Maxwell kinematic system uses three balls in three v-grooves to establish six points of contact to constrain the top to bottom.

The v-groove blocks are placed on the bottom plate (top of the stand) and strategically placed. For proper orientation of the v-grooves, the v-grooves should be placed on the plate so that if one were to draw a line from the center of each v-groove block to create a triangle, the axis of the vee would bisect the angle at the corners of the triangle as seen in Figure 19 (Hale & Slocum, 2001). The balls on the top plate that support the optics should sit at the center of these v-grooves.

Figure 19

Vee Groove Orientation on Optics Stand

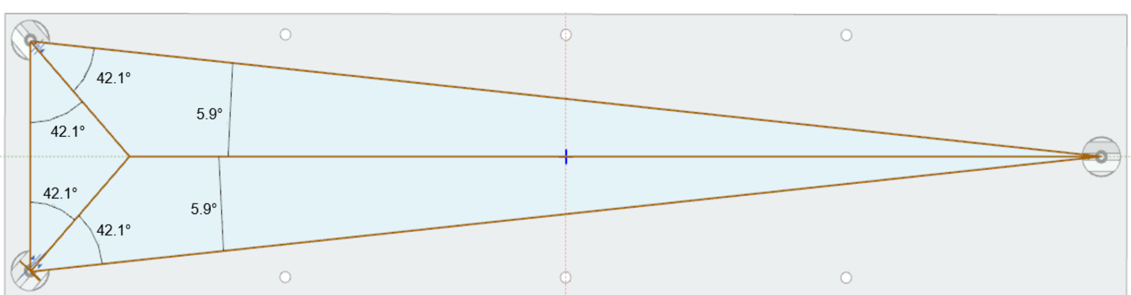

Note. This is a top-down view of the top of the plate with the v-grooves. Drawing a triangle from the centers of each v-groove a triangle is made. Each axis of the v-groove block bisects the angles at each corner of the triangle *(Hale & Slocum, 2001)*.

Figure 20

Vee Groove Installation

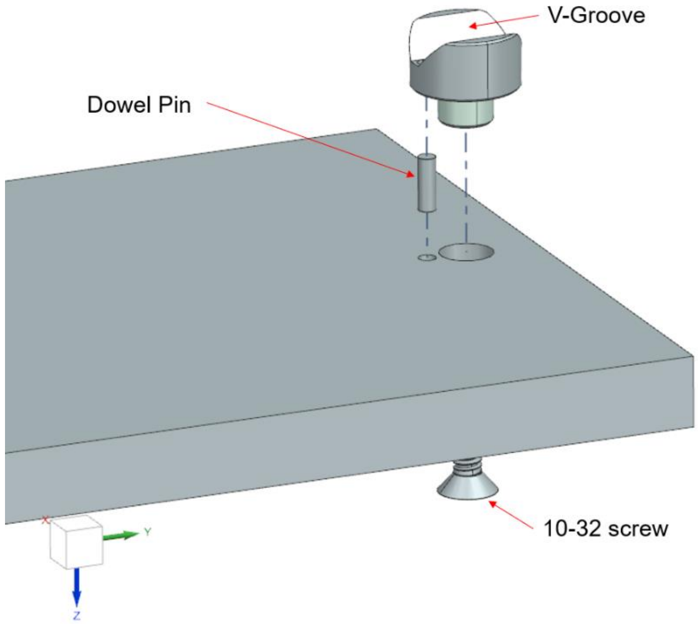

Note. Exploded view of how the v-grooves are positioned, oriented, and fixed to the optics stand.

V-grooves and truncated threaded balls are purchased from Bal-tec for the assembly of the optics stand. The v-grooves have a small shaft at the bottom for locating the groove assembly to the plate, while a dowel pin is used to ensure the orientation of the block is correct (Figure 20). The truncated and threaded balls are used as the spheres and fixed to the top plate. The truncated balls are threaded onto set screws and a lock nut is used to fix the truncated ball to the screw. The set screws are threaded into the top plate allowing for some vertical adjustment of the optics. A lock nut is used on the set screw to the vertical adjustment (Figure 21). Figure 22 shows an exploded view of the optics stand and a view of the optics stand in the chamber during phase 1 assembly.

Figure 21

Vee Groove and Ball Interface

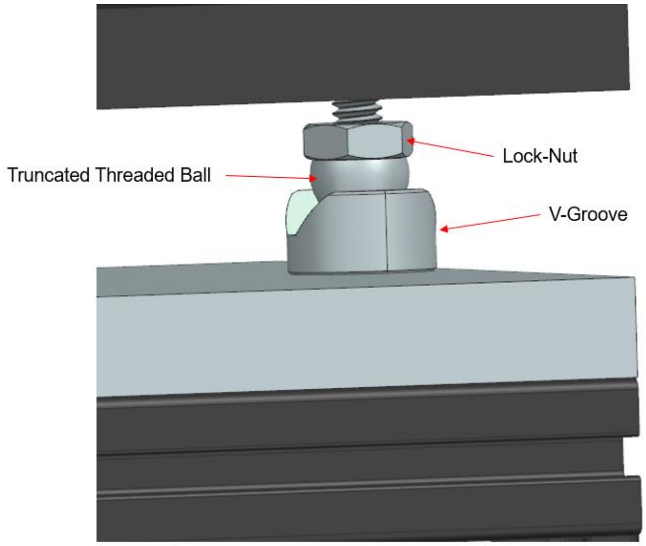

Note. This is a diagram of how the top plate interfaces with the bottom plate of the optics stand. A set screw is threaded into the truncated ball and a lock nut is used to lock the ball onto the screw. The set screw is threaded into the plate. Vertical adjustment is made by threading the set screw in and out. Once vertical adjustments are made, the lock nut is used to lock in the adjustment.

Figure 22

Exploded Optics Stand and Test Setup View

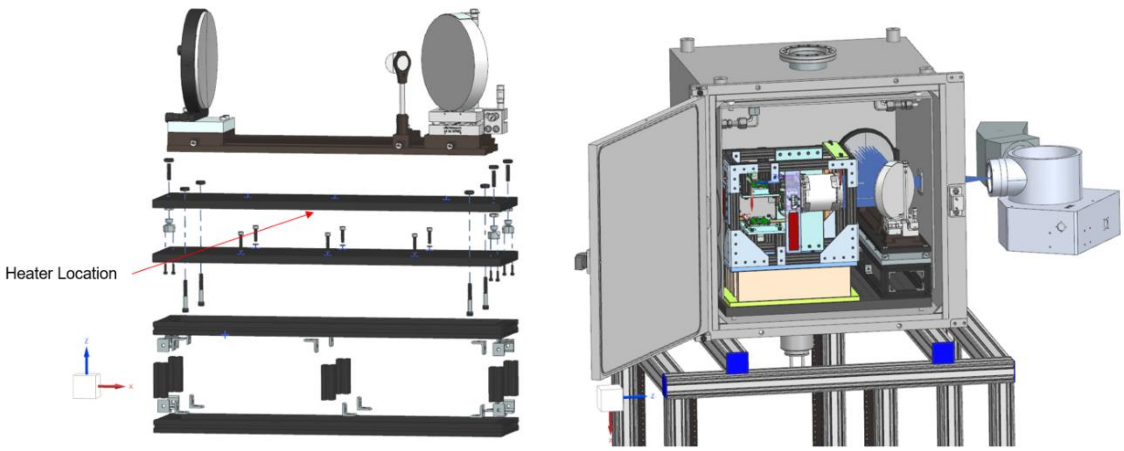

Note. Left is an exploded view of the optics stand. Right is a view of the optics stand in the chamber during phase 1 testing.

Partially Assembled Test Setup

The integration and test fixture is designed to facilitate the assembly and testing of the SPARCS payload during the first phase of testing. In Phase 1 testing, the payload is required to be in a partially assembled configuration, comprising the payload optics assembly (telescope, optics bench, dichroic, and both the FUV and NUV detectors), the detector electronics boards, the power board, the digital signal processor (DSP) board, and the payload processing board (Figure 23). This strategic configuration, resembling an "exploded" state, provides necessary access to the detector header boards for making adjustments to bring the detectors into focus. The detector header boards are directly

Figure 23

Partially Assembled Payload Overview

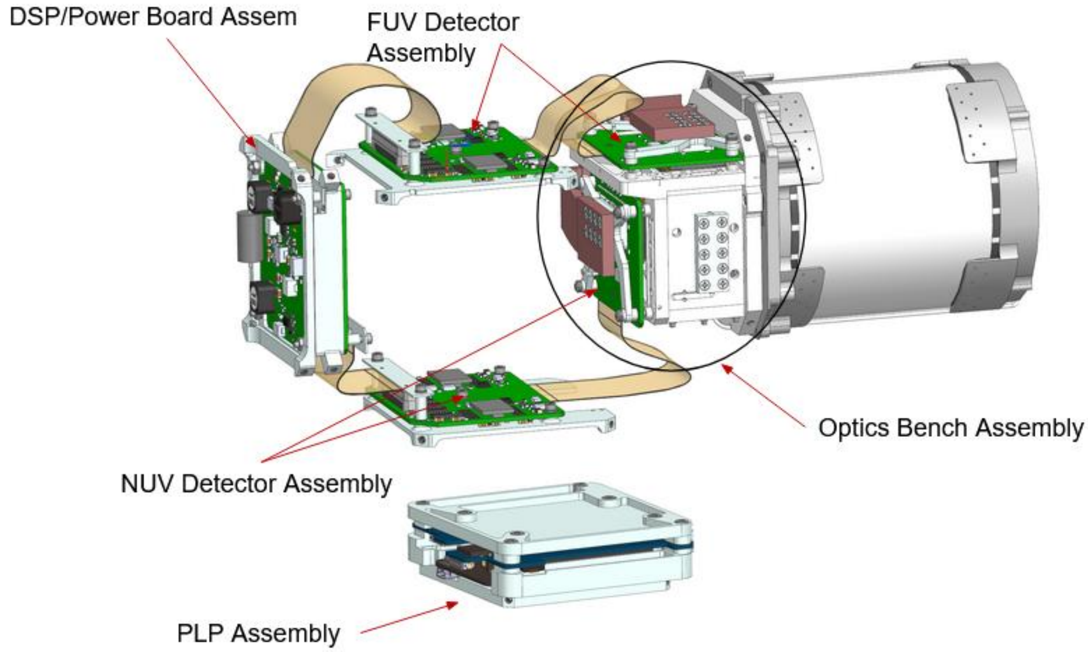

Note. The payload is in a partially assembled state to allow for access to the FUV and NUV detector boards. Access to the NUV and FUV detector boards is required during phase 1 testing in case any adjustments are needed to bring the detectors into focus.

connected to the detector electronics boards through fixed flex cables, while the DSP and power boards are linked using flight flex cables. This configuration limits the bending of the flex cables to reduce cable wear prior to being put into the flight configuration.

The integration and test fixture's design requirements encompass several key aspects:

- Supporting the payload in the partially assembled test configuration for chamber testing.
- Fitting within the dimensions of the purge cabinet (16.6” W x 16.1” D x 11.6” H, with an opening of 16.3” W x 10.7” H).
- Providing flight-like heat sinks (-40 to +60) for the payload hardware.
- Offering support and protection for the payload during assembly.

Constructed with 6061-T6 T-slot extruded aluminum framing, the assembly test fixture is both cost-effective and adaptable. The fixture, measuring 14.25” W x 8.25” D x 11” H, conveniently fits into the purge cabinet for storage on its side (Figure 24). To maintain the necessary configuration, interface plates, and additional aluminum framing are utilized within the fixture. The payload hardware is contained within the fixture frame, allowing rotation on the table during assembly while preventing unintentional use of the hardware as a support. Interface plates, matching the material of the fixture and closely resembling the 7075 aluminum properties used for the payload mounts, securely hold the payload hardware in place. Using 1/4-20 screws and nuts that slide in the rails, the interface plates are directly mounted to the frame rails, providing some adjustability

Figure 24

SPARCS AI&T Fixture Dimensions

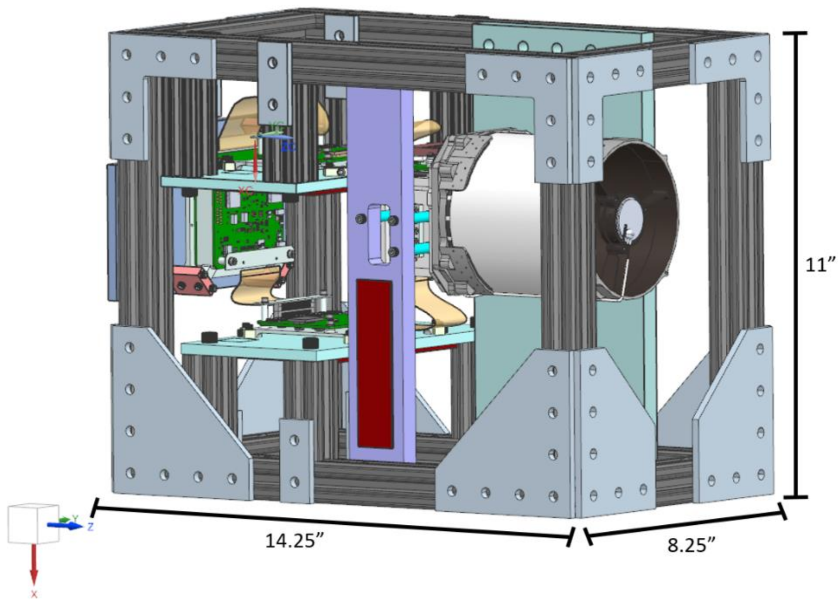

Note. The partially assembled payload is supported in the AI&T fixture. The fixture can easily be fit in the purge cabinet. Each interface has heater control. The optics bench heater can be seen as a red patch in the figure.

in their positioning and ensuring efficient heat transfer away from the hardware due to the matching thermal conductivity of the materials.

The optics bench is securely fixed to its interface plate (5) using three 6-32 screws and standoffs (Figure 25). The standoffs serve the purpose of precisely positioning the telescope in the center of the fixture along the Y-axis, while spacers can be used for refined adjustments. To facilitate access for mounting the optics bench heater, a machined opening is strategically integrated into the design of the interface plate. The design allows for both secure fastening and flexibility in alignment adjustments of the optics bench.

Figure 25

AI&T Fixture, Optics Bench Interface

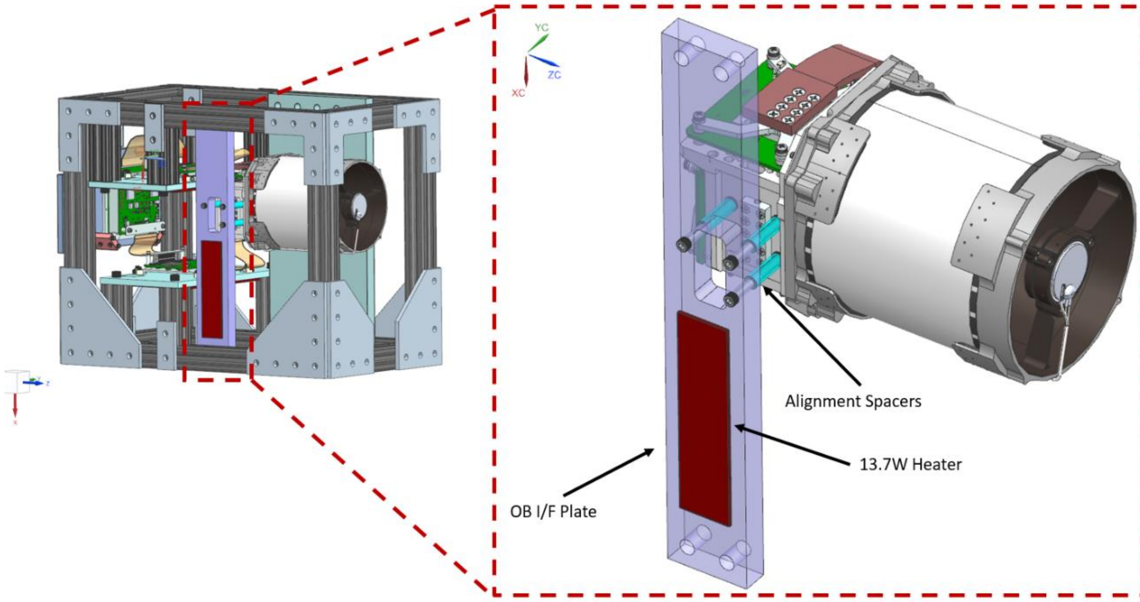

Note. The optics bench interface plate anchors the optics bench in the AI&T fixture. The optics bench is mounted using three 6-32 screws and spacers which are used adjusting the position of the optics bench in the fixture. The interface plate has a 13.7 W heater for heating the plate, with a thermocouple opposite of the heater.

The detector electronics boards require the incorporation of their flight mounts as they provide heat sinks for some of the higher-power chips on the boards. To accommodate the flight mounts, specialized mounting blocks are designed to establish a connection between the flight mounts and the fixture interface plates. These interface plates are securely affixed to aluminum t-slot framing and cut to maintain the desired positions within the fixture. This design provides flight-like thermal paths and structural support for the detector electronics boards and their flight mounts during phase 1 of integration and testing (Figure 26).

Figure 26

AI&T Fixture, Detector Interface Plate

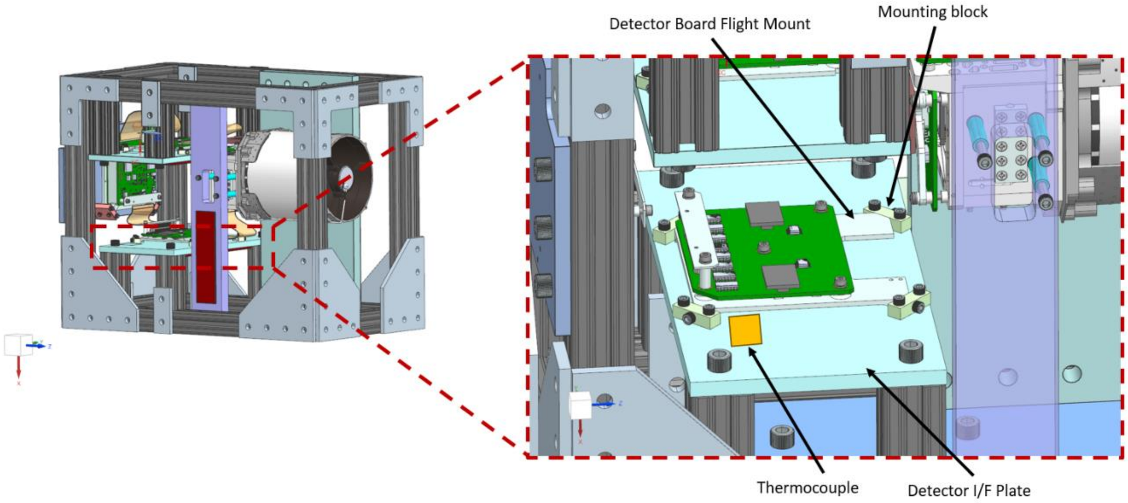

Note. The detector electronics boards are fixed to their flight mounts as the flight mounts provide thermal paths for some of the “high” power chips on the boards. A thermocouple is placed next to a mounting block so the sink temperature for the flight mount is known. Opposite of the thermocouple is a heater to provide a controlled sink temperature when the system is cold biased.

Similarly, the DSP and power boards, consolidated within their flight mount, also require specialized mounting to the interface plate located on the back of the fixture (Figure 49). To address this requirement, large mounting blocks are designed to accommodate the secure attachment of the DSP/power board flight mount to the interface plate. This approach provides a thermal path to the interface plate, similar to flight and structural support for the DSP/power board assembly.

Figure 27

AI&T Fixture, DSP Assembly Interface

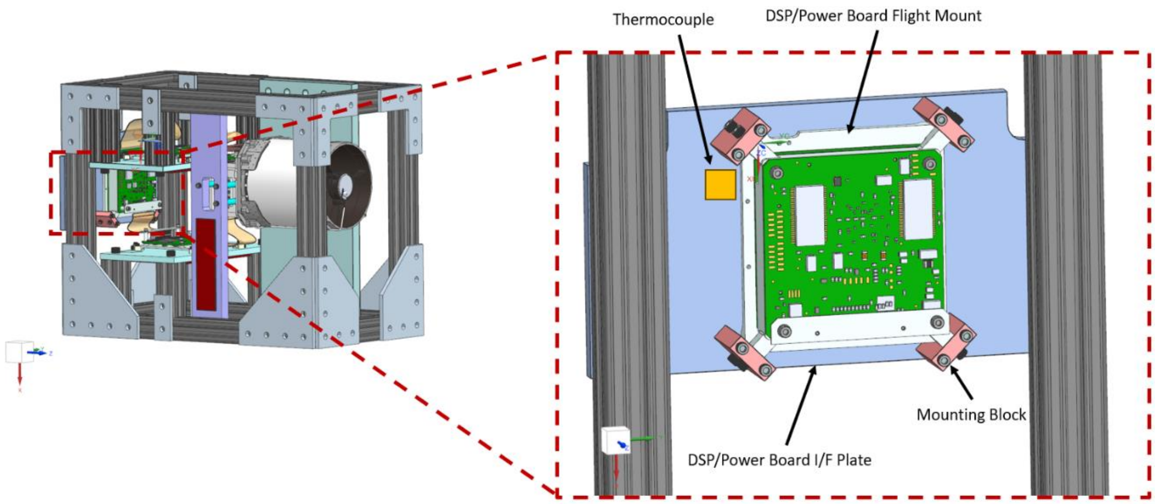

Note. The DSP electronics boards are fixed to their flight mounts so the nominal thermal path for the boards are used to dissipate heat out to the interface plate. The interface plate has a thermocouple near one of the mounting blocks to collect the sink temperature during testing and used for controlling the interface plate temperature with the heater on the opposite side.

The interface plate for the TEC provides a thermal path for the detector cooling system and is designed to simulate the dedicated spacecraft payload radiator (Figure 28). The TEC I/F is designed to be larger in order to provide a heat sink with a larger thermal mass to reduce temperature instability, while the large profile provides a better thermal path to the rails where the heat will eventually make it to the chamber platen, which leaves the system. To simplify the manufacturing of the TEC interface plate, it was broken up into two parts. The TEC thermal path (Figure 28) is fixed to the TEC mount using the same sixteen 2-56 screw points as in flight. The TEC thermal path is then fixed to the interface plate with six 6-32 screws to ensure good thermal contact between the two parts.

Figure 28

AI&T Fixture, TEC Interface

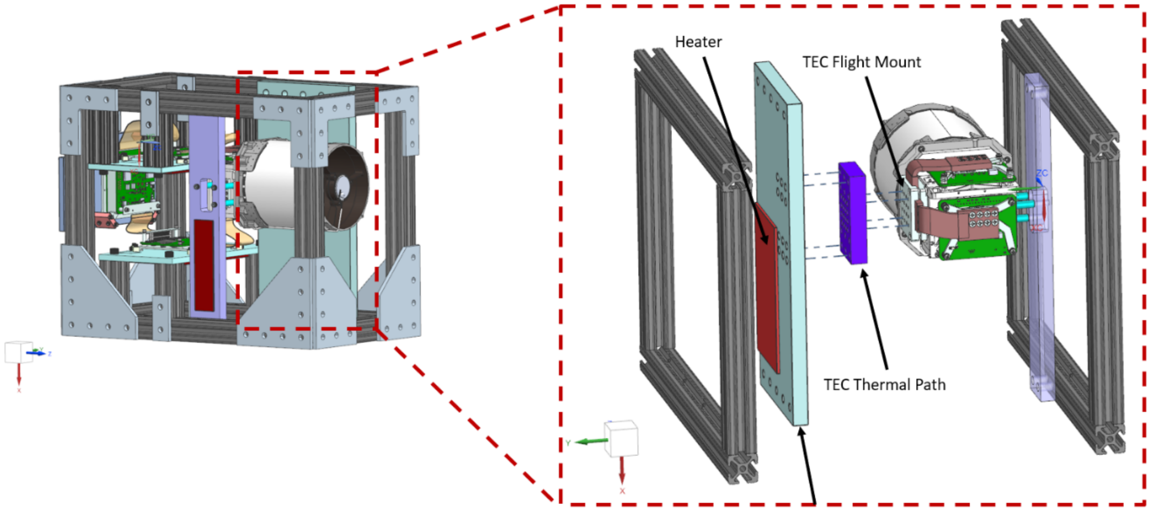

Note. The TEC interface plate has an extra block (TEC Thermal Path) that interfaces with the payload TEC mount with sixteen 2-56 screws. The TEC thermal path block mounts to the TEC interface plate which can maintain control when cold biased. A thermocouple is located on the interface plate next to the thermal path block and is used to control the heater on the back side of the plate.

For testing in the chamber, the fixture is securely fastened to an aluminum booster seat comprised of 6061 aluminum blocks and plates. The foundation is established by the bottom plate, ensuring robust thermal contact. Aluminum bars, affixed to the bottom plate through five evenly spaced ¼-20 screws each, enhance structural integrity. Atop these blocks is an aluminum plate, serving as a platform for mounting the assembly and test fixture using sixteen ¼-20 screws. The booster seat functions as a pedestal, positioning the test fixture within the chamber at the required height for test light to pass through the aperture. Additionally, it facilitates a thermal path to the platen, contributing to efficient temperature management during testing.

During the initial planning stages for phase 1 testing, it is determined that the detectors need to be cooled to their operational temperature range (-35°C to -40°C) for taking images during the alignment test. To achieve this, the thermal strategy involves cold biasing the system by utilizing LN2 to cool the platen. With the system cold-biased, it allows for precise control of the interface plates using the installed heaters. Cooling the platen to a lower temperature than the hardware offers an additional advantage in contamination control: any residual contaminants in the chamber after bake-out were more likely to condense on the platen rather than on the contamination-sensitive hardware.

The test fixture comprises five independently controlled heating zones, with a central control system anchored by a 6-channel Omega CN616A temperature controller, mirroring the setup for regulating chamber temperatures. Unused heaters from the chamber shrouds and platen are repurposed for the TEC, DSP/Power, and Detector interface plates. Additionally, the optics bench interface plate incorporated a smaller Kapton heater for improved fitment.

Zone 1, located on the optics bench interface plate, features a 13.7W heater capacity powered by an 18V supply and utilizes a type T thermocouple for control sensing. Zones 2 through 6, situated on the DSP/Power board interface plate, the TEC interface plate, and the NUV and FUV detector board interface plates, each boast a 58.5W heater capacity. These zones are powered by 48V supplies and employ type T thermocouples for control sensing, strategically positioned near mounting blocks to monitor the interface temperatures of the flight hardware accurately. The PID heater control within the CN616A controller is utilized across all six heater zones for precise temperature regulation.

A thermal model was built to offer valuable insights into the prospective performance of the test fixture during phase 1 testing and to forecast the requisite cooling of the platen. Leveraging the CAD model in NX, a finite element mesh (FEM) is made via the NX mesh software based on simplified idealized parts (Figure 29). To streamline the model, the payload was deliberately excluded, with the focus solely directed towards

Figure 29

AI&T Fixture FEM

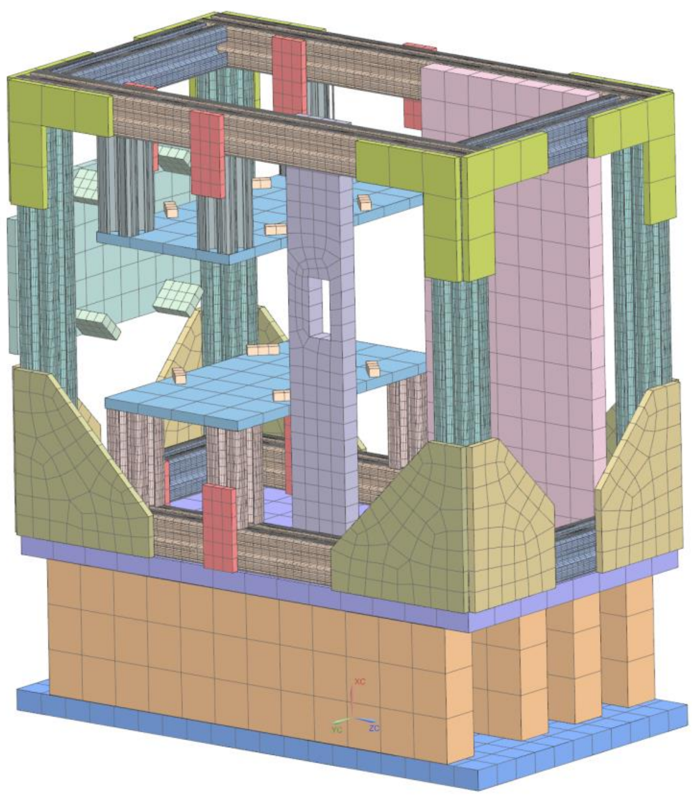

Note. The figure shows the mesh used for the thermal model of the test fixture in the partially assembled payload test configuration.

the test assembly fixture. This strategic choice was underpinned by the assumption that the test fixture and chamber exert the primary influence on temperatures. With the payload in the fixture the cooling times are expected to increase due to the extra thermal mass. idealized representations of each component were initially devised using the wave function to replicate the part, coupled with synchronized modeling techniques. This process deliberately omitted intricate details such as screw holes, chambers, and minor radii, aiming to minimize mesh complexity by reducing the number of elements and nodes. Subsequently, each part was meshed and interconnected, culminating in the formation of a comprehensive FEM assembly.

Thermo-physical and thermo-optical properties were assigned to each mesh (Table 5). The thermophysical properties, encompassing conductivity, density, and specific heat for 6061 aluminum, were assigned using the NX library, with material values cross-referenced with the *Spacecraft Thermal Control Handbook* (Gilmore, 2002). Determining

Table 5

AI&T Fixture Property Assignment

Part	Material	Thermal Conductivity @ 20 °C, W/mK	Density, kg/m^2	Specific Heat, J/kgK	Thermal Emissivity
T-Slot Rails	Black Anodized Al 6061	154	2711	896	0.86
T-Slot Mounts	Uncoated Al 6061	154	2711	896	0.15
Interface Plates	Uncoated Al 6061	154	2711	896	0.15
Mounting Blocks	Uncoated Al 6061	154	2711	896	0.15
Booster Seat	Uncoated Al 6061	154	2711	896	0.15
Chamber Shrouds	Z306 Black Paint	---	---	---	0.87

Note. This table gives the values and assignments used for materials' thermal conductivity, density, specific heat, and thermal emissivity.

the thermal emissivity can be challenging due to variable surface conditions and manufacturing processes. For uncoated bare aluminum, thermal emissivity typically spans from 0.09 to 0.31, with commercial-grade sheets tending towards the lower end and heavily oxidized surfaces towards the higher end (The Engineering ToolBox, 2003). The thermal emissivity of black anodized aluminum is subject to considerable variation based on the coating processes employed. A thermal emissivity of 0.86 was thus adopted for the black anodized rails, derived from averaged values of test samples cited in the Spacecraft Thermal Control Handbook (Gilmore, 2002).

In the simulation, thermal contacts are established to interconnect each mesh with specified conductance values (Table 6). Notably, when addressing the anodized T-slot frame rails, the anodization process introduces additional contact resistance, influencing overall conductance. The thermal conductance between bare and anodized aluminum surfaces is contingent upon factors such as anodization type, contact pressure, and coating thickness. The T-slot frame rails, featuring a Type II anodize coating with a thickness typically ranging from 7 to 33.7 microns, exhibit interface conductance variability between 110 and 3000 W/m^{2}K (Lambert et al., 1995). To accommodate this variability, an average conductance value of 1555 W/m2K was utilized in the model. Calculating the total conductance for all contact areas between the rails and a plate involved determining the contact area from the CAD model and multiplying it by the average conductance value. After the first rounds of TVAC testing with a thermal balance, the conductance values can be fine-tuned to better match the actual conductance seen in testing.

Table 6

AI&T Fixture Model Conductances

From	To	Contact Area, m^2	Conductance, W/m^2K	Total Conductance, W/K
TEC I/F Plate +X End	Rail	0.001011	1555	1.57
TEC I/F Plate -X End	Rail	0.001011	1555	1.57
T-Slot Bracket (0.875”)	Rail	0.000177	1555	0.28
T-Slot Bracket (1”)	Rail	0.000202	1555	0.31
T-Slot L Bracket Med Side (2”)	Rail	0.000405	1555	0.63
T-Slot L Bracket Long Side (3”)	Rail	0.000607	1555	0.94
T-Slot Triangle Bracket Short (4”)	Rail	0.000809	1555	1.26
OB I/F Plate +X End	Rail	0.000324	1555	0.50
OB I/F Plate -X End	Rail	0.000324	1555	0.50
DSP/Power Board I/F Plate +Y Side	Rail	0.000657	1555	1.02
DSP/Power Board I/F Plate -Y Side	Rail	0.000657	1555	1.02
Booster Seat top	Rail	0.002441	1555	3.80
Detector Blocks	Detector I/F Plate	---	---	0.52
Booster Top Plate	Booster Bars	---	---	17.55
Booster Bottom Plate	Booster Bars	---	---	17.55
DSP Blocks	DSP I/F Plate	---	---	0.52

Note. All of the conductance values for the parts to the rails assumed bare uncoated aluminum to anodized aluminum surface-to-surface contacts found in Lambert et al.

The detector and DSP blocks to the interface plates are assuming two 4-40 screws.

The booster seat bars to the booster seat plates are assuming five 1/4-20 screws.

Conductance values for aluminum-to-aluminum screwed joints can be found in the *Spacecraft Thermal Control Handbook.*

To establish the total conductance between the booster seat blocks and the interface plate mounting blocks, bolt conductance values were referenced from the Spacecraft Thermal Control Handbook (Gilmore, 2002). Mounting blocks on the DSP/Power board interface plate and the detector electronics board interface plates were affixed to the interface plate using two 4-40 screws, each with a conductance of 0.26 W/K. Consequently, the total conductance of each block to the interface plate is 0.52 W/K.

Employing analogous guidelines, the conductance of a ¼-20 screw was determined to be 3.51 W/K.

A steady-state model is developed to ascertain the temperatures that each of the interface plates would attain given the platen temperature. In this model, it is assumed that each interface plate would bear a 3W heater load. This 3W value is chosen for the coldest case scenario, ensuring that the TEC interface plate would reach the minimum temperature expected for the spacecraft radiator during operation. Each heater possesses the capability to deliver more power to control warmer temperatures if required.

It is anticipated that each of the boards would dissipate less than 3W, with the heaters controlled using PID control. As soon as the electronics boards begin to dissipate heat, the power to the heaters would be diminished to sustain the temperature of the interface plates. Given the maximum heat dissipation of each board to be approximately 1.5W, there remains 1.5W of heater control power for ensuring the heaters maintain control of the temperature of the interface plates.

The boundary conditions for the model include the radiative environment and the interface between the platen and the bottom of the booster seat. The radiative environment is set at 5°C, based on the temperatures recorded from the TEC test shrouds. Should the shrouds drift colder, the heaters would utilize more power. With only 3W being used, the duty cycle sits at approximately 22% for the optics bench interface plate heater and about 5% for the other interface plates, leaving a significant margin in heater power if additional power is required.

At the interface between the platen and the bottom of the booster seat, the assumed temperature to which the platen is being controlled is set. In this case, the platen is controlled to -80°C. With the platen at -80°C, the interface plates are capable of attaining their set points with a 3W heat load, facilitating control of the interface plate temperature (Figure 30). The TEC interface plate reaches -37°C, while the NUV, FUV, and DSP interface plates attain temperatures of -28°C, 0°C, and -21°C, respectively, ensuring that all boards have a cold heat sink for operation (Figure 30).

Figure 30

AI&T Fixture, Steady-State Results

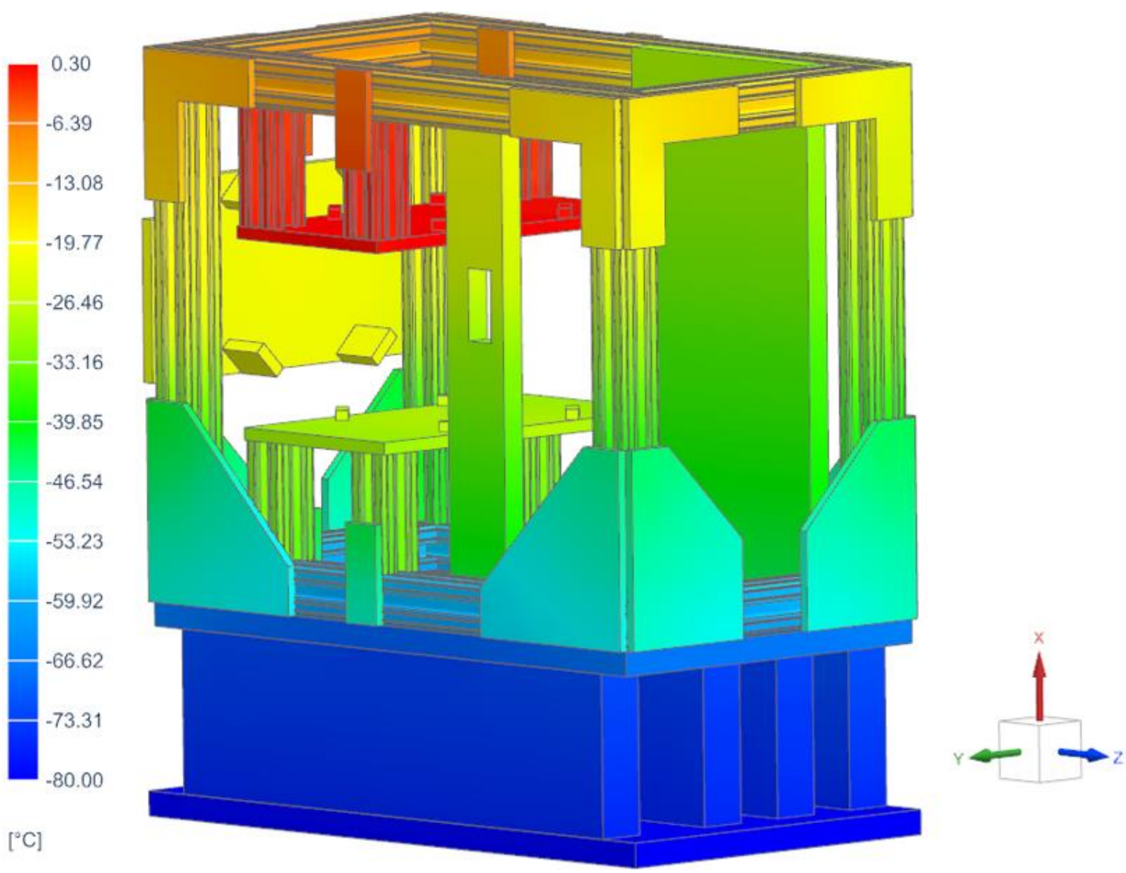

Note. The figure shows the steady-state temperature results for the AI&T test fixture. The base of the booster seat is held at -80°C, and the radiative environment is 5°C.

A transient model was executed with identical assumptions, except for the boundary temperatures at the platen and booster seat interface, which decrease from 22°C to -80°C at a rate of 1°C/min, and the radiative environment cools from 22°C to 5°C at a rate of 0.5°C/min. This scenario was utilized to estimate the predicted cool-down time for the test. Understanding the cooldown time for the system aids the team in planning the testing schedule effectively. The model results indicate that the interface plates take approximately 2.5 hours to approach within 2°C of the temperatures predicted by the steady-state analysis (Figure 31).

Figure 31

AI&T Fixture, Transient Results Cool Down

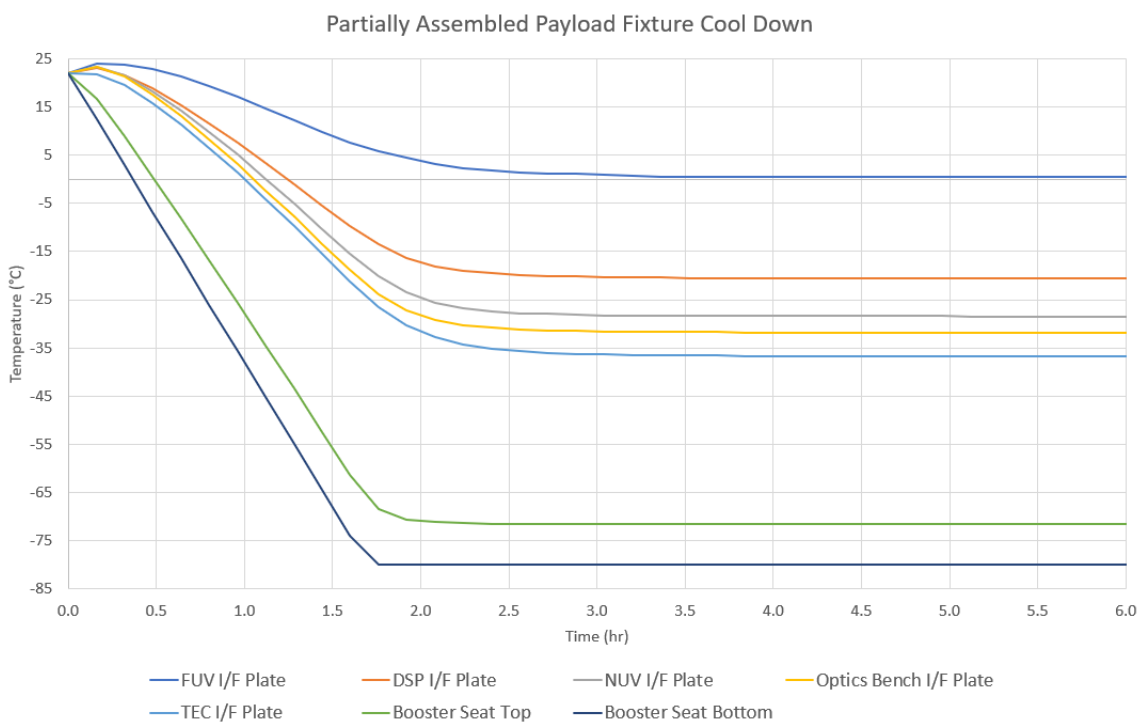

Note. This figure is a plot of the temperature over time with the platen cooling at a rate of 1°C/min showing how fast the interface plates cool given the boundary conditions.

Full Assembly Test Setup

The fully assembled payload test setup comprises the payload in its entirety, utilizing the same test fixture as in the partially assembled setup. However, in the MGSE (Mechanical Ground Support Equipment) setup, there are alterations in the interface plates for the payload to interface with. When the payload is fully assembled, two interface plates are employed to secure it to the structure. The TEC plate is retained from Phase 1 testing, while a new interface plate is introduced to structurally mount the payload.

Integration of the payload onto the structural interface plate involves the use of eight 6-32 screws. Similar to the other plates used in Phase 1, the structural interface plate is constructed from 6061 aluminum and incorporates a heater for temperature control, simulating the expected spacecraft interface temperature. Notably, the payload structural plate features a cutout just below the surface where the payload mounts, facilitating the placement of the control thermocouple. This thermocouple is strategically positioned just beneath the interface surface to enable temperature sensing and control as close to the interface as possible.

The FEM model utilized in Phase 1 testing underwent modifications to align with the Phase 2 test setup. The model was executed in a manner akin to the Phase 1 setup, with two primary boundary conditions: the radiative environment and the interface between the pallet and the bottom plate. The radiative environment is assumed to decrease to 5°C, consistent with previous tests where the platen was cooled for TEC testing.

The coldest controlled case for the fixture to operate with the payload is during cold operation. In this scenario, the payload TEC interface is set to -40°C, while the payload spacecraft interface is -20°C (Figure 32). To achieve these temperatures while ensuring a minimum of 3W heater control on the TEC interface plate, the platen needed to be cooled to -95°C. Consequently, the TEC interface plate reached -40°C, while the

Figure 32

AI&T Fixture, Phase 2 Steady-State Results

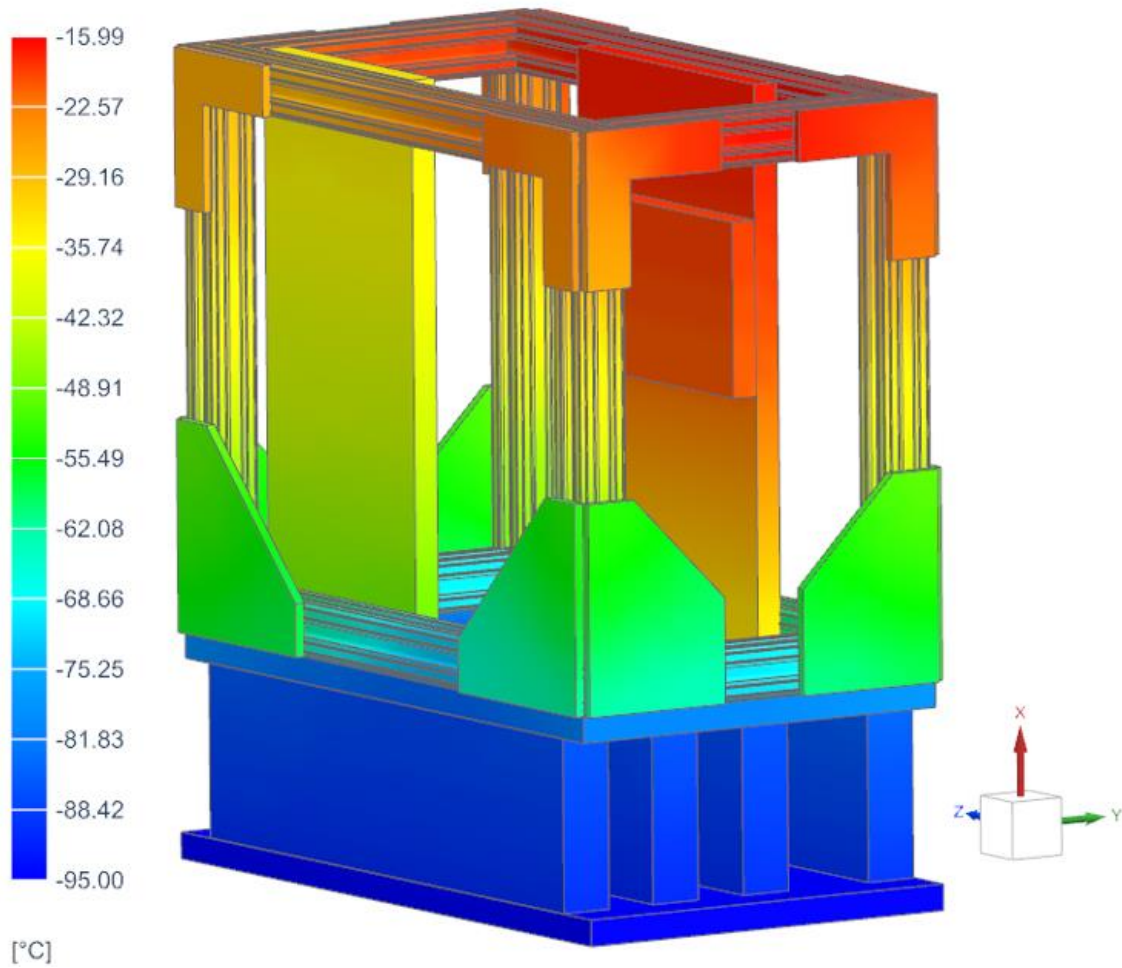

Note. This figure shows the temperature results mapped over the FEM model. The bottom of the booster seat is set at -95°C. The goal of this analysis is to get the TEC interface plate to -40°C and the payload interface plate to -20°C.

payload interface plate attained -20°C with a 30W heat load (51% duty cycle).

A transient case is executed to estimate the time required for the interface plates to reach the lowest testing temperatures. The platen was cooled from room temperature to -95°C at a rate of 1°C/min, while the radiative environment was gradually cooled to 5°C at a rate of 5°C/min (Figure 33). Under these conditions, it was determined that the interface plates would take approximately 2.5 hours to approach within 2°C of the target temperatures.

Figure 33

AI&T Fixture, Phase 2 Transient Results

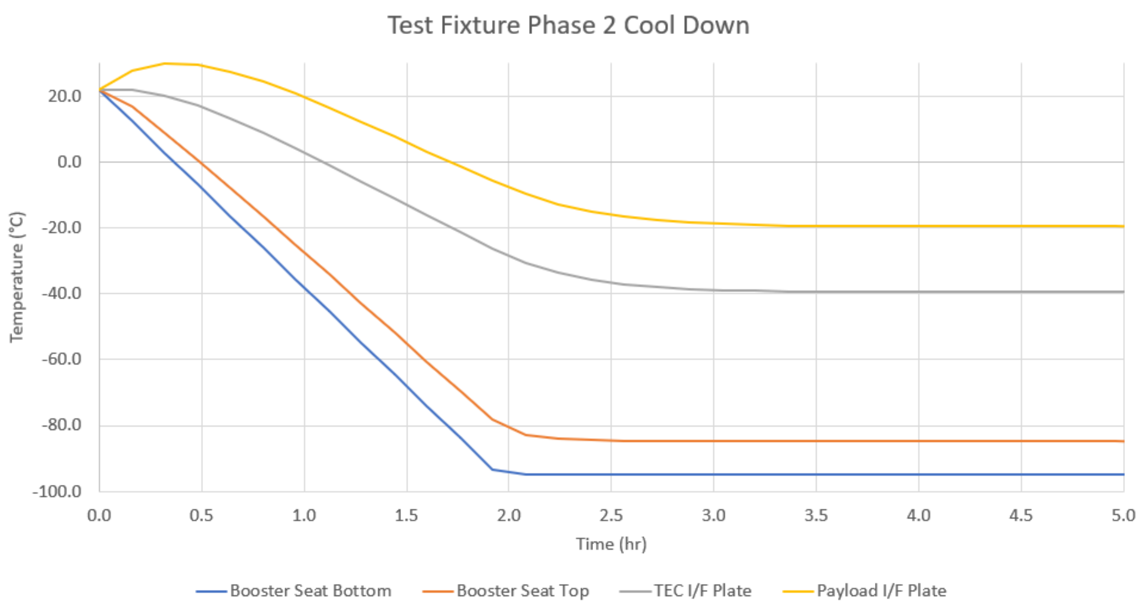

Note. The plot shows the cool down time for the test fixture. With the payload it would be expected to be slightly longer due to the extra thermal mass added to the assembly.

SPARCS Summary

The culmination of efforts on SPARCS has yielded a tailored thermal vacuum chamber specifically designed for CubeSat missions, boasting the capability to attain and sustain cleanliness levels essential for instruments with stringent contamination constraints, particularly those in the far ultraviolet spectrum. This chamber serves as a reliable platform for hardware bake-outs, contamination measurement, and thermal vacuum testing campaigns, ensuring the performance and resilience of future CubeSat endeavors at ASU.

Each project utilizing the chamber necessitates unique mechanical and ground support hardware tailored to its unique requirements. New and unique ground support hardware is always needed to meet the distinct mechanical demands of upcoming missions. Ground support hardware tailored for the SPARCS mission has undergone analysis, fabrication, and integration, now seamlessly facilitating the AI&T processes of SPARCS.

CHAPTER 3

MECHANICAL AND THERMAL DESIGN CONSIDERATIONS FOR THE STRUVE CUBESAT MISSION

Motivation Behind Struve Work

STRUVE is a proposed Heliophysics CubeSat mission designed to investigate the magnetized plasma of the solar atmosphere. Its primary objective is to enhance our comprehension of the energy accumulation and storage processes within the solar chromosphere, leading to eventual releases via flares and coronal mass ejections. The STRUVE instrument, a slit-scanning, full-Stokes spectropolarimeter, is tasked with observing the sun (Berner et al., 2022). Funded through the NASA H-FOS program, this backing enabled the team to refine instrument requirements for achieving scientific objectives, as well as explore how these requirements could be met using the CubeSat platform.

Figure 34

Functional Block Diagram of the STRUVE Instrument Optics

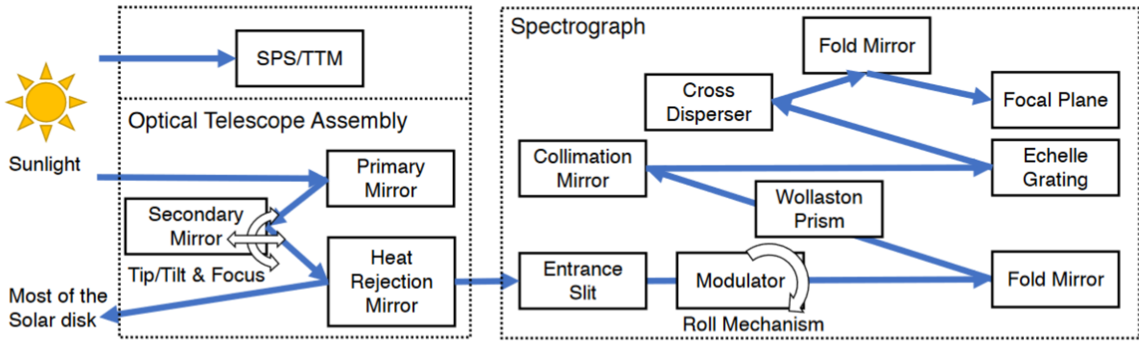

Note. Figure by Robert Woodruff (Berner et al., 2022).

During the concept study phase, requirements are better defined, and collaboration with Space Inventor aided in understanding CubeSat configurations. Space inventor is an aerospace vendor who specializes in delivering off the shelf and custom CubeSat spacecraft buses for CubeSat payloads. Early assessments revealed that a 6U CubeSat was insufficient to physically accommodate the instrument volume, prompting a transition to the larger 12U CubeSat chassis. This upgrade facilitated a larger telescope, thereby enhancing instrument spatial resolution with minimal trade-offs. Light enters the telescope assembly, passes through the entrance slit, and then proceeds to the modulator. The modulator and detector work in tandem to measure polarization by executing eight exposures during a polarimetric modulation cycle (~0.8s) that can subsequently be used to find the four Stokes parameters that describe the polarization of the light (Berner et al., 2022).

The precision of polarimetric measurements is critical for addressing STRUVE's scientific inquiries and dictates accuracy and crosstalk requirements, which, in turn, influence overall stability needs. Image motion at the slit or detector may cause signal detection in a pixel to originate from different sources, impacting the accuracy of Stokes parameters. Jitter primarily affects image motion, though significant temperature variations during observations can also play a role.

This contribution to the STRUVE concept study involves packaging the instrument within a 12U CubeSat volume, ensuring space for typical avionics while establishing an initial design for the instrument's opto-mechanical mounts. Additionally, an analysis of the spacecraft and instrument's thermal environment is done to identify factors potentially affecting thermal stability and ensure the survivability of the hardware such as the sun pointing telescope.

Structural Model Concept

A CAD model is constructed for the STRUVE instrument as a proof of concept. This proof of concept aimed to create a realistic representation of the instrument to provide the team with insights into the potential opto-mechanical system's appearance and to support various optical components. The model served several purposes, including generating more accurate mass estimates, demonstrating how the instrument could fit within the 12U chassis, and devising strategies for optic mounting.

Figure 35

STRUVE CubeSat Volume Boundary Box

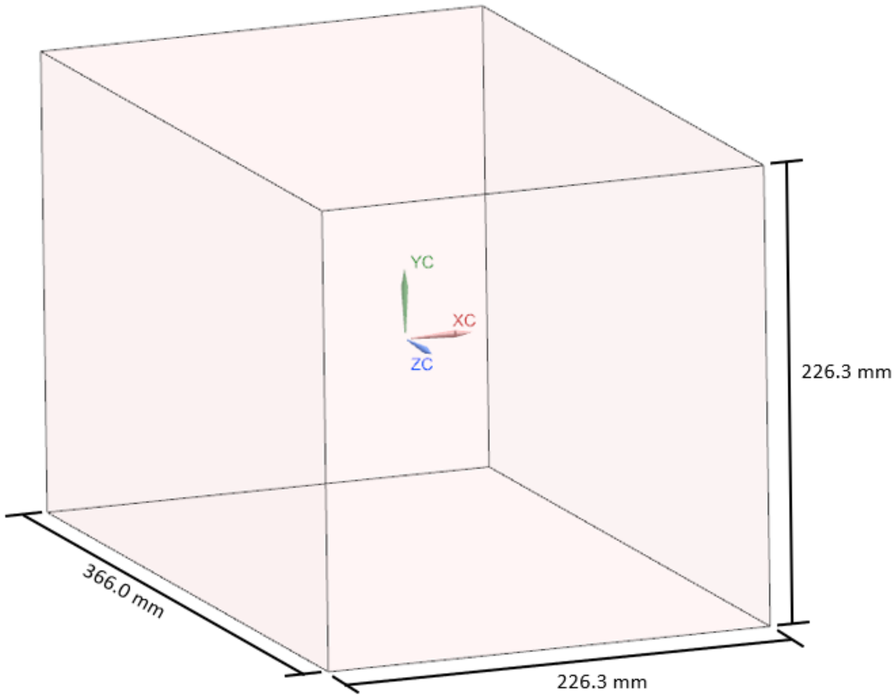

The initial step in building the CAD model involved creating a bounding box based on the dimensions outlined in the CubeSat Design Specification REV 14.1 (CDS) (California Polytechnic State University, 2022). The CDS was developed to establish baseline requirements for CubeSat developers to ensure compatibility with CubeSat dispensers and launch opportunities. According to the CDS specifications, a 12U CubeSat size measures 226.3 mm along the X-axis, 226.3 mm along the Y-axis, and 366.0 mm along the Z-axis.

Figure 36

STRUVE CubeSat Volume Boundary Box with Optics Zemax Model

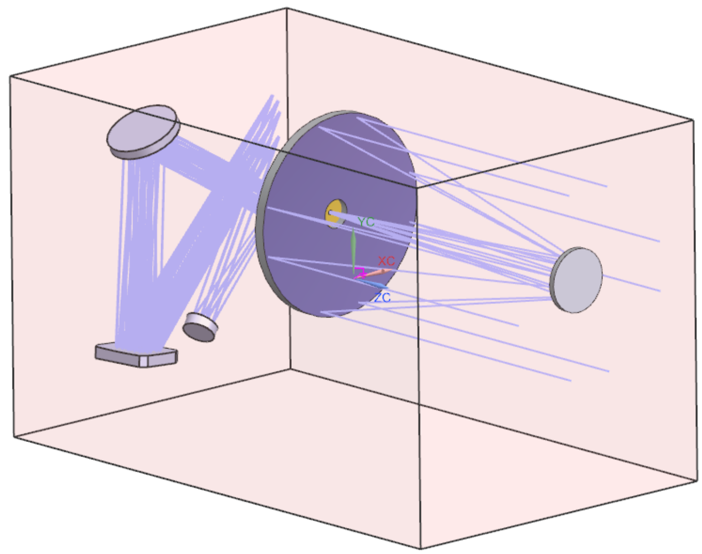

The volumetric box serves as a tool to provide feedback to the team regarding the size constraints of the optics system. The initial step involves iterative collaboration with the optics designer (Robert Woodruff) to ensure that the optics for the instrument could fit within the designated volume. After several iterations, a consensus is reached, resulting in the configuration depicted in Figure 36. This instrument design equipped STRUVE with a relatively large telescope for a CubeSat, featuring a 126 mm diameter primary mirror. Such a telescope aperture enabled STRUVE to meet the SNR requirement with the baselined 1.25” slit width and spatial sampling, with a significant margin.

Figure 37

STRUVE CubeSat and Instrument Volume Boundary Boxes

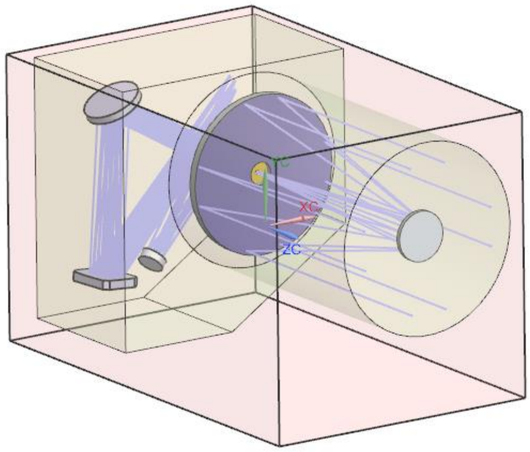

Note. The red box is the spacecraft volume while the green outline is the proposed instrument volume and the bounding box for building the instrument model.

Subsequently, a bounding box is drawn for the optics assembly and telescope to fit inside. This volume serves as a reference for allocating space within the spacecraft between the avionics and the instrument (Figure 37). This second bounding box delineates a space for determining the placement of much of the avionics within the spacecraft. It is important to note that while the majority of the avionics and hardware placement is conceptual, involving the spacecraft vendor early in the process is crucial for finalizing these decisions. Throughout much of the concept study and proposal phases, the STRUVE team collaborated with Space Inventor.

Table 7

STRUVE Spacecraft Hardware

Component	Quantity	Length (mm)	Width (mm)	Height (mm)	Unit Mass (g)
Battery Conditioner	1	91.14	94	11	180
Battery	2	91.14	94	41.2	655
Power Distribution	2	91.14	94	20	138
On Board Computer	1	91.14	94	13	120
S-Band Radio	2	91.14	94	11	120
Momentum Wheel	4	60	60	45	350
Star Tracker	2	60	60	116	300
Fine Sun Sensor	5	40	20	10	N/A
Torque Bar	3	200	Ø17		300

Using the hardware dimensions obtained from the Space Inventor website (*12u Satellite - Space Inventor*, n.d.), simplified volumetric models of the expected hardware were created. These volumetric blocks are strategically placed around the spacecraft, particularly around the instrument, to ensure sufficient room for the hardware, as illustrated in Figure 38. The hardware accounted for and located within the spacecraft is listed in Table 7. With proper organization, it is conceivable to accommodate all spacecraft avionics inside the 12U bus along with the relatively large STRUVE instrument.

The instrument optics assembly is complex, comprising eleven optical surfaces, including the detector. The telescope is mounted to a titanium (Ti-6Al-4V) optics bench, chosen as the baseline material for its relatively low CTE of 8.8×10^{-6} °C^{-1}, compared to

Figure 38

STRUVE CubeSat Assembly Organization

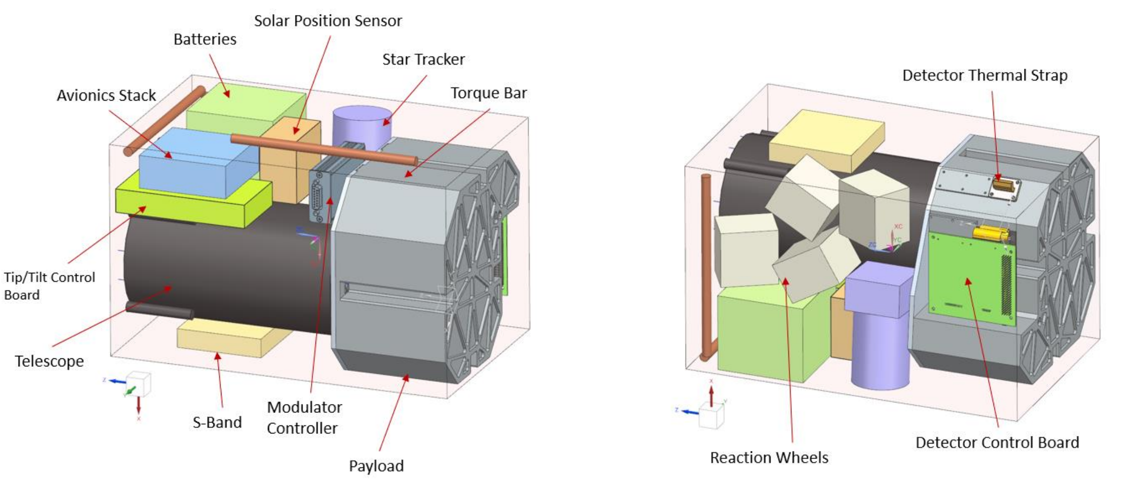

Note. Volumetric blocks of Space Inventor hardware are placed around the instrument to verify the blocks can fit and there is room for the necessary hardware.

aluminum's 23.6×10^{-6} °C^{-1} (Yoder, 2008). If future analysis indicates a need for an even lower CTE, Invar 36, with a CTE of 1.26×10^{-6} °C^{-1}, could be considered.

Zerodur glass is assumed to be the working material for the optics due to its extremely low CTE of $0 \pm 0.05 \times 10^{-6}$ °C^{-1}. This low CTE ensures minimal changes in the system's optical properties due to temperature fluctuations, with any changes primarily attributed to the optics mounts or stresses applied to the optics themselves.

Moving forward, significant effort was dedicated to determining how the optics would be mounted to the optics bench, with careful consideration given to ensure stability and precision in the mechanical model.

Figure 39

STRUVE Optics Assembly Overview

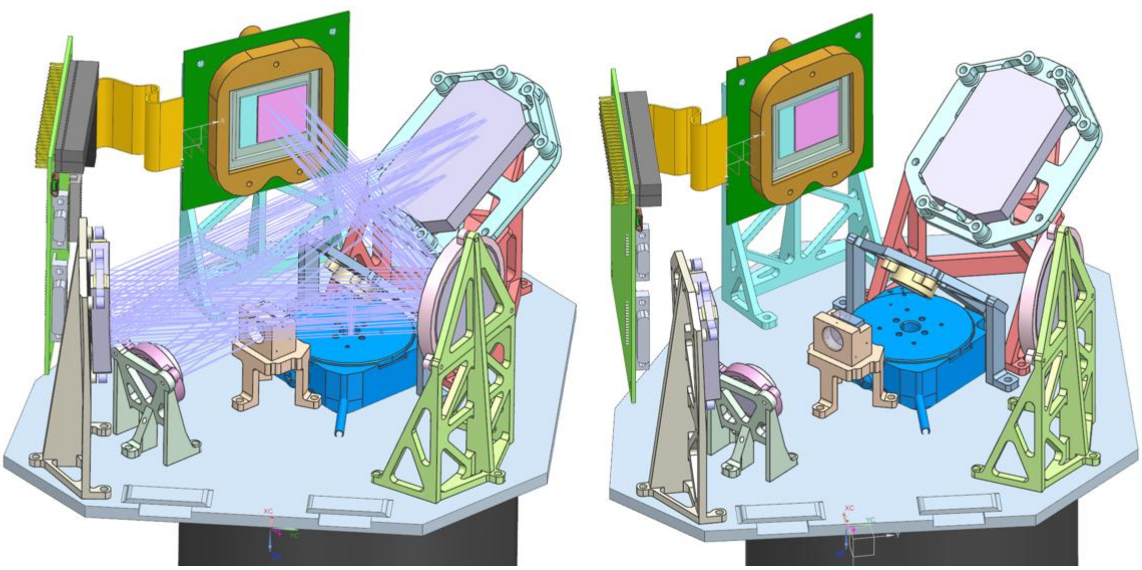

Note. Left has rays entering the instrument through the modulator and ending at the detector.

Mounting Circular and Reflective Optics in STRUVE

Figure 40

Mounting an Optic in an Annular Ring

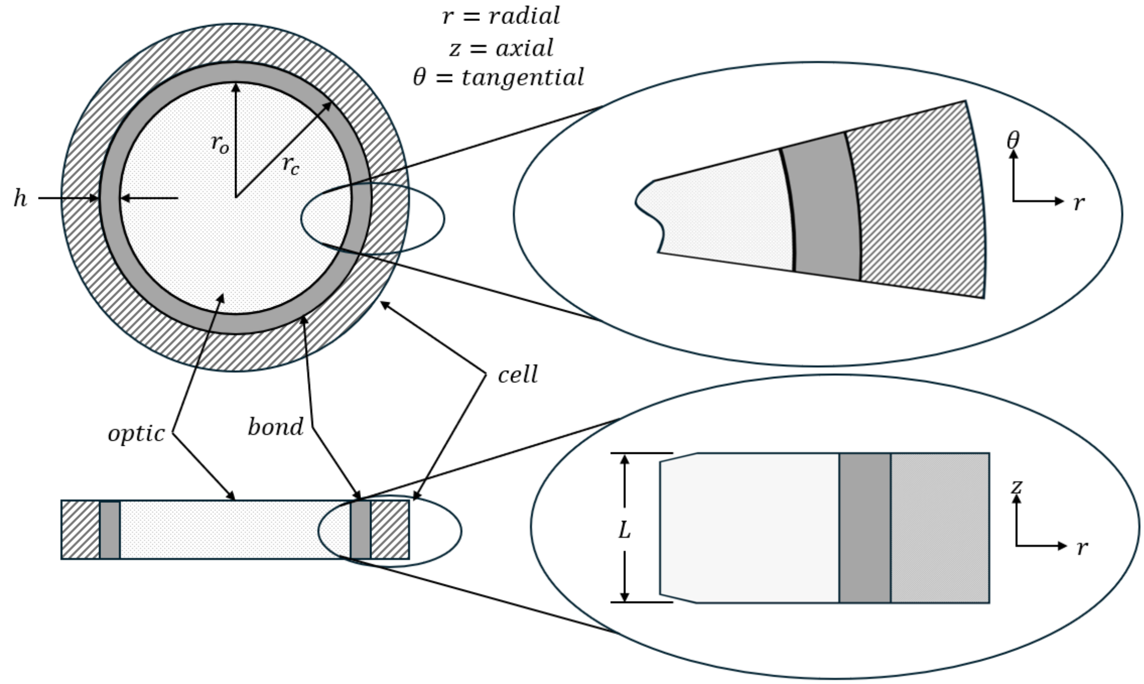

Note. This figure shows a typical annular optic mount. The variables in this diagram are applied in equations 5-11. Figure is adapted from Monti (2007).

The circular optics were mounted in an annular ring in the CAD model for the concept study. The objective is to mount the optic in the cell in a way that makes the system insensitive to temperature changes (athermal). One way to make the system athermal is to match the CTE of the optic substrate material, the cell, and the bonding material. That is difficult to do if the optic is made of a ceramic or glass material, as they have CTEs that are significantly lower than most metals that would be used to mount the optic. The difference in CTE between the optic and mirror cell can be made up for by calculating the bond-line thickness required for athermal mounting of the optic in the cell.

Note, these following calculations only work when the CTE of the optic (α_o) is less than the cell (α_c), and the CTE of the cell is less than the bonding material (α_b) ($\alpha_o < \alpha_c < \alpha_b$) (Herbert, 2006). Figure 40 is a visual representation of an optic fixed in an annular ring. The dimensions pointed out in the figure are used in the following equations to calculate an athermal bondline thickness.

Figure 41.

Comparison of a Heated Assembly

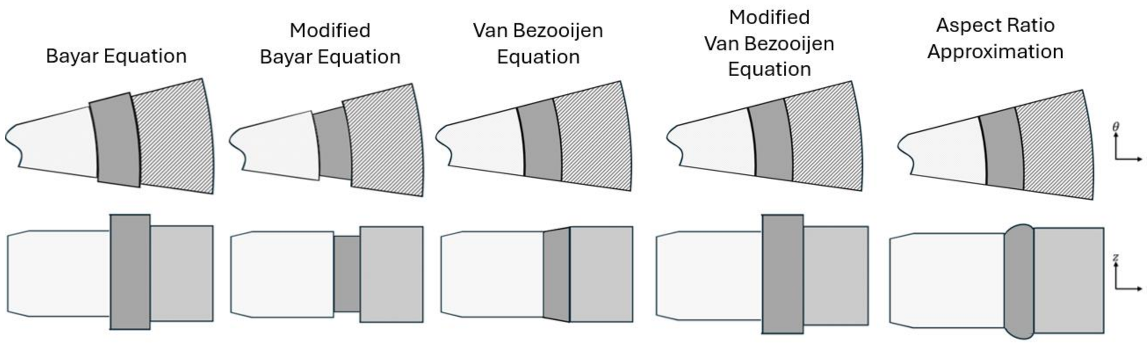

Note. Comparison of a heater assembly for each equation and how it constrains the bond. Figure adapted from Monti (2007)

Multiple equations are available to calculate the bond-line thickness with different levels of accuracy. Figure 41 provides a visual representation, although not to scale, illustrating how each equation applies constraints to the bond line based on its underlying assumptions when subjected to heat (Monti, 2007). All the following equations for calculating an athermal bondline are derived using Hooke's Law for stress, the full derivations can be found in the referenced Monti, 2007 paper. The Bayar equation, while the simplest, lacks accuracy for materials with a Poisson ratio exceeding 0. Considering that most adhesives and epoxy possess a Poisson ratio ranging from 0.4 to 0.5, the Bayar equation is generally not applicable in such scenarios. However, the Modified Bayar equation (Herbert, 2006) enhances accuracy by accounting for the amplification of the CTE as the Poisson ratio increases.

The Bayar equation calculates an athermal bond line by equating the change in bond-line thickness over temperature to the difference in the changes of the optic and the cell radii over the temperature range (Monti, 2007). The change in the bond-line (Δh) is equal to the thickness of the bond-line (h) multiplied by the CTE of the bonding material (α_b) multiplied by the change in temperature (ΔT). The change in the radius of the cell (Δr_c) and optical element Δr_o) are equal to their respective radii multiplied by their respective CTE (α_c, α_o) and the change in temperature. Solving for h results in the Bayar equation (7).

$$\Delta h = \Delta r_c - \Delta r_o \tag{5}$$

$$h\alpha_b \Delta T = (r_o + h)\alpha_c \Delta T - r_o \alpha_o \Delta T \tag{6}$$

$$h = \frac{r_o(\alpha_c - \alpha_o)}{\alpha_b - \alpha_c} \tag{7}$$

In Figure 41, it can be seen the Bayar equation leaves the bond line unconstrained, allowing it to naturally expand in all three axes when heated. Conversely, the Modified Bayar equation (8) constrains the axial and tangent axes of the bond, preventing expansion (or contraction when cooled) in those directions. This constraint is a simplification of what is going on but is used because the optic and optical cell exhibit less expansion compared to the bonding material at the interface, essentially making the bond expand more in the radial direction. That is why the modified Bayar equation calculates for an amplified CTE based on the Poisson ratio (v). However, because the bond is over-constrained, the bond line in the axial and tangent axes results in a thinner bond-line estimate than what may be necessary.

$$h = \frac{r_o(\alpha_c - \alpha_o)}{\left(\frac{1+v}{1-v}\right)\alpha_b - \alpha_c} \tag{8}$$

The Van Bezooijen Equation (9), as illustrated in Figure 41 (Monti, 2007), constrains the bond line at each end with the optic and optical cell, providing a slightly better estimate of the athermal bond-line thickness compared to the Modified Bayar equation. Nevertheless, it may still underestimate the required thickness. The Modified Van Bezooijen Equation (10) relaxes the constraint in the axial direction, resulting in a slightly thicker bond-line estimate, possibly exceeding the requirements for an athermal bond. Both the Van Bezooijen (Herbert, 2006; Monti, 2007) and its modified version can be used to establish a lower and upper bound estimate of the bond-line thickness.

$$h = \frac{r_o(\alpha_c - \alpha_o)}{\alpha_b - \alpha_c + \frac{2v}{1-v}\left(\alpha_b - \frac{\alpha_o + \alpha_c}{2}\right)} \tag{9}$$

$$h = \frac{r_o(\alpha_c - \alpha_o)}{\alpha_b - \alpha_c + \frac{v}{1-v}\left(\alpha_b - \frac{\alpha_o + \alpha_c}{2}\right)} \tag{10}$$

The Aspect Ratio Approximation (Monti, 2007) imposes a constraint on the bond in the tangent axis, similar to the Van Bezooijen variations, while applying a more realistic constraint in the axial direction by allowing it to bulge out, as depicted in Figure 41. This method yields the most accurate estimation of the bond-line thickness necessary for an athermal bond. Figure 42 is a plot by Monti (2007) shows a comparison of how the bondline varies with each of these 5 methods based on a germanium lens with a 2 inch diameter, bond height (axial) of 0.08 inch, an aluminum cell and an RTV bond.

$$\left.\begin{aligned} a &= -\frac{v}{L}\left(\alpha_b - \frac{\alpha_o + \alpha_c}{2}\right) \\ b &= (1-v)(\alpha_b - \alpha_c) + 2v\left(\alpha_b - \frac{\alpha_o + \alpha_c}{2}\right) \\ c &= r_o(1-v)(\alpha_c - \alpha_o) \end{aligned}\right\} \quad h = \frac{-b\sqrt{b^2 - 4ac}}{2a} \tag{11}$$

Figure 42

Monti Bondline Thickness Calculation Example

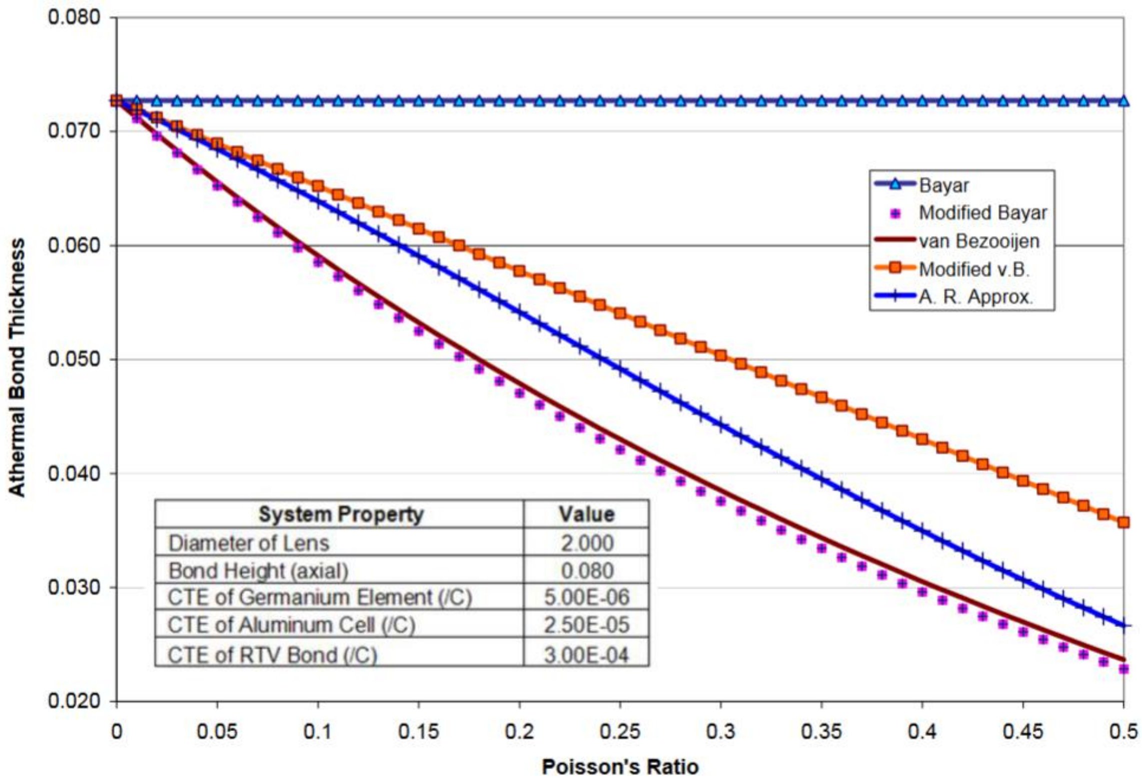

Note. The above plot show shows how the athermal bondline thickness changes with the Poisson Ratio for each of the five equations. The calculations are based on a germanium 2 inch diameter lens, a bond axial height of 0.08 inch, an aluminum cell and an RTV Bond. This example and plot are from Monti (2007).

For the concept study, initial bondline thickness was calculated using the Modified Bayar equation as it was one of the simpler equations that provided a good approximation. By utilizing the modified Bayar equation, the bond-line thickness can be approximated for the circular optics mounted in annular rings. The resulting values can be observed in Table 8. For these calculations, Zerodur is assumed as the optics material, titanium as the mirror cell material, and a common translucent optics grade 2216 epoxy is used. The table provides suggested approximate bond-line thicknesses for mounting the circular optics in annular mounts based on these assumptions. Equations 5 and 6 can be utilized to update these values as assumptions change. However, it's recommended to conduct finite element analysis as it will catch the effects discussed above in the design prior to fabrication and testing.

Another method for mounting reflective optics that can be used involves bonding the back of the optic to the cell (refer to Figure 43). This approach can simplify the design and machining of the mirror cell however depending on the CTE of the materials, it is generally better suited for environments with smaller temperature swings from where

Table 8

STRUVE Circular Optics Annular Mounting Bondline Thickness

Mirror	Dia. (mm)	α_g (°C^{-1})	α_m (°C^{-1})	α_e (°C^{-1})	α_e^* (°C^{-1})	v_e	t_e (mm)
Fold Mirror 1	12.7	0	8.8e-6	81e-6	203e-6	0.43	0.287
Filter	10.1	0	8.8e-6	81e-6	203e-6	0.43	0.229
Off-Axis Parabola	20	0	8.8e-6	81e-6	203e-6	0.43	0.453
Fold Mirror 2	45	0	8.8e-6	81e-6	203e-6	0.43	1.018

Note. The table calculates the bond-line thickness for each of the circular optics in the STRUVE instrument after the telescope. The assumed substrate of the optic is Zerodur, while the assumed mount material is Ti-6Al-4V, and the epoxy is translucent 2216 with a 1:1 mix ratio.

it is cures. The minimum bonded area required are calculated using equation 7.

$$Q_{min} = \frac{W a_g f_s}{J} \tag{12}$$

where Q_{min} is the minimum bond area required, W is the weight of the optic, a_g is the maximum expected acceleration factor, f_s is the factor of safety, and J is the shear or tensile strength of the epoxy (Yoder, 2008).

In Figure 43, the epoxy used is based on the minimum calculated bond area for a 0.5-inch diameter mirror made of Zerodur, with a maximum expected acceleration factor of 100, a factor of safety of 4, and using translucent 2216 epoxy with a shear stress of 2000 in/lb. Something to note again is this is the minimum required bond area.

Figure 43

Fixing Mirrors with Epoxy on the Back

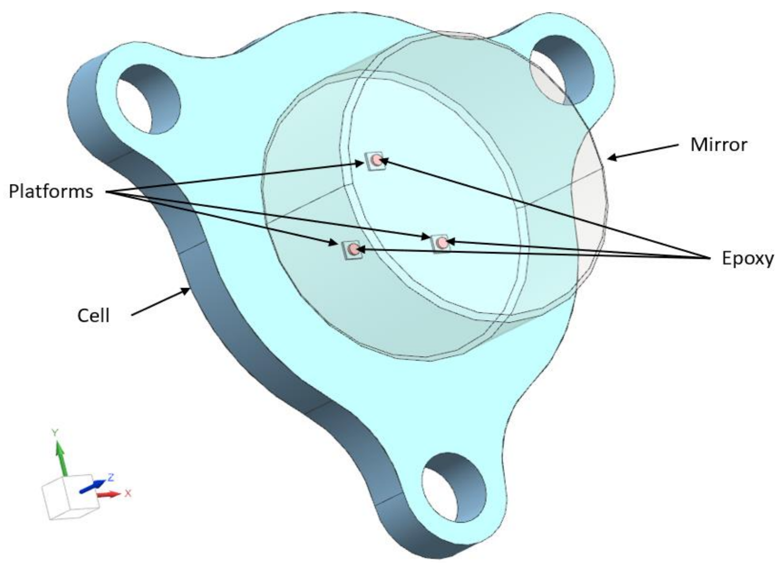

Note. Mounting a flat mirror optic to a mirror cell with bonded points on the back surface of the optic. Platforms are machined into the mirror cell and define the plane the optic sits on.

The bond-line thickness between the glass and metal mount is an important design parameter that should be carefully considered. Typically, the recommended bond-line thickness from the vendor should be followed. It's worth noting that a thin bond-line results in a stiffer bond compared to a thicker bond-line. Depending on the epoxy's Poisson's ratio, the epoxy at the bond can have an effective Young's modulus several hundred times larger than the bulk value, as it is dependent on the ratio of the bond lateral size (diameter) to the bond-line thickness (Yoder, 2008).

To enhance stability and reduce dimensional changes, the calculated total bond area can be divided into three bond areas and placed in an equilateral triangle configuration. This approach helps mitigate the significant CTE differences between the epoxy, glass, and mount. By using one larger bond, the epoxy will have a larger physical change when the temperature changes which can increase the stress on the mirror as well as increase the shear stress at the bonded interface. By creating smaller bonds, the bond areas are reduced resulting in smaller dimension changes in the bond. This results in smaller shear stresses at the bonded joints and increased stability (Yoder, 2008). This works when the CTE of the bonding material is larger than the CTE of the optical element or the mounting material. A balance does have to be made between the distance

Table 9

Minimum Bond Area for Mounting STRUVE Optics from the Back

Optic	W (lbm)	a_G	f_s	$J\ (lb/in^2)$	$Q_{min}\ (in^2)$
Fold Mirror 1	0.0042	100	4	2000	0.00084
Off-Axis Parabola	0.0128	100	4	2000	0.00256
Fold Mirror 2	0.0531	100	4	2000	0.01063

Note. This table shows the values used to calculate the minimum bond area (Q_{min}) and the resulting minimum area required for bonding the optic to the mirror cell.

the bond areas are split up and the size of the bond to ensure that the mounting cell isn't imposing a larger stress than the one larger bonded area.

One method for controlling the bond-line thickness is to mix a small percentage of glass beads per epoxy volume into the epoxy. Glass beads of different diameters can be utilized for this purpose and have a negligible effect on the bond strength (Yoder, 2008).

Mounting Rectangular Optics in STRUVE

The mounting method employed for the cross-disperser and echelle grating differs from that used for the reflective optics. The echelle grating is affixed to the cell using flexures, as depicted in Figure 44. Utilizing flexures to mount the optic allows for flexibility, minimizing stress transmitted from the mount to the optic. When utilizing flexures the design can really be fine-tuned to minimize the imposed stress on the optic and balance it with the rigidity needed for surviving the worst expected environments. This method could also be used to mount circular optics. However, utilizing flexures to mount optics generally increases the mount complexity and can result in increased fabrication costs. For mounting the rectangular optics in the system, the corners of the optic are beveled so that imaginary lines drawn from the center of where the flexures mate to the optic intersect at the middle of the optic. This configuration creates a stationary point, ensuring that the center of the optic remains fixed even with temperature fluctuations. The position of this stationary point can be adjusted by modifying the bevel and the mounting of the flexures (Yoder, 2008).

Figure 44

Mounting Rectangular Optics

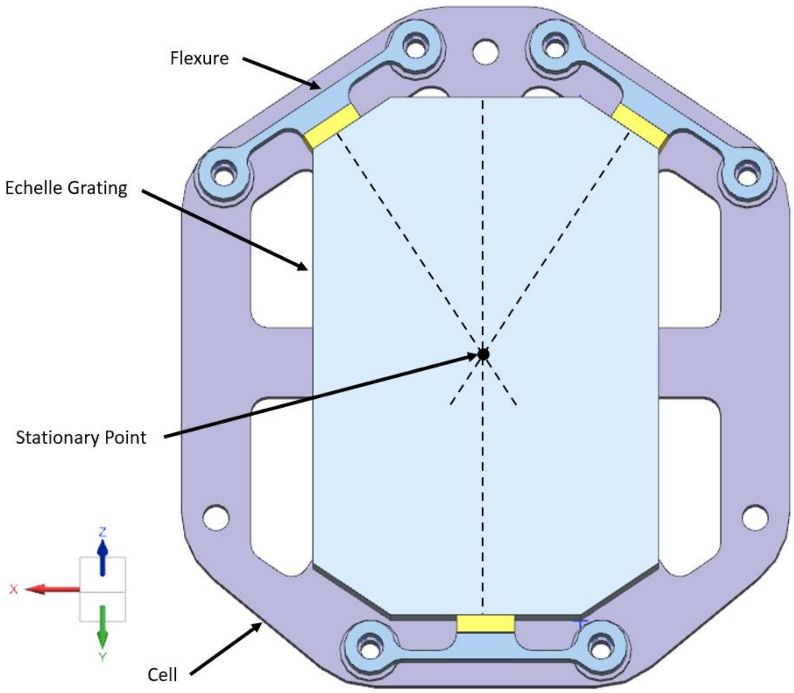

Note. The echelle grating is mounted to the mirror cell using 3 flexures. The flexures are mated to the grating with epoxy. The flexures are fastened to the mirror cell using screws. The corners are beveled so as if a line is drawn at the center of the flexure mating area, the lines will intersect at the center of the optic. This creates a “stationary” point, so if the temperature were to change and create expansions or contractions, the center of the optic will stay in place (Yoder, 2008).

Prism and Filter Mount

The prism and filter are positioned closely together, making it convenient to hold them in the same mount. The light reflects off the first fold mirror into the Wollaston prism, then passes through the filter immediately after the prism. A design challenge arises when the light exits the filter, as it is reflected off the off-axis parabola, folded back, and passes over the filter and prism. Due to the light returning over the mount, the mount must have a low profile to avoid interfering with the light (see Figure 45).

Figure 45

Prism and Filter with Light Ray Trace

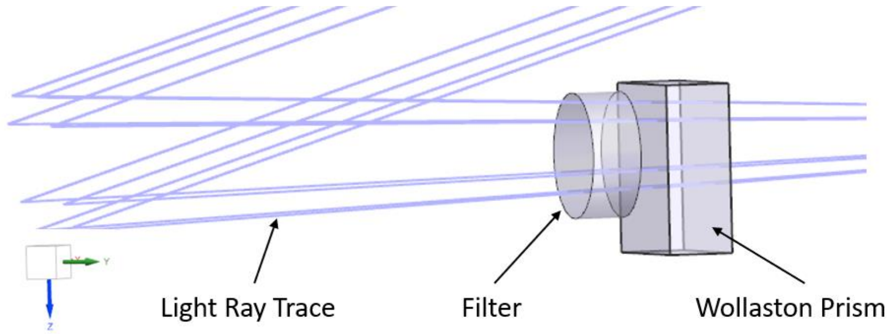

Note. Shows the location of the filter and Wollaston prism regarding each other as well as the beam that comes back over the prism and filter.

The mounting method for the prism is based on a technique found in "Mounting Optics in Optical Instruments" (Yoder, 2008). The prism mount features a reference face where the prism is bonded. The most challenging aspect of this mount is developing a

Figure 46

Mounting Prism and Filter in Mount

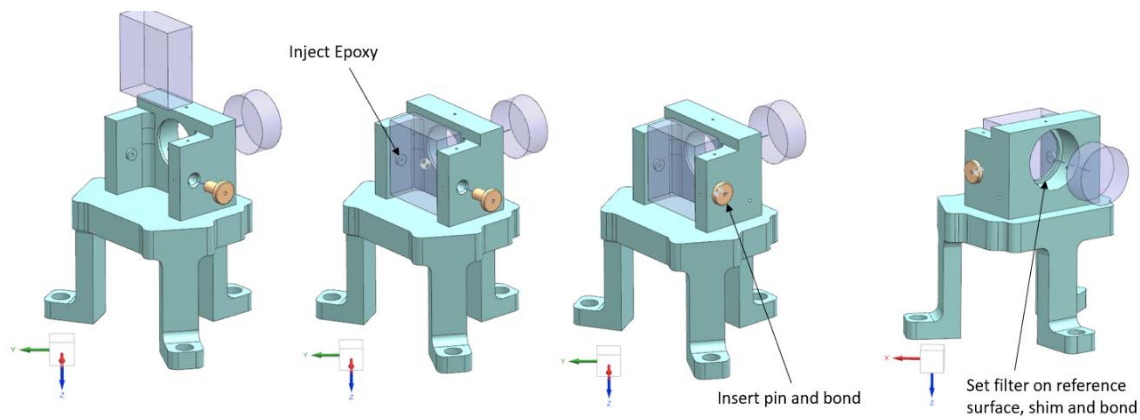

Note. Above shows a quick overview left to right of the assembly process of the Wollaston prism and filter mount. The filter and prism integration to the mount can happen in any order. To install the prism a fixture may be required for alignment. Once aligned epoxy is injected and the prism is bonded to one side. Once cured, the pin is inserted and cured to the prism. The area around the pin is then cured in place via the epoxy injection holes. The filter is inserted into the mount and against the reference face. The filer is then shimmed to be centered. Epoxy is injected through the injection holes in the mount to bond the mirror to the mount.

fixture to hold and align the prism. Once the prism is aligned in the system, bonding it to the mount ensures that it retains its alignment. Figure 46 illustrates the assembly process of the prism and filter into the mount. After aligning the prism, epoxy is injected from the left side of the mount to bond the prism to the mount. A pin is then inserted from the right side and bonded to the prism. Once the epoxy has cured, the pin is bonded to the mount through epoxy ejection holes. The pin allows more room for the optic to be aligned inside the mount and then provides a second bonding area.

Something to note about the mounting of the Wollaston Prism is the prism itself is made up of two MgF_2 crystals bonded together with crossed axis. The two axes have different CTEs which have a difference of about 5 x 10^6 per degree celsius. This different CTE between the two can create stresses and cause the bond to sheer. This was not taken into account at this point in the design. A way to mitigate this is through analysis to ensure the optic is uniform in temperature or the temperature difference across the prism is small enough to where the shear stress's are minimal. A change to the mount design may entail bonding from one end to ensure the optic is held by one of the crystals to ensure there are no extra forces pulling the crystals apart. Designing flexures into the mount may also be an option to ensure minimal stresses are transferred to the prism.

The filter is inserted into the mount against the reference surface in the ring. It is then shimmed to the center, and epoxy is injected through holes around the mount to bond the filter. The bond areas and bond thicknesses are determined using the methods discussed in previous sections.

Instrument Shroud

An aluminum shroud envelops the optics on the optics bench, serving multiple purposes. Firstly, it prevents stray light from entering the system. Secondly, it reduces the likelihood of contamination from the spacecraft reaching the interior where the optics are housed. Thirdly, it enhances the stability of the optics system by attenuating external radiative inputs. The shroud interfaces with the optics bench through a set of flexures to alleviate stress caused by the mismatch in CTE between the titanium optics bench and the aluminum shroud (refer to Figure 47).

Figure 47

STRUVE Shroud Mounting Point

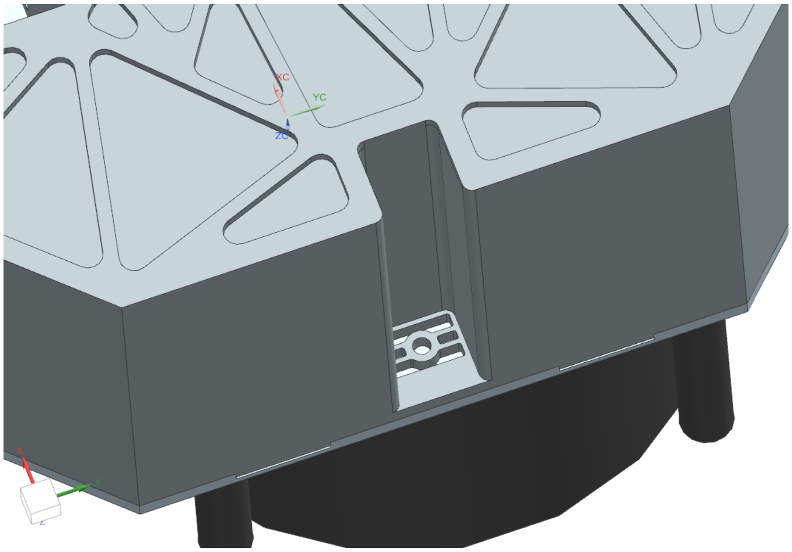

Note. The flexures reduce any temperature-imposed stresses due to the material mismatch between the aluminum shroud and titanium optics bench.

To illustrate the temperature instability dampening effect, a simple model is constructed. The model consists of three plates: the boundary plate, the shield, and the sample plate. The boundary plate is controlled to be at 0°C for 1 hour before being

Figure 48

Basic Model Used to Demonstrate Effectiveness of Shield

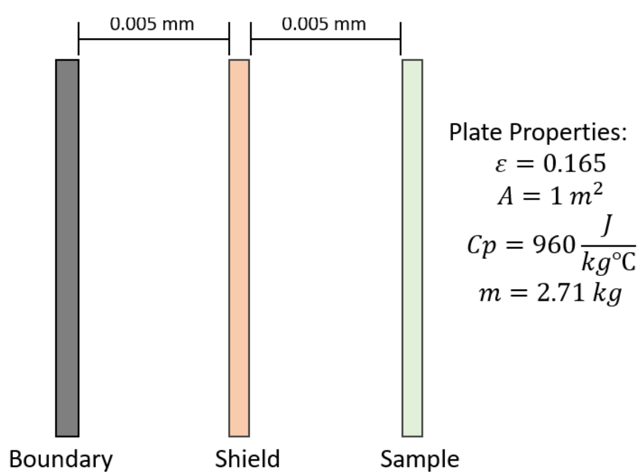

instantaneously switched to 30°C for an hour. The shield and sample plate start at an initial temperature of 20°C. Each plate has an area of 1 m^2, an emissivity of 0.165, specific heat of 960 J/kg/°C, a mass of 2.71 kg, and are separated by 0.005 mm.

The heat transfer (Q) between the two plates is calculated using the grey body radiative heat transfer equation, considering the Stefan-Boltzmann constant (σ), temperatures of the plates (T), emissivity (ε), radiating area (A), and view-factor (F_{1-2}) between the two areas. To determine the temperature change over time (dT/dt), the equation for rate of temperature change is used, considering the mass (m) and specific heat (Cp) of the material. Combining these equations and creating a node network allows for the calculation of the change over time.

$$Q = \frac{\sigma(T_1^4 - T_2^4)}{\frac{1-\varepsilon_1}{\varepsilon_1 A_1} + \frac{1}{A_1 F_{1-2}} + \frac{1-\varepsilon_2}{\varepsilon_2 A_2}} \tag{13}$$

$$mCp\frac{dT}{dt} = Q \tag{14}$$

The baseline case examines the sample response without the shield between it and the boundary node (see Figure 48). With the boundary node temperature change, the sample plate experiences a temperature change of 5.7°C (see Figure 47). This change could be dampened by increasing the thermal mass or reducing heat transfer. One way to reduce heat transfer is with MLI, although MLI can introduce contamination if not properly cleaned. Alternatively, adding an aluminum shroud, while heavier and potentially more costly, is a cleaner option than MLI. In the second scenario the shield is add in to the analysis (see Figure 48), the effective emissivity isn't reduced as much as

Figure 49

Temperature Response of Sample to Environment Chambe with no Shield

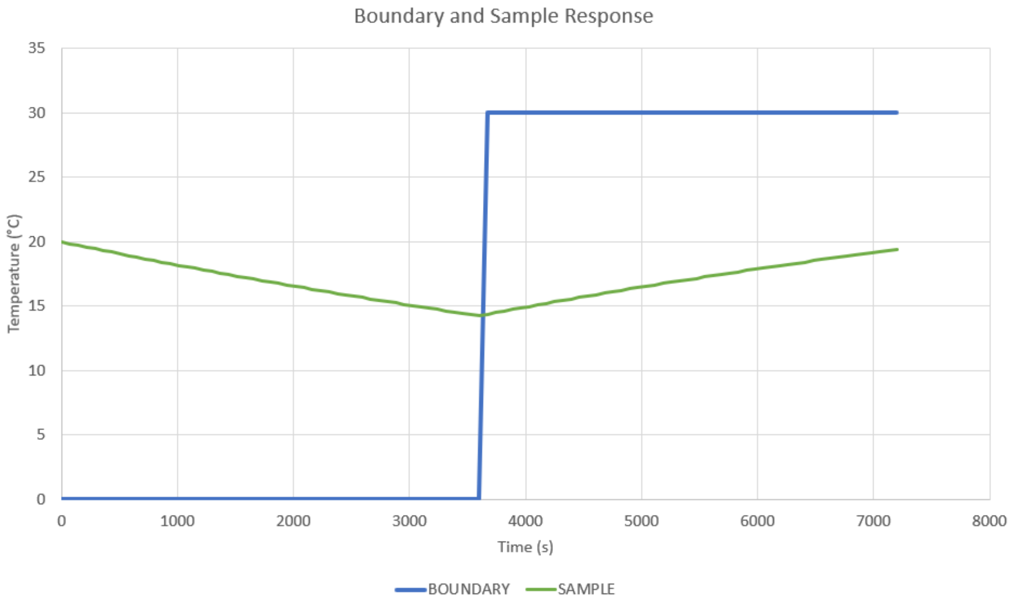

Figure 50

Temperature Response of Sample to Environment Chambe with Shield

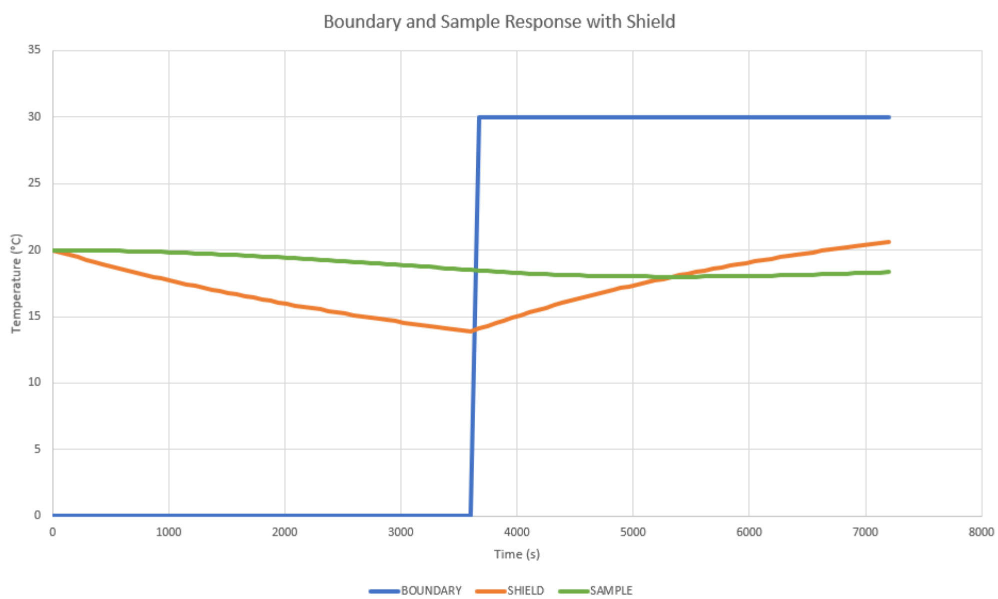

with MLI, but mass is added to the system, effectively dampening the response. As shown in Figure 50, the sample plate experiences a temperature change of 2°C, resulting in a reduction of 3.7°C in temperature change. Additionally, the sample plate response is slightly delayed.

STRUVE Orbital Environment

To achieve a comprehensive grasp of the spacecraft's thermal environment, a simple thermal model is formulated in Thermal Desktop (*Thermal Desktop | C&R Technologies*, n.d.) with a thermal mass of 0 J/K and situated within a typical orbit. By setting the thermal masses of the surfaces to 0 J/K, the obtained temperature results for the spacecraft precisely reflect the ambient sink temperature. Two prevalent orbital configurations are specifically analyzed: the favored sun-synchronous orbit with a 6AM

Figure 51

Simplified Orbit Environment Study Model Overview

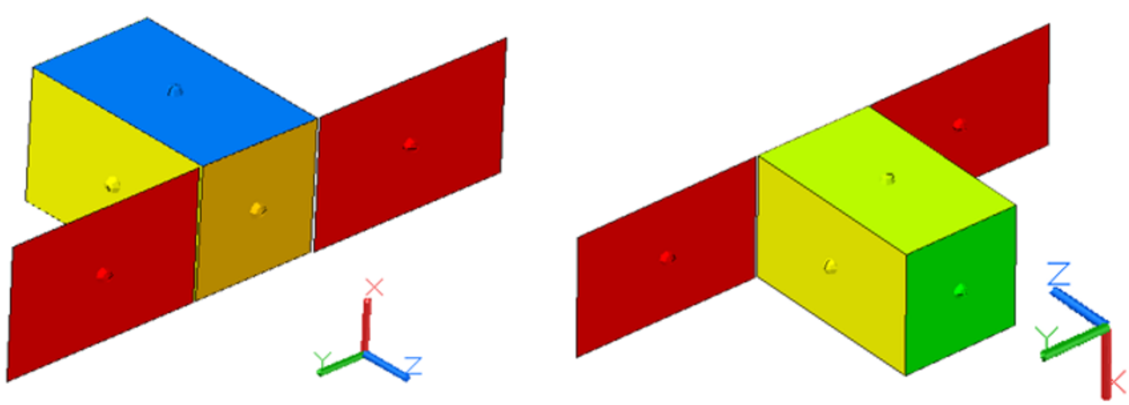

Note. This figure displays the simple thermal desktop model used to understand the thermal environment better. Each panel is made up of a single node and not conductively connected with only the external surfaces radiating. The temperature results will represent the equivalent external radiative heat sink temperature of that panel.

ascending node and a frequently assigned ISS orbit with an inclination of 51.6º.

In discussions regarding thermal environments in LEO, the beta angle holds significant importance in delineating the orbit's attributes. It denotes the angle between the Solar vector and the spacecraft's orbital plane (Gilmore, 2002). A beta angle of 90º indicates that the solar vector is perpendicular to the spacecraft's orbital plane, resulting in orbits characterized by consistent solar loading. Conversely, beta angles of 0º correspond to orbits experiencing the maximum duration of eclipse (the actual duration depending on the orbit's altitude). It's crucial to recognize that the beta angle is dynamic, varying throughout the year based on Solar inclination. The beta angle (β) can be calculated using the following equation where δ_s is the declination of the sun, RI is the orbit inclination, Ω is the right ascension of the ascending node, and Ω_s is the right ascension of the sun (Gilmore, 2002).

$$\beta = \sin^{-1}(\cos\delta_s \sin(RI)\sin(\Omega - \Omega_s) + \sin\delta_s \cos RI \qquad (15)$$

In a sun-synchronous orbit, the orbit proceeds eastward at the same rate as the sun (0.985647 deg/day)(Gilmore, 2002). Figure 52 depicts the dynamic fluctuations in the beta angle for a sun-synchronous orbit, highlighting its correlation with Solar inclination. The plot includes an eclipse line, delineating the beta angle at which the spacecraft encounters orbital eclipses. Orbital eclipses for the spacecraft occur when the beta angle falls below this line. Calculations for the eclipse line are specifically derived from an orbit positioned at an altitude of 550 km. It's important to emphasize that, despite being in

Figure 52

Sun-Synchronous Orbit Beta Angle Variation, 550km Altitude

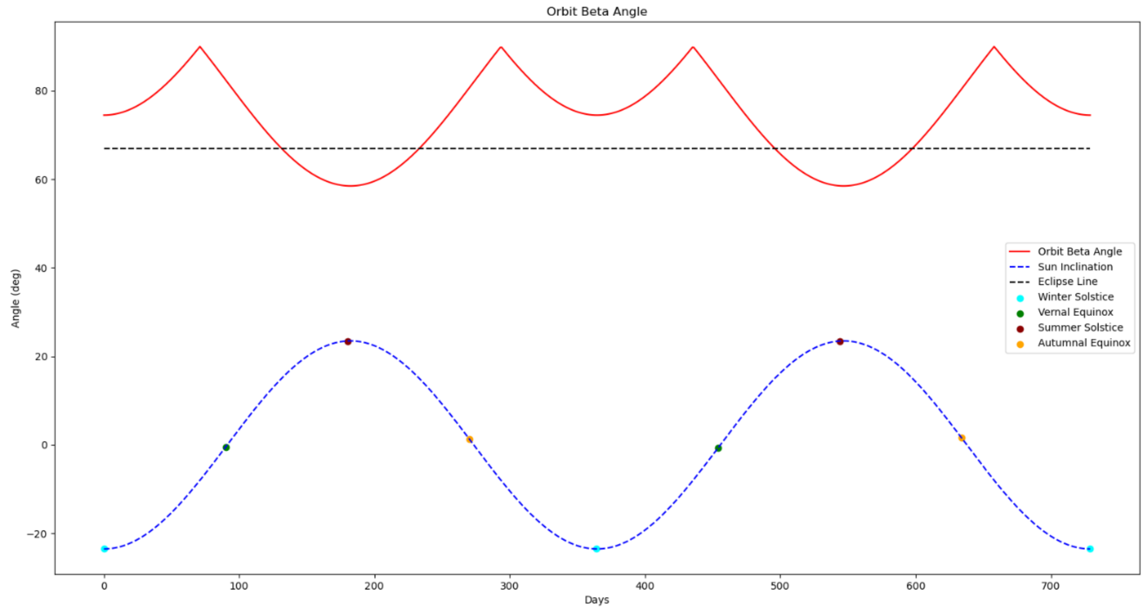

Note. The plot shows how a sun-synchronous orbit with an inclination of 98° varies throughout a 2-year period based on the Sun's inclination. The black dashed line indicates when the orbit beta angle drops below it the spacecraft would start to experience orbits with eclipses.

a sun-synchronous orbit, the spacecraft experiences orbital eclipses at different times throughout the year, with up to 23% of an orbit spent in an eclipse.

The beta angle where the eclipse starts (β^*) can be calculated using equation 6, where cap Ris is the Earth's radius and h is the orbit altitude. Equation 7 can be used to determine the fraction of the orbit that the spacecraft spends in eclipse. Something to note is that the equations assume a circular orbit and the Earth's shadow is cylindrical (Gilmore, 2002).

$$\beta^* = \sin^{-1}\left[\frac{R}{R+h}\right], \quad 0° \leq \beta \leq 90° \tag{16}$$

$$f_E = \frac{1}{180°}\cos^{-1}\left[\frac{(h^2+2Rh)^{\frac{1}{2}}}{(R+h)\cos\beta}\right], \qquad if|\beta| < \beta * \tag{17}$$

$$0 \qquad if\ |\beta| \geq \beta^*$$

In an ISS like orbit, a spacecraft would spend the majority of its life with eclipses in the orbit. This could prove challenging when the instrument has a thermal stability requirement. Assuming the spacecraft is orbiting at an altitude of 400 km like the International Space Station (ISS), up to 38% of an orbit can be in the shadow of the

Figure 53

ISS Like Orbit Beta Angle Variation

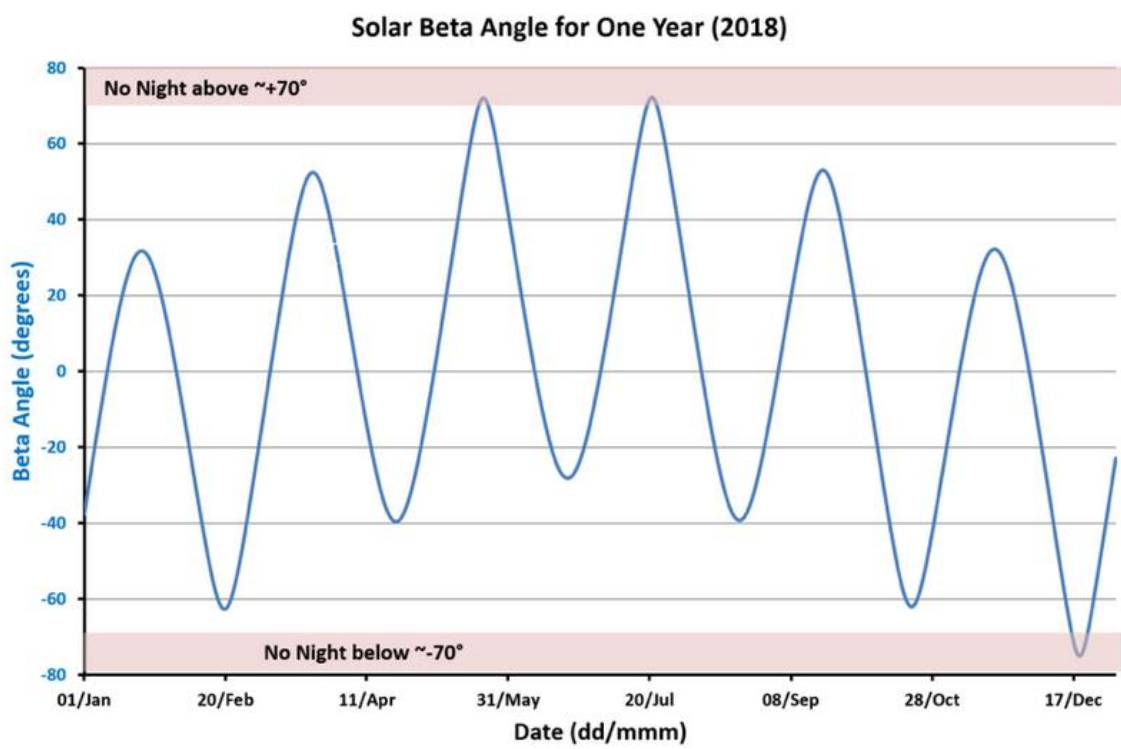

Note. This figure shows how the beta angle changed for the ISS through 2018. The figure is from: https://ams02.space/operations/thermal-operation

Earth. The longest eclipses would occur when the beta angle is equal to 0°. There are brief intervals that usually last up to a week when the beta angle is greater than 70° or less than -70° where the spacecraft will not have to contend with the Earth's shadow in an orbit (Figure 53).

Using the simple Thermal Desktop model, environmental sink temperatures were analyzed for orbits by assessing the maximum and minimum beta angles for both sun-synchronous and ISS orbits. In the case of sun-synchronous orbits, our investigation centered on instances when the beta angle reached its maximum and minimum values. Conversely, for ISS orbits, we examined sink temperatures during orbits with the beta angle at its maximum and at 0º, representing scenarios with the minimum and maximum eclipse times, respectively.

Figure 54

View From Sun of Spacecraft Orbit, Sun-Sync Orbit β = 90°

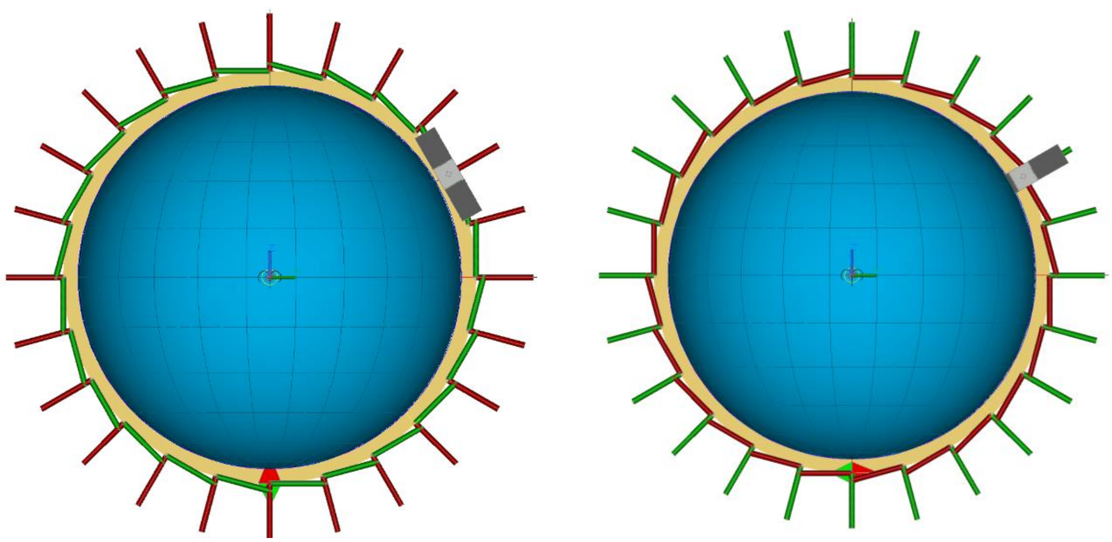

Note. View from the Sun of the spacecraft orbiting Earth in Thermal Desktop with a beta angle of 90°. Left, the +X axis is pointed towards space. Right, the +Y axis is pointed towards space.

Figure 54 depicts a representation of the spacecraft orbiting Earth in Thermal Desktop, positioned in an orbit with a beta angle of 90°. In this configuration, the +Z coordinate of the spacecraft is directed toward the sun, optimizing the utilization of the solar panels and representing the direction the telescope faces to observe the sun. Figure 53 illustrates the environmental sink results for each panel of the spacecraft based on the orbit and orientation of the spacecraft. This information is crucial as it provides insights into the sink temperatures available for each panel of the spacecraft, aiding in the understanding of thermal management strategies.

In Figure 53, the plot displays the temperature results of the spacecraft completing two orbits around Earth. The +X panel offers the coldest environmental heat sink of

Figure 55

Sun-Sync Orbit β = 90º -X Panel Pointed Nadir

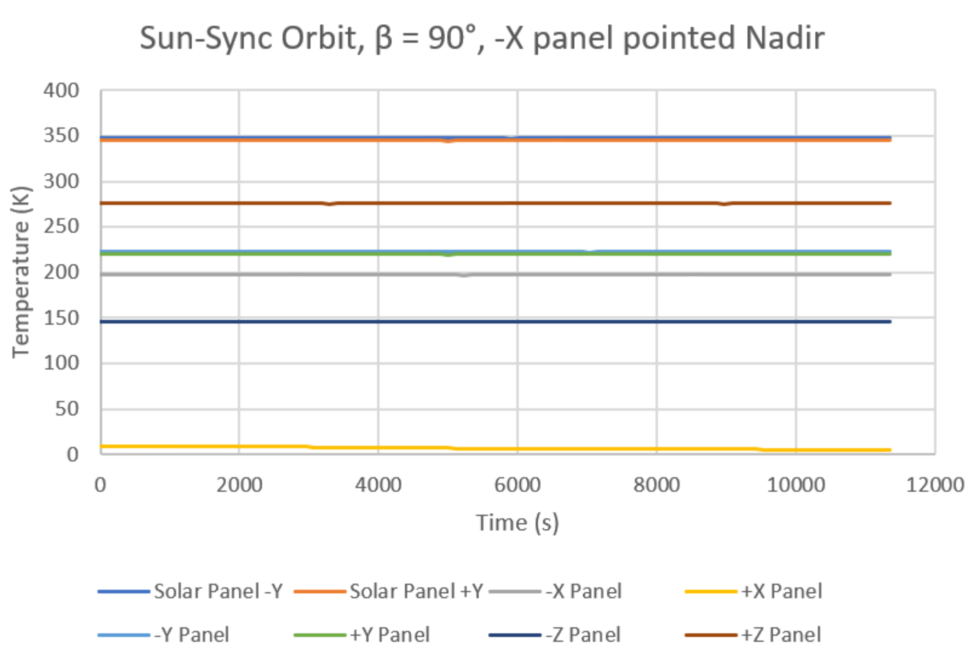

Note. The plot shows the temperature results over two orbital periods at a beta angle of 90°. The -X panel is pointed

Figure 56

Sun-Sync Orbit β = 90º -Y Panel Pointed Nadir

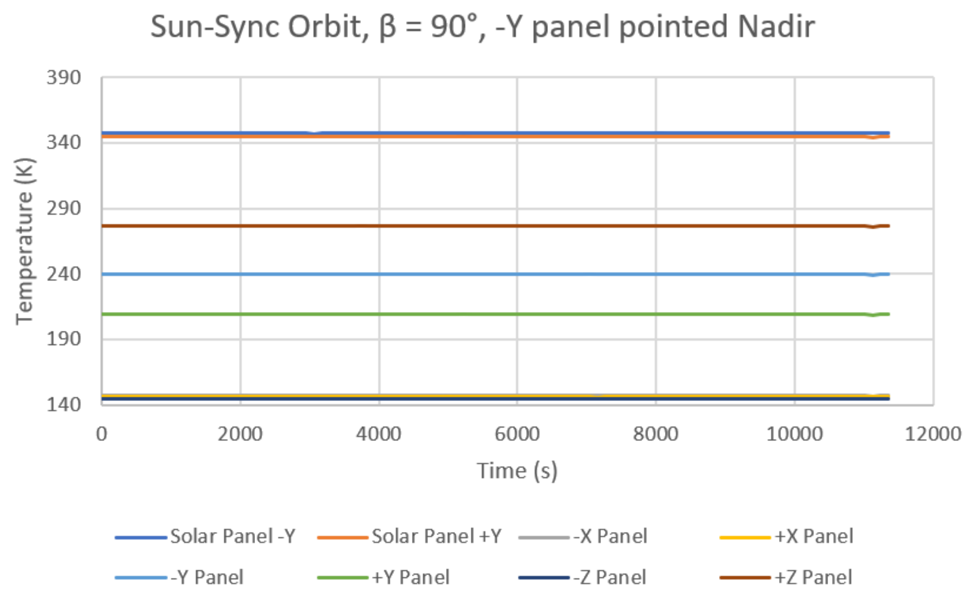

Note. The plot shows the temperature results over two orbital periods at a beta angle of 90°. The -Y panel is pointed

about 4K for the spacecraft since it has an unobstructed view of space. The sun-synchronous orbit ensures a stable thermal environment for the spacecraft. The primary thermal instabilities are anticipated to arise from temperature disparities of Earth and variations in albedo as the spacecraft traverses its orbit around Earth.

If the spacecraft's orientation is rotated 90 degrees about the Z-axis so that the -Y panel is directed Nadir, the panel facing space becomes the +Y panel. In this orientation, the +Y panel does not experience the same cold thermal environment as the +X panel did. This difference is attributed to thermal back loading on the +Y panel from the deployable radiator positioned 90 degrees off from it. Consequently, the +Y panel has a thermal sink of about 209K, whereas the +X panel has a thermal sink of approximately 147K (Figure 54). In this new orientation, the +X panel now has a view of both Earth and space, with Earth occupying roughly 26% of the panel's view and space comprising the

Figure 57

View Factor Planar Element Above Sphere

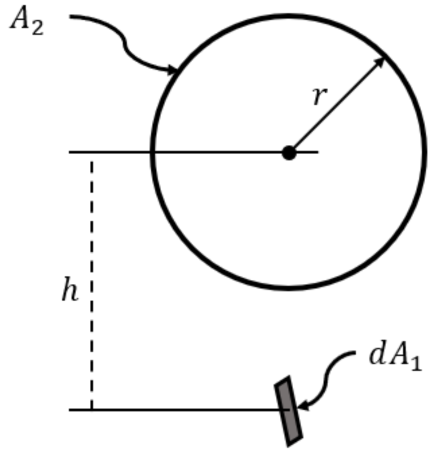

Note. Planar element above a sphere, related to calculating view-factors in equation 7.

Figure from "Radiative Heat Transfer" (Modest, 2013).

remaining 74%. View-factors can be calculated in a variety of ways, the easiest way is to use a view-factor catalogue. Calculating the view-factor (F) for the side of the CubeSat in this case can be simplified down to a differential planar element orbiting a sphere as seen in Figure 55 and using equation 13 (Modest, 2013).

$$F_{d1-2} = \frac{1}{\pi}\left[\tan^{-1}\frac{1}{\sqrt{(h/r)^2 - 1}} - \frac{\sqrt{(h/r)^2 - 1}}{(h/r)^2}\right] \qquad (18)$$

Figure 58

View From Sun of Spacecraft, Sun-Sync Orbit β = 58.5°

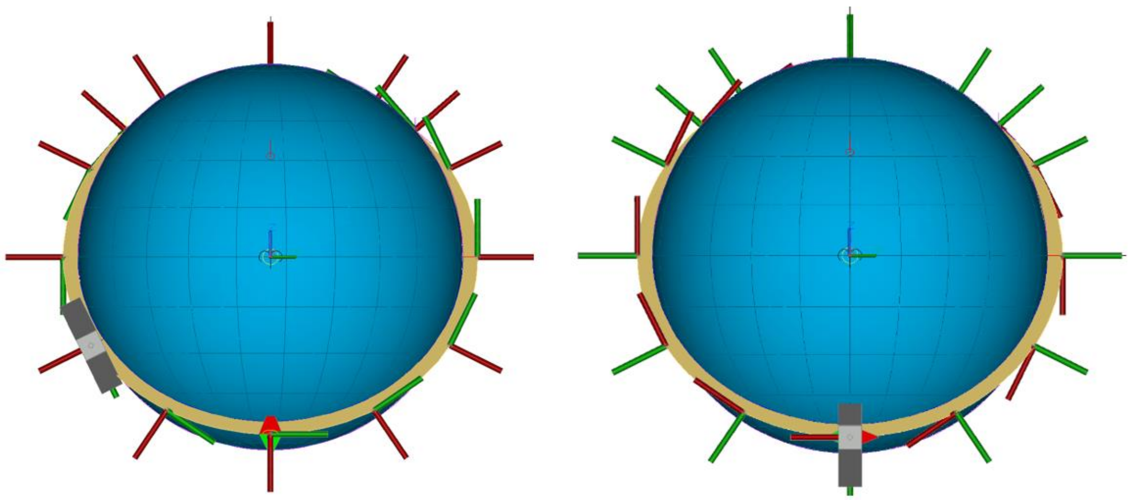

Note. View from the Sun of the spacecraft orbiting Earth in Thermal Desktop with a beta angle of 58.5°. Left, the +X axis is pointed towards space. Right, the +Y axis is pointed towards space.

In a sun-synchronous orbit when the beta angle is at its minimum (58.5 degrees), the spacecraft will be eclipsed by Earth (Figure 56). With the -X panel pointed nadir, the +X panel faces space for most of the orbit. However, at two points in the orbit, Earth comes into view of the panel, introducing disturbances in the thermal environment (Figure 56 & Figure 57). By rotating the spacecraft 90 degrees about the Z-axis so that the -Y panel is directed nadir, the +X panel encounters a stable thermal environment with an environmental heat sink at approximately 192K (Figure 58).

Figure 59

Sun-Sync Orbit β = 58.5° -X Panel Pointed Nadir

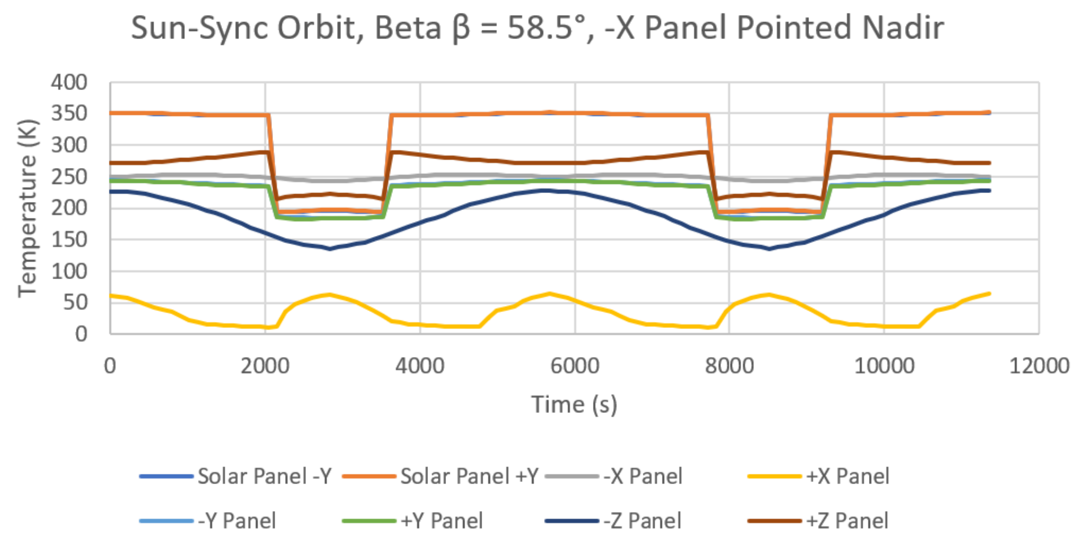

Note. Plot shows the temperature results over two orbital periods at a beta angle 58.5°. The -X panel is pointed Nadir.

Figure 60

Sun-Sync Orbit β = 58.5° -Y Panel Pointed Nadir

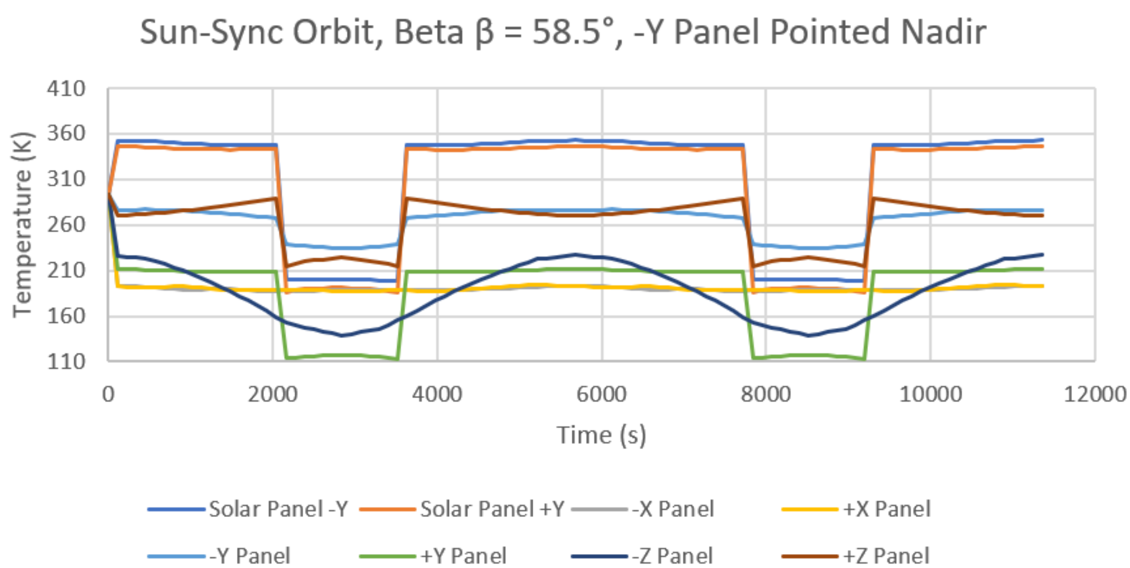

Note. Plot shows the temperature results over two orbital periods at a beta angle 58.5°. The -Y panel is pointed Nadir.

Figure 61

View From Sun of Spacecraft, ISS Orbit β = 0º

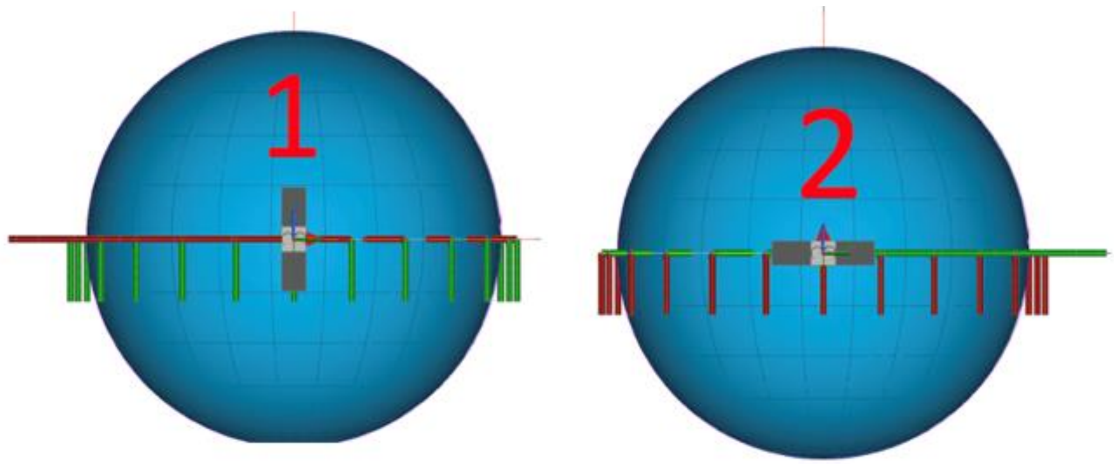

Note. Left, option 1 positions the +X and -X axis aligned with the orbital vectors. Right, option 2 positions the +Y and -Y axis along the orbital vectors.

In the ISS orbit with the longest eclipse duration occurring when the beta angle is 0, two orientations were explored. Option 1 positioned the +X and -X panels aligned with the orbital vectors, while option 2 involved rotating the spacecraft 90 degrees about the Z-axis, placing the +Y and -Y panels along the orbital vectors.

Option 1 (Figure 60) resulted in a significantly less stable thermal environment, with all panels experiencing considerable temperature fluctuations. The X panels exhibited large temperature swings as they alternated between facing open space and Earth at different points in the orbit. The Y panels encountered temperature variations due to thermal backloading and changes in solar panel orientation.

Figure 62

ISS Orbit β = 0º, Option 1

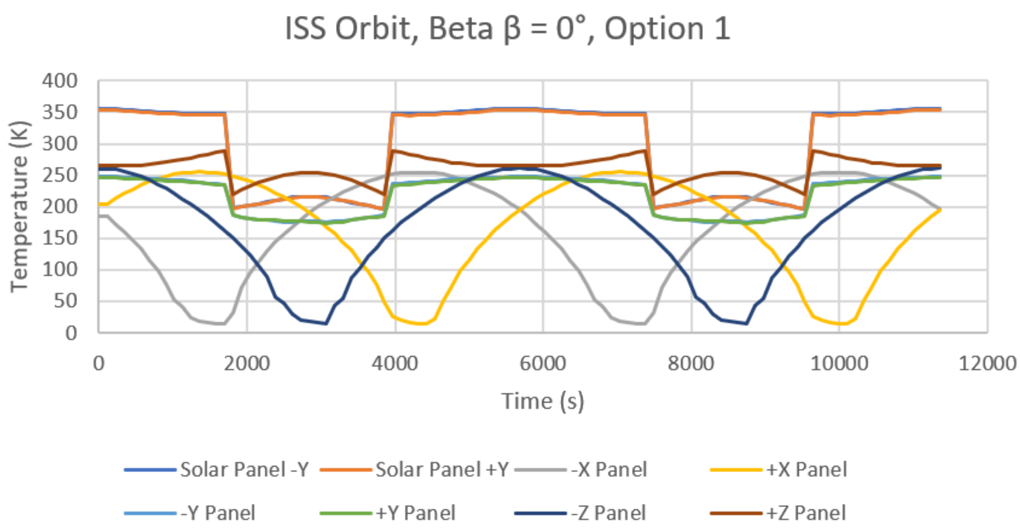

Note. Plot shows the temperature results over two orbital periods at a beta angle 0°. The X panels are pointed along the orbital vector.

Figure 63

ISS Orbit β = 0º, Option 2

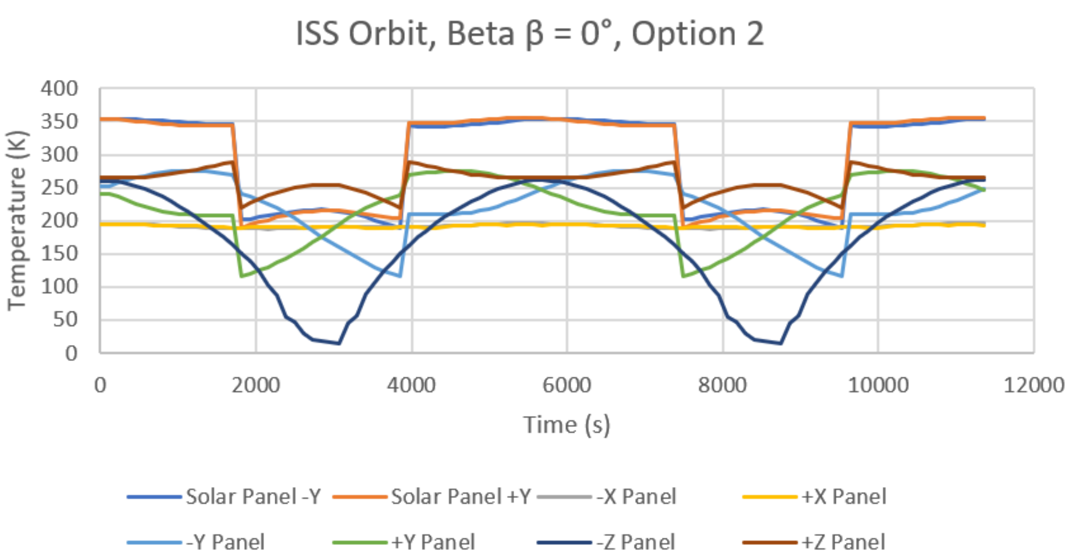

Note. Plot shows the temperature results over two orbital periods at a beta angle 0°. The X panels are pointed along the orbital vector.

In contrast, option 2 (Figure 61) provided a stable thermal environment for both the +X and -X panels. In this configuration, the X panels experienced minimal changes in their field of view throughout the orbit, with approximately 28% of their view consisting of Earth and 72% space. Additionally, the X panels were unaffected by backloading from the solar panels, which impacted the Y panels in this orientation.

Based on this analysis, it is recommended to designate the +X panel as the radiator. For the sun-synchronous orbit, either orientation during observation modes would offer a stable thermal sink. The primary distinction between the two orientations lies in the environmental heat sink temperature for the radiator. In all orbital cases examined, a stable thermal environment was achievable. The table below outlines the average environmental sink temperature for each stable orbit identified. When talking to future spacecraft vendors this analysis provides insight into why the radiator should not be able to view the solar panel. Future analysis needs to focus on understanding in detail how the spacecraft needs to operate in orbit. Operational considerations such as how long the payload needs a constant alignment with the sun without any rotations could affect the thermal stability. A more detailed spacecraft model with the payload model will

Table 10

Orbit and Average Stable Temperatures For +X Panel

Orbit	Average Environmental Sink Temperature (K)
Sun-Syn, $\beta = 90°$	4 – 147
Sun-Sync, $\beta = 58.5°$	192
ISS, $\beta = 0°$	194

Note. Tale of average environmental sink temperature for the +X panel from the cases with a stable thermal environment.

provide insight into how more realistic operation conditions do affect the instrument.

To verify the heat sink temperature is cold enough to dissipate excess heat sufficiently, it can be assessed by performing first-order radiative heat transfer calculations. The equation below is used to calculate the radiative heat transfer (Q_{rad}) from a grey body to a black body. Assuming a radiator area (A) of 0.06 m^2 (full side of

$$Q_{rad} = A\varepsilon\sigma(T_1^4 - T_2^4)$$

$$Stefan - Boltzmann\ Constant \qquad \sigma = 5.67 * 10^{-8}\ W/m^2K^4 \tag{19}$$

12U CubeSat) with an emissivity of 0.88 and a working temperature average temperature of -10 °C, the radiator is capable of dissipating 10 W to a sink temperature of 195 K. The expected heat generation of the detector is expected to be less than 1 W, so a heat dissipation capability of 10 W is plenty capability wise giving room to possibly shrink the radiator.

This analysis shows that the thermal environment is very dynamic and can vary greatly depending on the spacecraft orientation or the panel that is being considered. It was shown that in a sun-synchronous orbit a stable thermal environment can be achieved throughout the majority of a year with a constant heliocentric orientation. When the spacecraft begins to experience eclipses, the spacecraft does not have a stable thermal environment. However, with the spacecraft in a heliocentric orientation and with he radiator panel oriented as described in the analysis above, a stable heat sink for the instrument radiator can be found. By isolating the instrument radiator and the instrument from the rest of the spacecraft the thermal fluctuations from the environment can be mitigated.

Detailed Thermal Model

A detailed thermal model of the instrument is constructed based on the CAD model, as depicted in Figure 62. This model is developed using Thermal Desktop, a robust software tool renowned for its capability in thermal analysis and system design. By leveraging Thermal Desktop, engineers can simulate heat transfer within intricate structures across diverse thermal environments, including space conditions.

The primary objective of this thermal model is to evaluate the thermal performance of the conceptual CAD model. It serves as a crucial tool to identify areas for improvement in the STRUVE thermal system development. Moreover, the model aids in establishing spacecraft thermal requirements tailored to meet the payload's needs. In this regard, while the instrument is modeled in more detail, the spacecraft and avionics are represented at a far less detailed level, functioning primarily as boundary nodes. This

Figure 64

Overview of Detailed Thermal Model for STRUVE

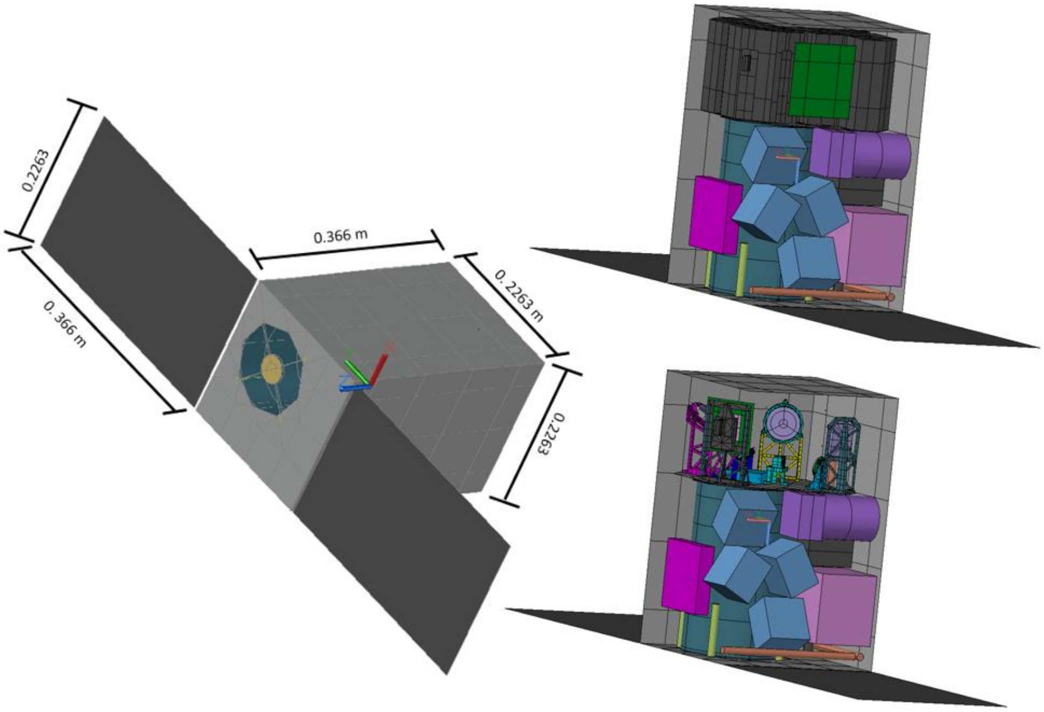

Note. Detailed thermal model, left is the external view with the cut out for the telescope, right is the view inside of the spacecraft with two external panels hidden. Right bottom the shroud is hidden so the optics assembly can be seen.

approach allows for a comprehensive understanding of the instrument’s thermal environment required to fulfill the instrument's scientific objectives, guiding future efforts in spacecraft design and thermal system optimization.

Model Configuration and Property Assignments

Figure 63 provides a side-by-side comparison between the thermal model and the CAD model. While the thermal model is less detailed than the CAD model, it effectively captures the heat flow dynamics from the optics bench to the optics, enabling the analysis of temperature gradients across the mounts. Conductors and contactors are strategically employed in the model to establish conductive connections between each mesh. The contactor and conductor details in the model can be found in Appendix A. The conductance values provided in these tables are based on a generic epoxy with a conductivity of 1 W/mK, supplemented by screw joint conductance tables sourced from the "Spacecraft Thermal Control Handbook" (Gilmore, 2002).

Figure 65

STRUVE Optics Assembly Thermal Model vs. CAD Model

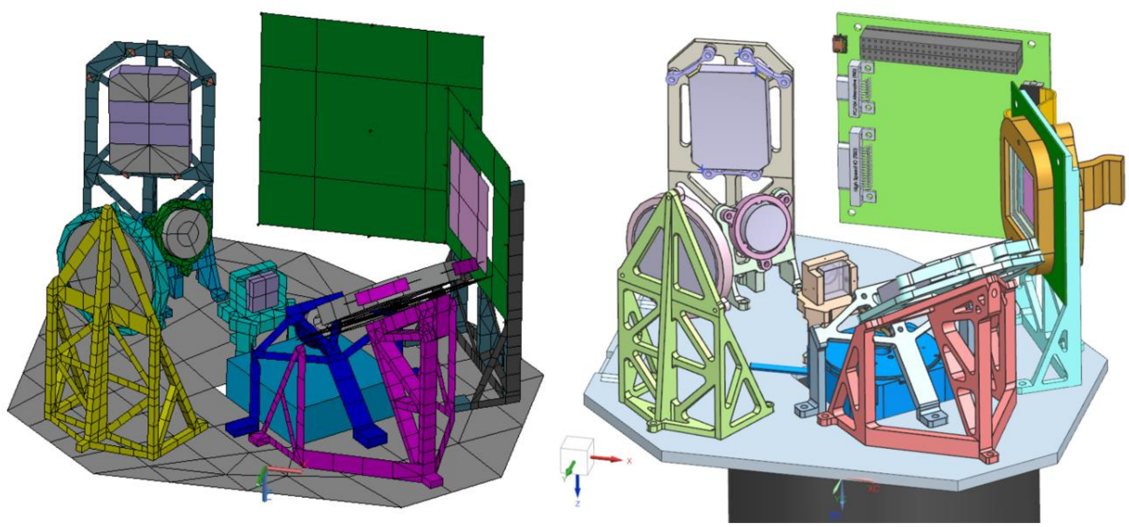

Table 11

Thermal Model vs. CAD Model Mass Comparison

Component	CAD Model Mass (kg)	Thermal Model Mass (kg)
Thermal Strap	0.23	0.23
Detector Mount	0.11	0.11
Payload Shroud	0.67	0.67
Telescope	1.67	1.69
1st Fold Mirror Assem	0.05	0.05
Optics Bench	1.27	1.27
Prism & Lens Assem	0.06	0.06
Echelle Assem	0.31	0.31
2nd Fold Mirror Assem	0.13	0.13
Cross-Disperser Assem	0.12	0.12
Total	4.62	4.64

These values serve as an initial reference point for the thermal analysis conducted during the concept study. However, further analysis should explore variations in these conductances to assess the system's behavior under different scenarios. These values serve as an initial reference point for the thermal analysis conducted during the concept study.

Figure 66

Model Thermophysical Property Assignment

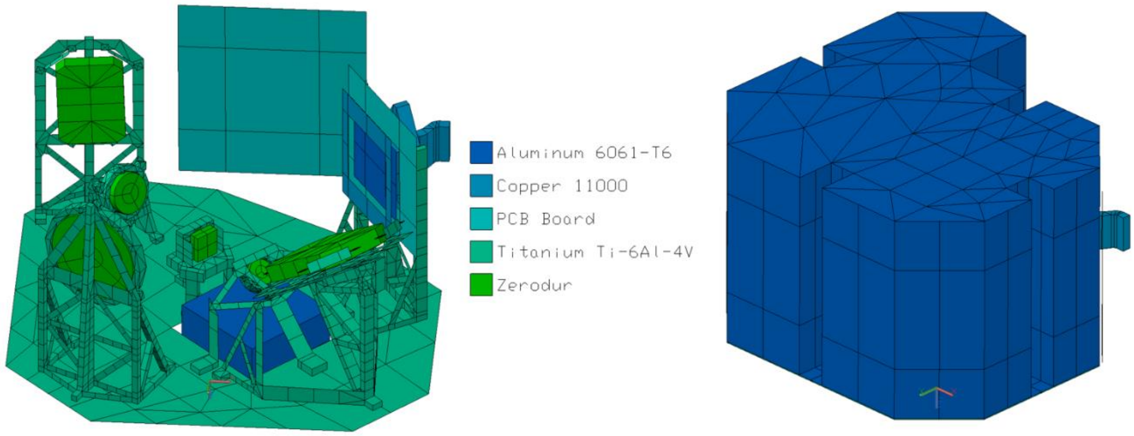

Thermo-physical and optical properties are assigned to both the STRUVE payload and the spacecraft, matching the specifications outlined in the CAD model. Figure 64 illustrates the material assignments for the thermo-physical properties, with detailed properties listed in Table 12. Notably, Invar and carbon fiber are utilized for the telescope components, with carbon fiber employed for the telescope tube and Invar for the

Table 12

Thermophysical Property Values

Name	Conductivity, (W/mK)	Density, kg/m^2	Cp, J/kgK
Aluminum 6061	167.9	2777	961
Carbon Fiber	21	1780	710
Copper 11000	391	8860	385
Epoxy	1	1	1
Fused Quartz	1.5	2210	713
Invar	13	8030	504
PCB Board	80	2000	386
Ti-6Al-4V	7.3	4430	572
Zerodur	1.5	2530	800

secondary mirror mount and the base of the telescope. While the telescope's intricate details are not extensively elaborated upon in this analysis or the CAD model, as it is likely to be supplied by a vendor, the results from the analysis aid in establishing preliminary telescope requirements for STRUVE. Additionally, Figure 65 showcases the optical property assignments, with absorptivity and emissivity values provided in Table 13 for each property. These assignments are crucial for accurately simulating the thermal behavior of the payload and the spacecraft, laying the groundwork for further refinement as the project progresses.

Figure 67

Model Optical Property Assignment

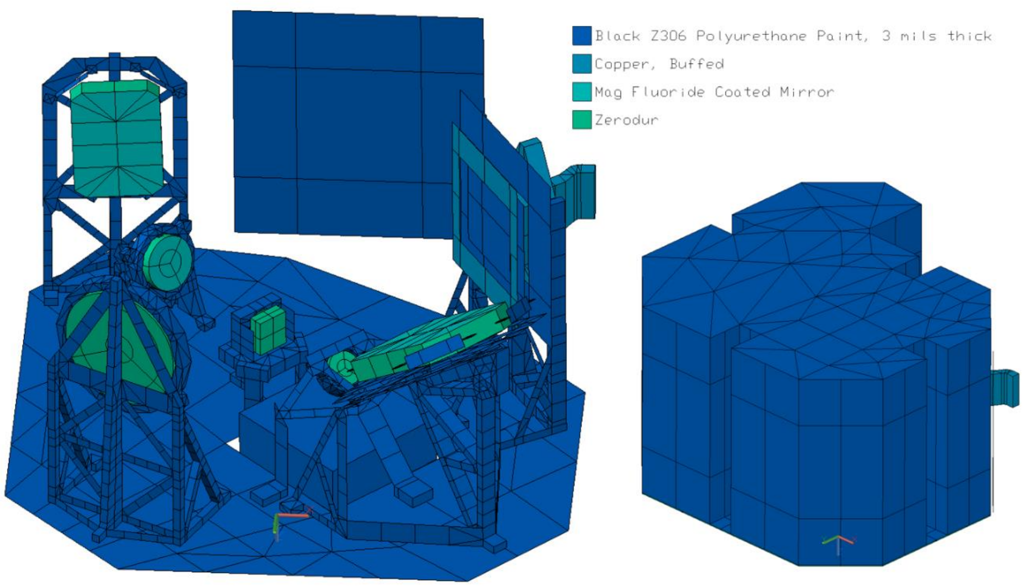

Table 13

Optical Property Values

Name	Absorptivity, α	Emissivity, ε	α/ε
Aluminum, Bare	0.09	0.1	0.9
Aluminum, Anodized Black	0.79	0.86	0.92
Black Z306 Polyurethane Paint, 3 mils thick	0.95	0.87	1.09
Copper, Buffed	0.3	0.03	10
Mag Fluoride Coated Mirror	0.05	0.03	1.67
Optical Solar Reflector, Silvered Fused Silica	0.07	0.8	0.09
S-13 GLO, White Paint	0.19	0.89	0.21
Stainless Steel, Bare	0.47	0.14	3.36
Titanium, Bare	0.4	0.55	0.73
Zerodur	0.15	0.90	0.160

Heat Loads on Instrument

Table 14

Model Heat Loads

Name	Heat Load, W
Detector Board Operating Power	2
Detector Header Board Power	0.3
Modulator Heater Power	3.4

Heat loads are applied to the detector board, detector headboard, and modulator, these heat loads are applied as electronics heat generation. The electronics heat loads in the model are based on spec sheets for the hardware that have been chosen and are used as the nominal values for the coming analysis. The actual power usages for the hardware in our use cases are unknown, so further analysis after the project is funded should have margins added onto the heat loads and adjusted as the project matures.

Heat loads are incorporated into the thermal model to simulate the solar heat loads on the telescope optics. Due to the complexity of accurately calculating heat rates for optics that manipulate incoming light, the telescope is deliberately excluded from the orbital heat rate calculations in Thermal Desktop. Instead, the heat loads on the optics are manually calculated and added to the mirrors. It is assumed that the telescope is directly pointed at the sun for these calculations.

The solar load (Q_{solar}) is calculated using the following equation, where A_x represents the cross-sectional area of the illuminated surface as viewed from the sun, α stand for the absorptivity of the surface, and $\dot{Q}$ denotes the solar flux from the sun, α is the absorptivity of the surface, and $\dot{Q}$ is the solar flux from the sun.

$$Q_{solar} = A_x \alpha \dot{Q} \tag{20}$$

The solar flux from the sun varies throughout the year, ranging between 1322 W/m² to 1414 W/m² (Gilmore, 2002). Figure 66 illustrates the energy distribution of the light entering the telescope through the system. Approximately 83.9% of the light that enters the instrument is reflected out, while 16% is absorbed by the optics, and only 0.003% reaches the instrument. Additionally, the secondary mirror absorbs additional heat from planet shine and sunlight reflected off the Earth's surface (albedo).

High and low total heat loads are calculated in Figure 66 and are utilized in the subsequent analysis sections. It's crucial to establish both hot and cold bounding cases to account for various scenarios in which the system may behave differently, thus understanding whether these scenarios will result in hot or cold conditions. By analyzing all conditions leading to either a cold or hot case, one can identify the worst-case scenarios, although the system is likely to fall somewhere between the extremes.

Figure 68

Telescope Heat Loads

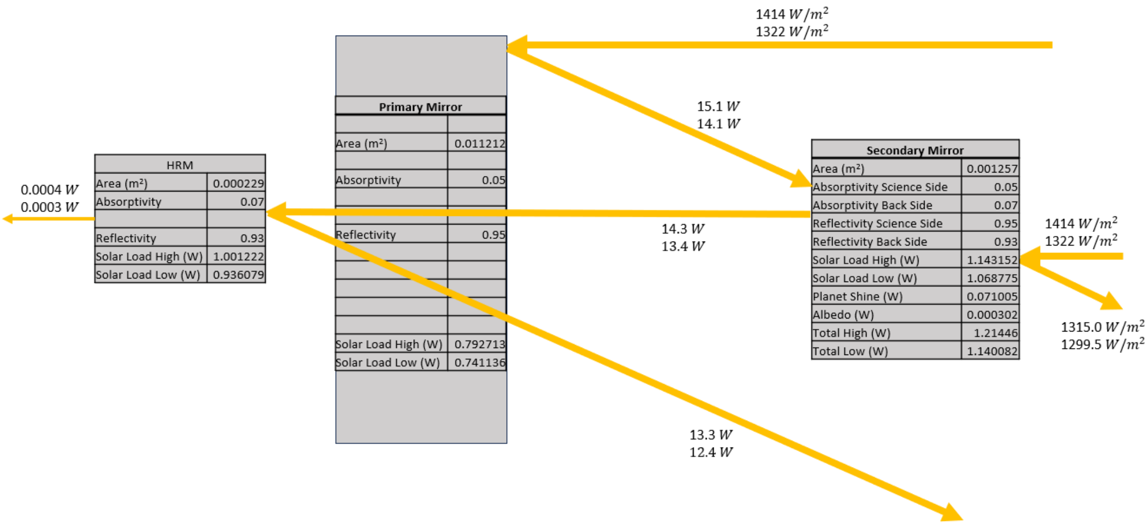

Note. This maps out the energy from the light that reaches the telescope and enters the telescope. Most of the energy is reflected out of the telescope.

Moreover, the duration of the mission can impact the hot and cold cases. For instance, white paint tends to degrade over time due to factors such as UV light, charged particles, and contamination. As the surface degrades, the emissivity generally remains the same, but the absorptivity increases, leading to higher temperatures (Gilmore, 2002). While this analysis is not included in this concept study, it should be considered in the future once funding is secured.

Stead-State Analysis

The STRUVE payload is housed within a 12U CubeSat, where internal temperatures significantly influence its thermal environment. Given the intended sun-synchronous orbit for STRUVE, the spacecraft may approach or reach a thermally steady-state condition, where heat into the system equals heat leaving the system. This analysis seeks to establish upper and lower temperature limits that the STRUVE team may want to impose on the spacecraft provider, thereby providing initial temperature requirements for the spacecraft.

In both the hot and cold steady-state analyses, it's assumed that the payload is operational and continuously observing. The peak power consumption for the modulator, as per specifications, is noted as 3.4 W. The peak power is used for the hot case and half of the peak power is used for the cold case. It should be noted that the modulator peak power is likely a large overestimate of what the nominal operating power will be. Further work should be put into determining what the power needed really is as early as possible as this will affect the thermal performance of the instrument. For the hot case, the temperatures of the spacecraft avionics, chassis, and instrument radiator are set at 30°C, while the solar panels reach 80°C. Conversely, in the cold case, the avionics temperature is set at 0°C, the chassis at 0°C, and the radiator at -20°C. The solar panels primarily impact the chassis temperature, with minimal direct effect on the instrument. These temperature settings are chosen to establish an operating range for the spacecraft provider and serve as temperature constraints to enable the vendor to create a suitable thermal environment for the instrument.

The heat map illustrates how heat propagates through the instrument in a hot steady-state scenario, which aligns with a sun-synchronous orbit where the CubeSat is consistently exposed to sunlight during each orbit, and the thermal environment undergoes minimal changes similar to a sun-synchronous orbit. Figures 67 and 68 show heat flow maps for the instrument based on the hot and cold steady-state cases run. Heat flow values smaller than 0.1W were omitted from the diagrams.

Figure 69

Instrument Hot Case Steady-State Heat Flow Map

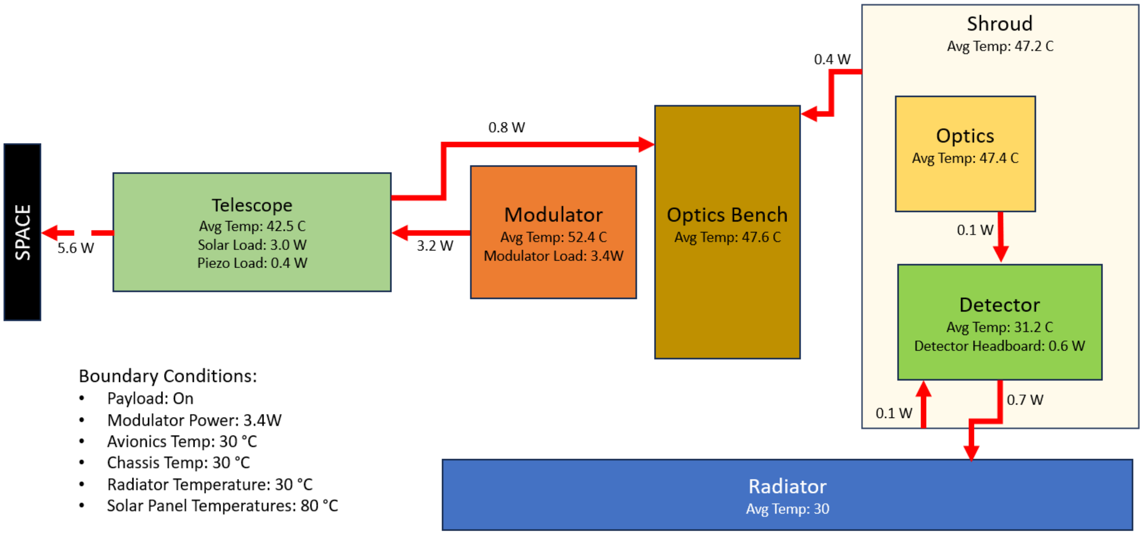

Note. Small heat flows smaller than 0.1W were omitted from the diagram.

Figure 70

Instrument Cold Case Steady-State Heat Flow Map

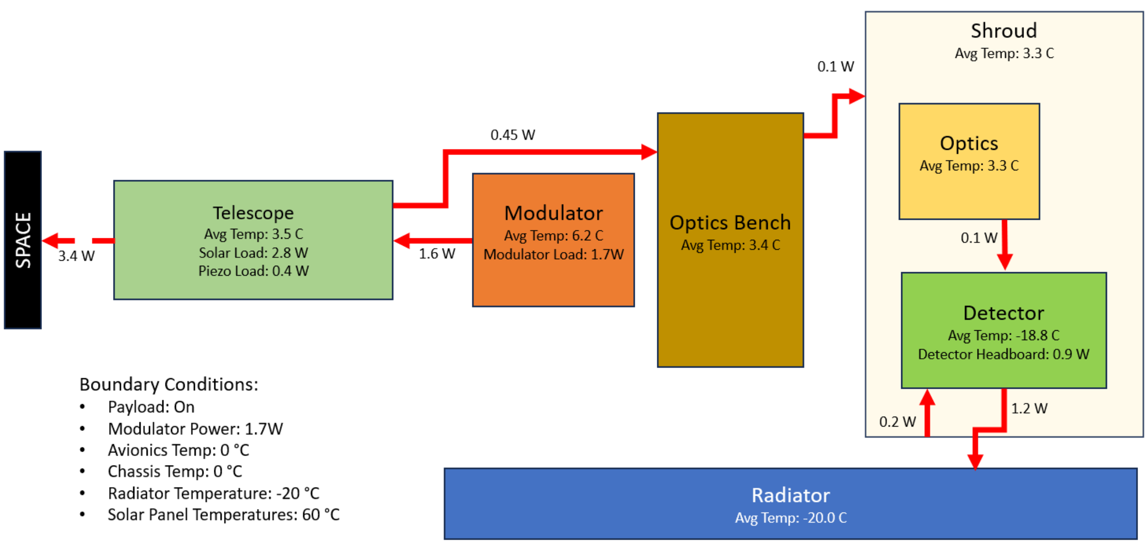

Note. Small heat flows smaller than 0.1W were omitted from the diagram.

The hot and cold steady-state cases highlight how the external environment surrounding the instrument within the spacecraft significantly impacts the instrument's resulting temperature. The key distinctions between hot and cold cases lie in the environmental temperatures and the heat load generated by the modulator. These findings indicate that the instrument temperatures are predominantly influenced by the spacecraft itself. The instrument is expected to operate a few degrees warmer than the spacecraft, with the degree of temperature elevation primarily dictated by the modulator's power consumption. Understanding the dissipation of power by the modulator is crucial for future planning.

Assuming the instrument is initially aligned and tested at 25°C, it would experience a considerable temperature variation of +/-22°C. This underscores the necessity for the instrument design to accommodate such a wide operating temperature range.

To address this challenge, the instrument design must ensure that performance requirements are met across the entire temperature spectrum. Alternatively, the design could incorporate additional thermal control measures to narrow the temperature range. This transition may involve shifting from a predominantly passive thermal control approach to a more active one, where temperature regulation mechanisms are employed to maintain optimal operating conditions despite external temperature fluctuations.

Given the substantial influence of the spacecraft on the instrument's temperature, initiating discussions with the spacecraft vendor to ascertain confidently achievable temperature ranges becomes imperative. To evaluate the impact of these temperature ranges on optical performance, it would be advantageous to conduct Structural Thermal Optical Performance (STOP) analysis prior to the Preliminary Design Review (PDR) and again before the Critical Design Review (CDR). STOP analysis can be resource-intensive, hence understanding its scheduling and rationale is crucial.

Conducting STOP analysis before the PDR aims to refine temperature range requirements for both the instrument and spacecraft, while also determining permissible optic movements to maintain alignment within acceptable bounds to meet science requirements. Prior to the CDR, STOP analysis seeks to verify that the design meets requirements with acceptable margins.

Transient Analysis

The transient analysis sought to assess the instrument's sensitivity to changes in its thermal environment through several scenarios. Firstly, the impact of activating and deactivating the modulator, identified as the highest-powered component, was examined to determine the time required for the instrument's temperature to stabilize post-changes. Secondly, fluctuations in avionics temperature, often generated by components like the S-band radio, were analyzed for their potential influence on instrument stability. Furthermore, variations in chassis temperature, particularly during eclipses in sun-synchronous orbits (beta angle <67°) or the ISS orbit, were explored to understand their effects. Lastly, the combined effects of solar loads on the telescope and chassis variations were investigated separately to pinpoint their specific impacts on the instrument's thermal behavior.

Modulator Effects

Several scenarios are examined to understand the impact of the modulator on the temperature stability of the system. These scenarios included:

1. Modulator activation at low power (1.4 W)
2. Modulator activation with sustained peak power (3.4W).
3. A 10-minute pulse of the modulator at peak power (at 3.4 W).

All scenarios are evaluated under consistent thermal conditions, with the avionics, chassis, and radiator maintained at 30°C, while the telescope experienced solar loads corresponding to its hot-case conditions.

The goal of this analysis is to determine how large of an effect turning on the modulator has when it is turned on and how long it takes for the temperature to stabilize after being turned on. When the modulator is turned on it takes about 6 hours for the system to stabilize. With the ISS orbit having an orbit period of 93.6 minutes and the sun-synchronous orbit period of 95.6 minutes, it would take close to four orbits from when the modulator is turned on to when the temperatures have stabilized. The detectors experience a relatively small temperature change of 0.6 °C and 0.3°C for the high and low power cases as it is more directly connected to the radiator than anything else due to the thermal straps. The optics are more thermally connected to the modulator and see a larger temperature change of 11°C and 5 °C for the hot and low power cases respectively. This analysis suggests that based on the currently passive thermal control in the system, warm up time would have to be taken into consideration for mission operations. If warm

Figure 71

Instrument Response to Modulator Turn On

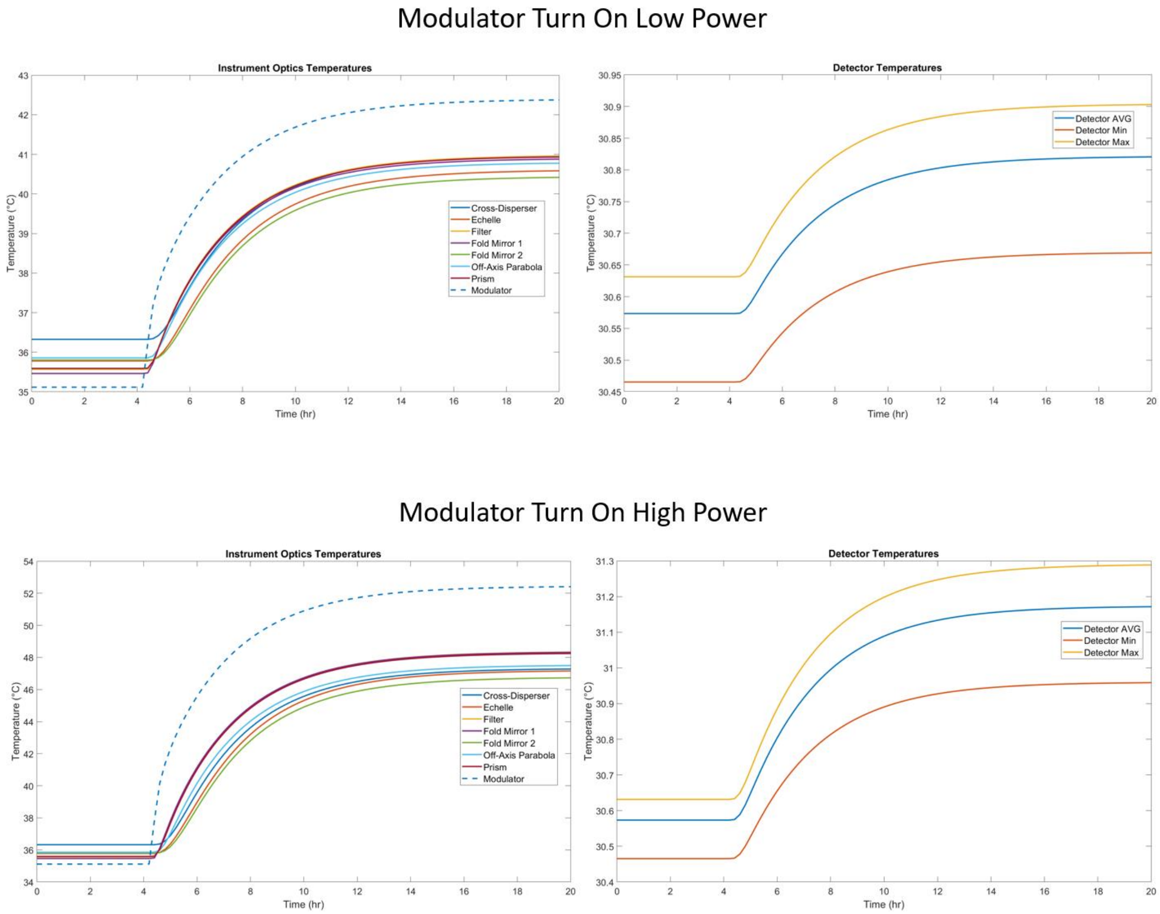

Note. Left is the temperature responses of the optics when the modulator is turned on, right is the detector response. The detector plot has the average, minimum and maximum temperatures.

up time needs to be reduced, the team may want to look into developing a more active thermal control system where the modulator power is replaced by a heater while it is off.

In the subsequent scenario, a 10-minute pulse of the modulator at peak power is examined. As depicted in Figure 70, both the detector and optics demonstrate temperature responses. The detector exhibits a minimal response of less than half a degree, whereas the optics display a temperature response of approximately 0.6°C. While the temperature

Figure 72

Instrument Response to Modulator Pulse

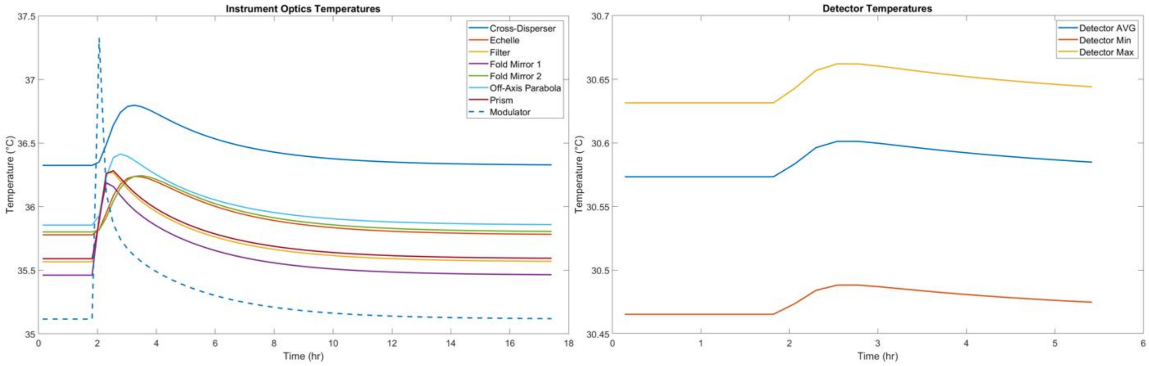

Note. Plots of the temperature over time with a 10-minute impulse from the modulator. Optics temperatures are on the left while the detector temperatures are on the right.

response is relatively minor and is unlikely to significantly impact the system, it is noteworthy that the system recovers within approximately 8 hours.

Avionics, Chassis, and Telescope Environment Variations

The avionics, chassis, and telescope cases examine the impact of periodic environmental disturbances on the thermal environment of the instrument. These analyses are conducted by defining the avionics and chassis as boundary nodes due to limited information about the spacecraft's operational characteristics. This approach allows for the manipulation of the external conditions affecting the instrument. The analysis is based on the ISS orbit, which has an orbital period of 93 minutes and is considered less stable. In the avionics case, the temperature oscillates between 30°C and 50°C periodically. Specifically, the avionics remain at 50°C for 36 minutes before returning to 30°C for 58 minutes. This simulation utilizes a square wave to model the temperature fluctuations of the avionics, representing a worst-case scenario. It assumes that high-power operations,

Figure 73

Avionics Temperature Disturbance Input

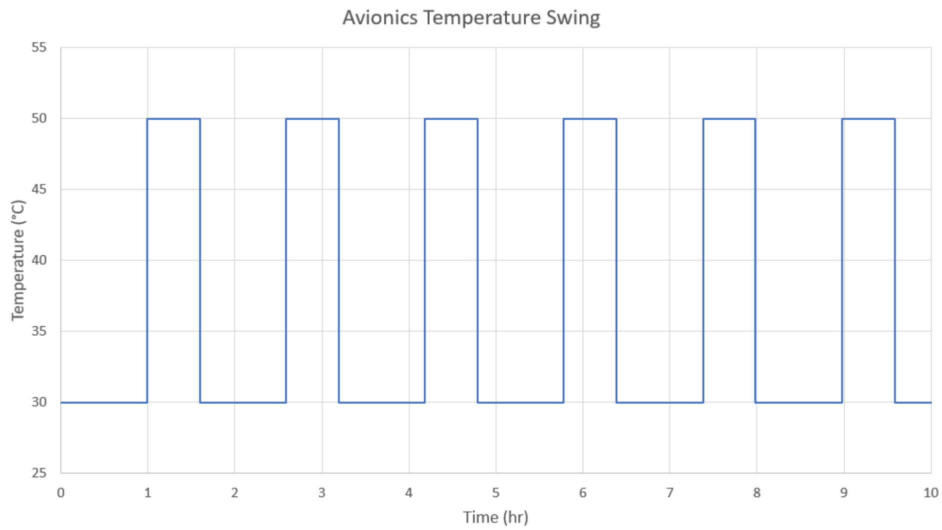

such as S-band transmissions, occur consistently during the 36-minute period of elevated temperature in each orbit, leading to a 20°C temperature change. This swing of 20°C is likely a worst-case scenario for the avionics alone.

The detector exhibits a minimal response of less than 0.05°C, attributable to its thermal connection to the radiator via a thermal strap, with the radiator maintained as a

Figure 74

Instrument Response to Avionics Temperature Swing

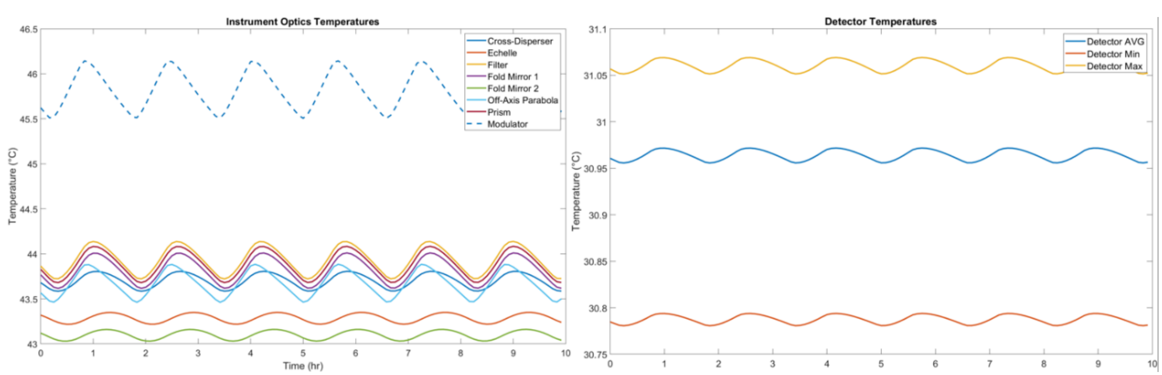

Note. Optics and detector temperature responses to avionics temperature cycling.

steady boundary node. This indicates that the detector, situated within the shroud, can maintain relatively stable temperatures. It's imperative to engage with the vendor early to ascertain the required thermal stability for the detector and devise appropriate measures to ensure the radiator can provide that level of stability. Moreover, the optics experience temperature variations of less than 0.5°C. Due to the relatively low CTE of the mounts and the optics along with the athermal mount, the small temperature variations are unlikely to have large adverse effects on the optics.

In the chassis swing case, the chassis temperature undergoes cycling between 30°C and 0°C, corresponding to the orbital conditions of the ISS. During sunlight exposure (~58 minutes), the chassis maintains 30°C, whereas during eclipse (~36 minutes), it drops to 0°C. Figure 73 illustrates these chassis temperature cycles, utilizing square waves, which may represent a more extreme scenario than actual temperature

Figure 75

Chassis Temperature Disturbance Input

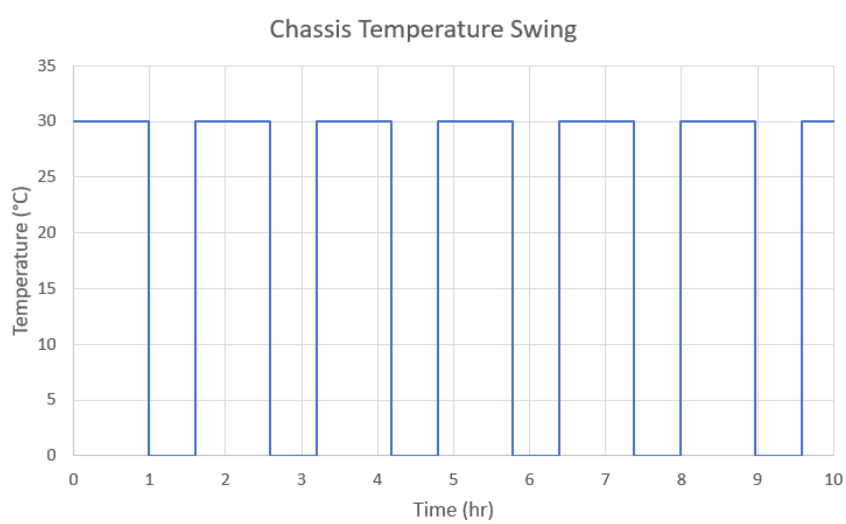

Figure 76

Instrument Response to Chassis Temperature Swing

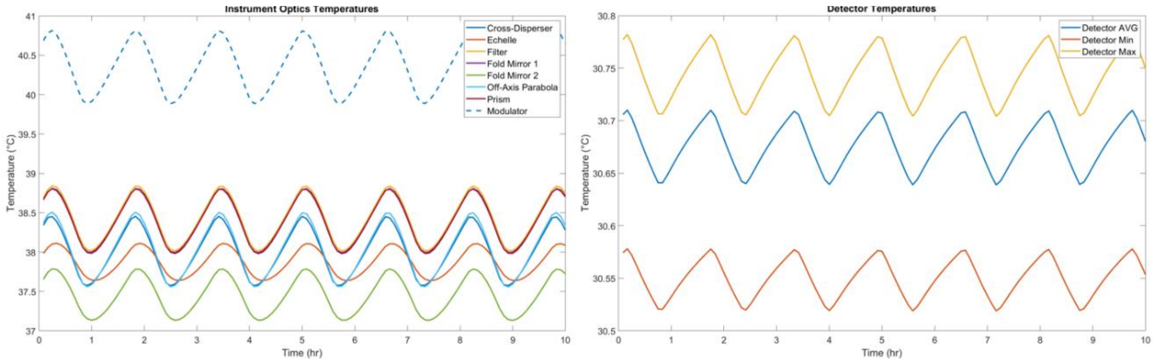

changes but provide a conservative estimate of inducing temperature instability in the instrument. The induced temperature variations of the optics and detector are depicted in Figure 74. The optics experience a change of approximately 0.8°C, while the detector undergoes a minor change of about 0.1°C. These temperature fluctuations are relatively small and unlikely to pose a significant issue. However, it's worth noting that the detector's apparent stability may be influenced by the radiator temperature, which remains constant. The stability of the radiator, in turn, hinges on various factors such as mass, isolation, and orientation. In future work, it will be important to better understand what kind of thermal environment the spacecraft can provide. The worst case hot and cold scenarios should be thoroughly investigated and ensure margin is accounted for to ensure the instrument is being designed for a temperature range that it will really experience in flight. These simulations provide more insight into the stability of the instrument and not the temperatures or temperature range of the instrument as that is high dependent on the spacecraft vendor and the performance they can provide.

The telescope variation analysis involved toggling the environmental loads on and off for the telescope optics based on the spacecraft's solar exposure. During sunlight exposure, the environmental loads are activated, while they are disabled when the spacecraft is not in direct sunlight, except for the planet shine load, which remains active. It's noteworthy that as the planet comes into view of the telescope, the planet shine load increases to approximately 0.25 W at its maximum. The resulting temperature variations for the telescope are depicted in Figure 76. Notably, the secondary mirror undergoes significant temperature swings, ranging from +50°C to -15°C. These substantial temperature variations must be carefully considered by the telescope vendor to ensure the system's thermal insensitivity, preventing image distortion as the temperature fluctuates during transitions out of eclipse. If achieving such thermal stability proves challenging, a

Figure 77

Telescope Temperature Response to Eclipse

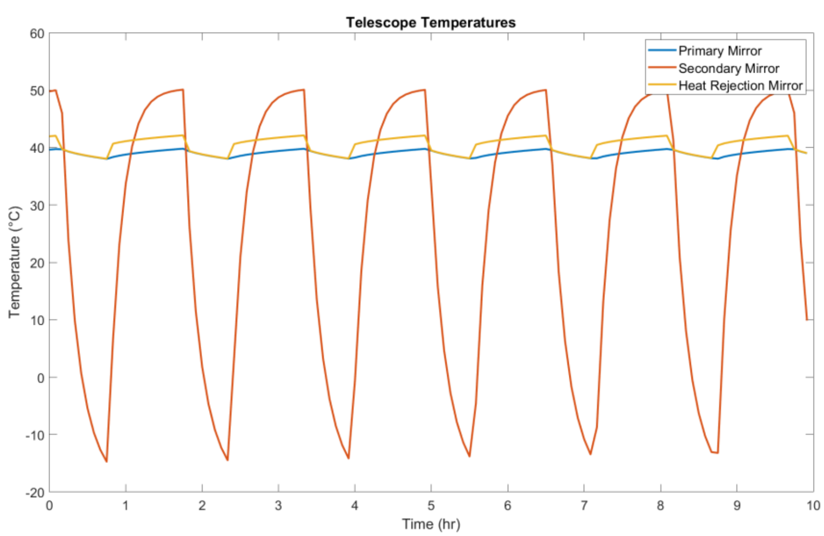

Figure 78

Instrument Response to Telescope Response to Eclipse

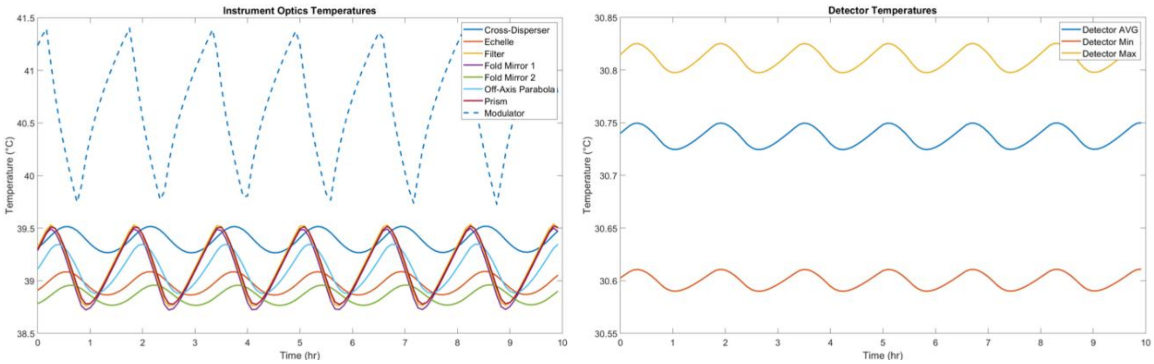

Note. The telescope experiences large temperature swings due to going from looking at the sun to being in eclipse.

more active thermal control approach may be necessary. A passive method for reducing the large temperature swing could be adding more mass or incorporating phase change material into the secondary mirror mounting cell. In contrast, the primary mirror and heat rejection exhibit greater stability, attributed to their larger mass and better conductive paths for heat dissipation. Consequently, the optics within the instrument experience less than a 1°C temperature change, while the detector temperature swing is less than 0.025°C, as illustrated in Figure 76. It is advisable to build the telescope out of thermally insensitive materials such as Zerodur for the optical elements, Invar for the optics cells and perhaps a low CTE carbon fiber material to reduce the mass and keep the rigidity in the telescope.

The final case examined involved combining the chassis temperature swing with the telescope's environmental load variations, providing a more realistic scenario reflecting potential external thermal environmental fluctuations. Figure 77 illustrates the telescope's response, with both the primary and secondary mirrors experiencing notable temperature changes, indicating their dependency on the chassis variations. Ensuring the telescope's thermal insensitivity becomes imperative to avoid resorting to an active thermal control method. The modulator observes a 2°C temperature change, while the remaining optics encounter a temperature swing of approximately 1.5°C, with the detectors experiencing a mere 0.06°C temperature swing. Fortunately, the temperature variations observed in the optics are likely permissible and unlikely to significantly compromise performance.

Figure 79

Telescope Response to Chassis Swing and Eclipse

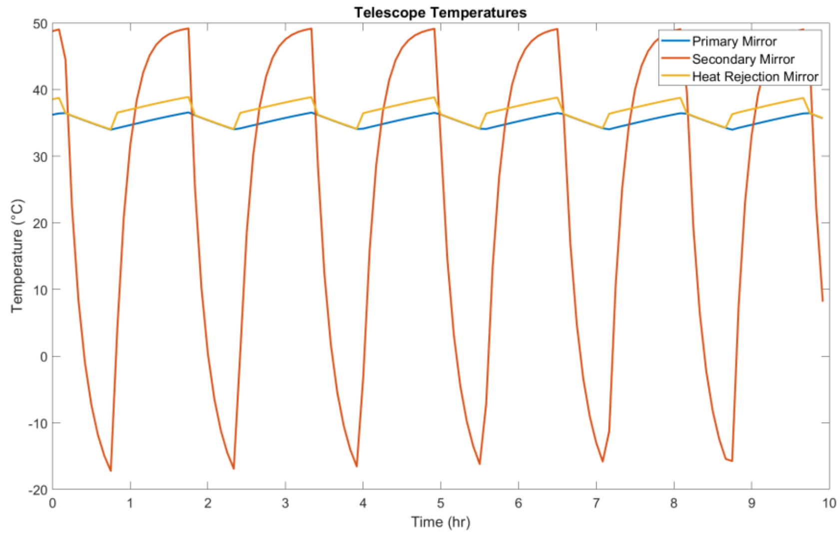

Figure 80

Instrument Response to Chassis Swing and Eclipse

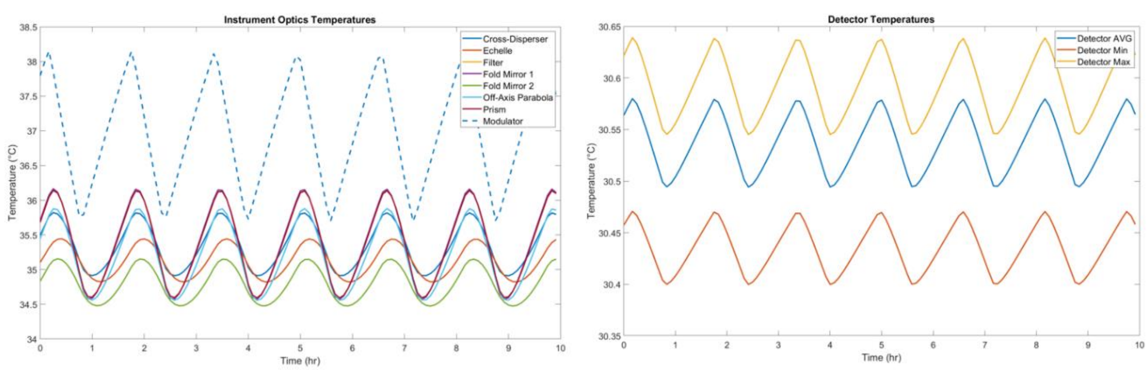

STRUVE Take Aways

The STRUVE instrument holds promise for integration within the 12U CubeSat form factor, highlighting the necessity for early collaboration with spacecraft vendors to discern the thermal conditions achievable for optimal instrument performance. A critical aspect that is not addressed in this work is the mechanical interface between the instrument and spacecraft. This interface, assumed to be well thermally insulated, poses a potential challenge that warrants early attention. A significant thermal conductance through the mounting interface can induce substantial temperature fluctuations in the optics due to avionics and chassis variations.

To mitigate temperature variations originating from the spacecraft, strategic adjustments in spacecraft orientation can optimize thermal management, particularly in sun-synchronous or ISS orbits. If the mass margin allows, adding mass in areas sensitive to thermal swings could help reduce the temperature swings passively. Active thermal control solutions could be used such as heaters to stabilize a component however that comes at a cost to the mission in price, power, and increased risk. Collaborative efforts with spacecraft vendors are pivotal in defining feasible temperature ranges. STOP analysis serves as an indispensable tool in assessing thermal impacts on optical performance.

The significance of STOP analysis is further emphasized by its role in refining temperature range requirements and aligning optic movements with scientific objectives, crucially before PDR and CDR stages. Considering the dynamics of modulator temperature stabilization, which typically takes approximately 10 hours after activation, meticulous planning for observation timing and temperature control mechanisms is imperative. Active thermal control systems present a viable avenue for mitigating modulator warm-up, alongside robust design considerations to uphold performance amidst temperature variations of up to 10°C.

CHAPTER 4

BALLOON-BASED SPECTROMETER MISSION: OPTO-MECHANICAL DESIGN

Figure 81

EXCITE Overview

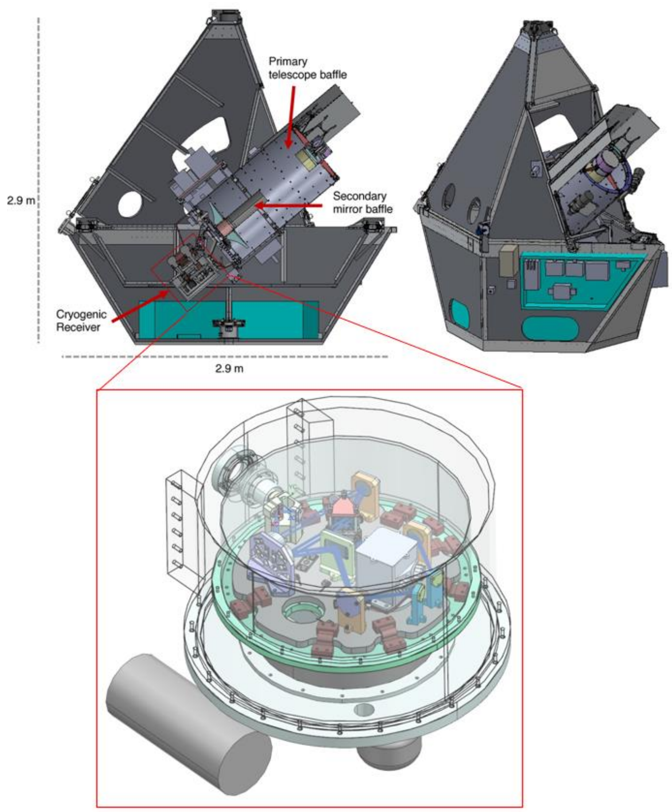

Note. This figure shows where the spectrograph inside the full EXCITE assembly. Note the Dewar has been rotated 180 degrees for this image to have the optics pictured “upright.” The gondola figure is from an SPIE paper by Tim Rehm, “The Design and Development Status of the Cryogenic Receiver for the EXoplanet Climate Infrared Telescope (EXCITE)” (Rehm et al., 2022).

Introduction

The EXCITE mission, a NASA-funded high-altitude balloon endeavor, aims to measure spectrographic phase curves of transiting hot Jupiter-type exoplanets (Nagler et al., 2019). A critical component of this mission is the spectrograph, situated within a dewar affixed to the rear of the telescope, as depicted in Figure 79. Operating at 120K, the spectrograph encounters a substantial temperature change of approximately 173°C. Consequently, detailed attention was paid to material selection and the design of the optics bench and mirror mounts to ensure that the optics remain aligned and that stresses

Figure 82

Spectrograph Top-Down View

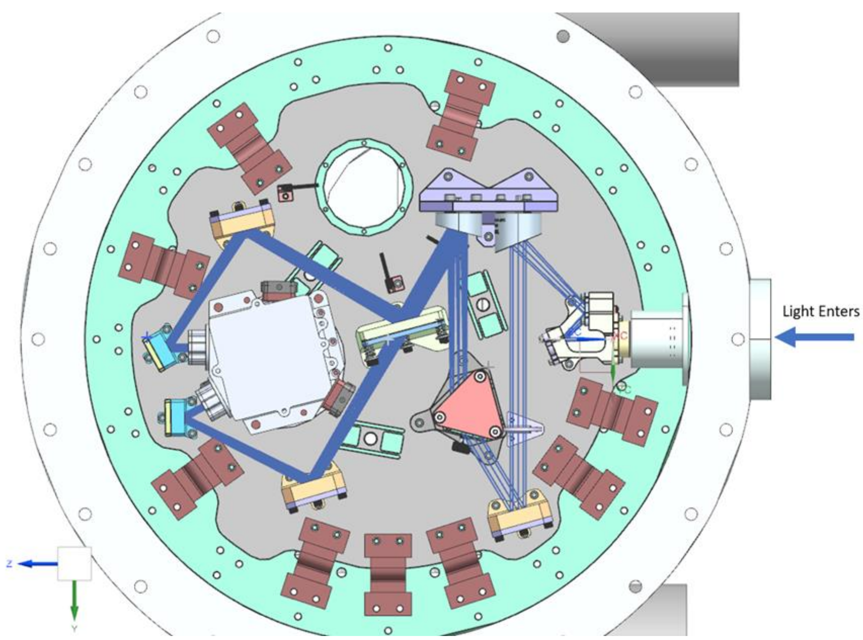

Note. Overview of the instrument, light enters the right side of the image (-Z side of the spectrograph).

arising from the significant temperature variation and interfaces with CTE mismatch do not adversely affect their performance.

The EXCITE spectrograph comprises 12 optics components. Initially, light enters the spectrograph from the telescope, as depicted on the right side of Figure 80, where it is focused at the slit. Subsequently, the light is guided by two fold mirrors to reach the 45-degree off-axis parabola. At this stage, the 45-degree off-axis parabola serves to collimate the beam, after which it passes through a prism and separated by wavelength. Following this, the beam is focused once again, this time using a 30-degree off-axis parabola. Subsequently, a dichroic is used to split the beam, with fold mirrors directing the beam where it is brought to focus onto two distinct regions of the detector.

Two cryocoolers are used to cool the instrument, one cryocooler for the detector and one for the cold plate (Rehm et al., 2022). The cold plate cryocooler cools the optics

Figure 83

EXCITE Instrument Assembly Inside the Dewar

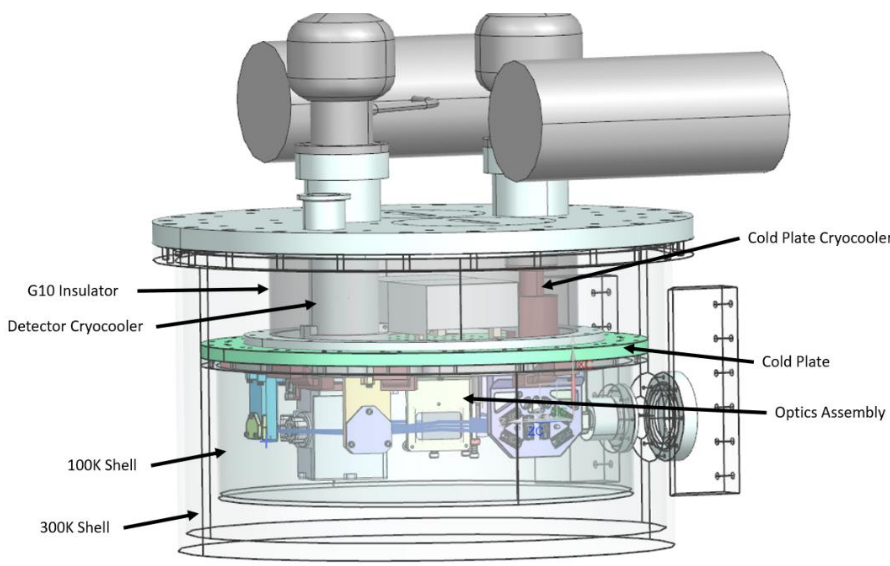

assembly to 120K for nominal operations and the second cools the detector to 50K. The optics assembly is housed inside a 100K shell, the shell serves as a radiative shield to the warmer 300K shell and helps radiatively cool the optics assembly.

Optics Bench

The optics bench provides a stable platform for all optics mounts and interfaces with the dewar's cold plate. Key design requirements for the optics bench include maintaining a beam path length tolerance of 0.77 mm from room temperature to 100 K, along with interfacing seamlessly with both the aluminum cold plate and the optics mounts.

The optics bench is circular in shape with a diameter of 279.4 mm (11 inches) and tailored to accommodate the optics while maximizing the surface area between the cold plate and the bench, all within the confines of the dewar. Originally, the optics bench was conceived using 6061-T6 aluminum, but is later replaced with Ti-6Al-4V titanium due to titanium's substantially lower CTE, which is approximately 61% less than that of aluminum.

To assess the dimensional changes of the optics bench, the linear thermal expansion equation (equation 16) was utilized. This equation, which governs how an object's length changes with temperature variation, was applied to determine the change in length (dL) based on the initial length (L_0), the coefficient of thermal expansion (α),

$$dL = L_0 \alpha dT \tag{21}$$

Figure 84

Optics Bench Overview

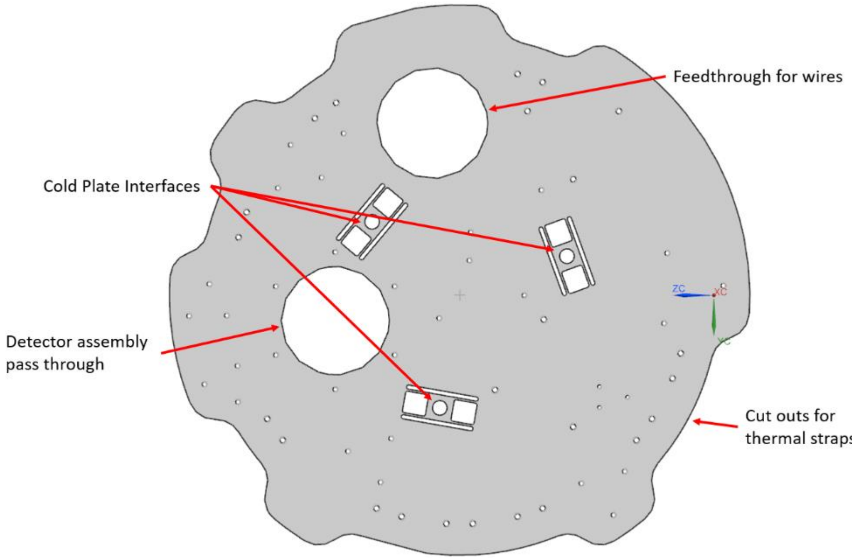

Note. Top-down view of the optics bench. The optics bench contains two pass-through holes, one for the detector assembly and one for the wires. The optics bench interfaces with the dewar cold plate at the three flexures with ¼-20 screws. There are cut outs around the optics bench to create room for thermal straps to connect the outer edge to the cold plate.

and the temperature change (dT). At room temperature, 6061 aluminum exhibits a CTE of 23.6×10^{-6} °C^{-1} (Yoder, 2008). With a temperature change of 193 K, this would lead to a contraction in the diameter of the optics bench by approximately 1.21 mm, consequently shortening the beam path by a similar amount. By contrast, titanium boasts a CTE of 8.8×10^{-6} °C^{-1} (Yoder, 2008), resulting in a diameter contraction of about 0.46 mm when subjected to the same temperature change. This leaves a margin of 0.31 mm, illustrating titanium's ability to better maintain dimensional stability under varying temperature conditions.

The interface between the cold plate and the optics bench is crucial as it serves as the primary means of cooling the optics assembly. However, this interface poses potential challenges due to the substantial CTE mismatch, with the cold plate being made of aluminum. Such a mismatch could result in significant stresses at the interface, leading to warping or even failure. To address this issue, flexures are precisely machined into the titanium optics bench. Strategically positioned around the center of the optics bench, the

Figure 85

Optics Bench Flexure Design

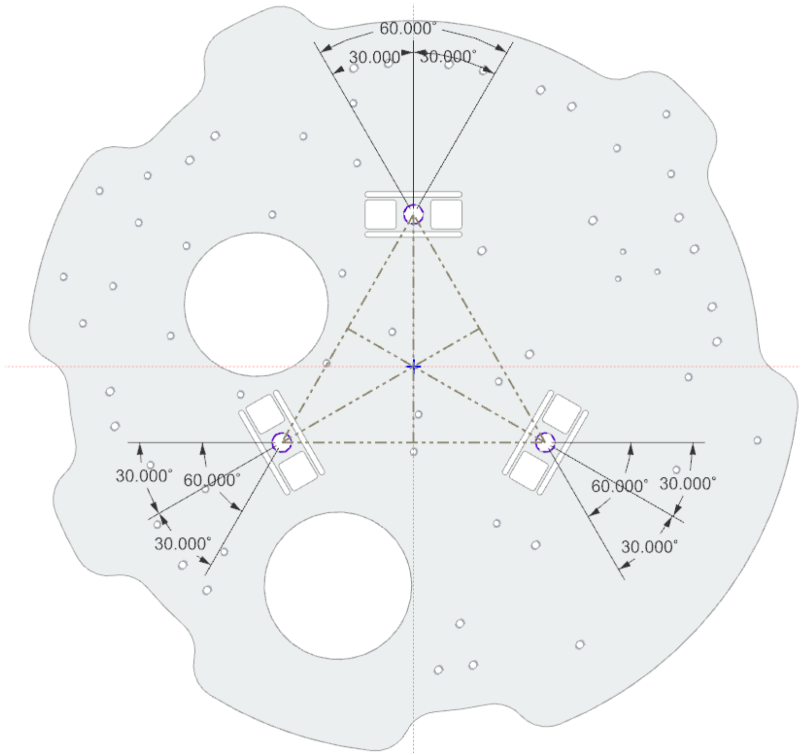

Note. The above figure shows how the flexure centers of the bolt holes make an equilateral triangle. The flexures are oriented perpendicular to the reference line bisecting each corner of the equilateral triangle. The reference lines bisecting the corners intersect at the middle of the optics bench keeping the center of the optics bench stationary during temperature fluctuations.

screw hole centers form an equilateral triangle configuration. Perpendicular to the reference lines bisecting each corner of the triangle, these flexures effectively manage stresses. Their intersection at the optics bench's midpoint ensures stability during temperature fluctuations (as depicted in Figure 83). Additionally, cutouts around the optics bench provide space for thermal straps, allowing for the connection of the optics bench's outer diameter to the cold plate without interfering with the placement of the 100K radiative shell (as illustrated in Figure 82).

Figure 86

Optics Bench Flexure Stress Analysis

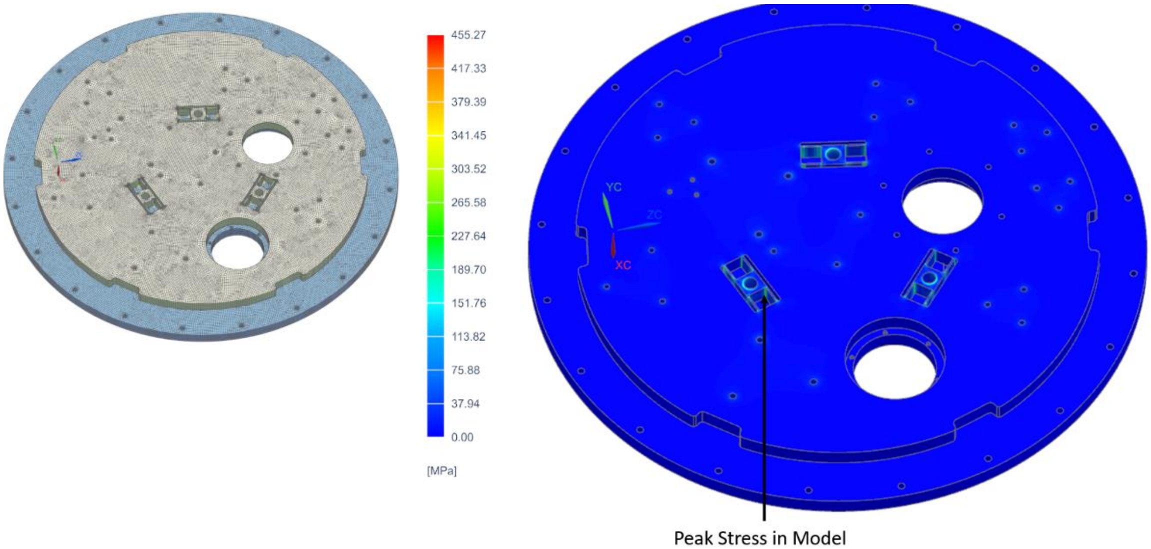

Note. Left is an image of the FEM, right is an image of the results showing peak stress at 455.27 MPa at a joint in the flexure.

The FEM focuses on assessing stress at the interface between the optics bench and cold plate, specifically examining the impact of the mismatched CTE. The model is configured with an initial stress-free temperature of 20°C (293K) and a final settling temperature of -153°C (120K), representative of typical operational conditions for the spectrograph, the analysis revealed a peak stress of 455 MPa at a joint within the flexures. Titanium, the material of the optics bench, possesses a yield strength of 830 MPa and an ultimate yield strength of 900 MPa. In cases where stress exceeds 830 MPa but remains below 900 MPa, the flexures are likely to bend without returning to their nominal position. However, if stress surpasses 900 MPa, the flexures risk catastrophic failure. With a peak stress of 455 MPa, a safety margin of 1.82 is observed, comfortably meeting the minimum requirement of 1.2 for safety margins.

Optics Mounts

Trimount Design

The trimount accommodates the slit and the first two half-inch fold mirrors, designed to minimize relative changes among them. The slit, measuring 0.5 inches in diameter, is mounted within the trimount, featuring a 100-micrometer width and a length of 3 mm. Positioned inside the mount, the slit assembly is supported by a wave spring that applies a preload force, while a retainer secures it in place, serving as the reference surface. With a preload force of 4 pounds, the spring ensures the slit remains in position without inducing excessive stress. Similarly, the second optic is installed with its

Figure 87

Trimount Overview

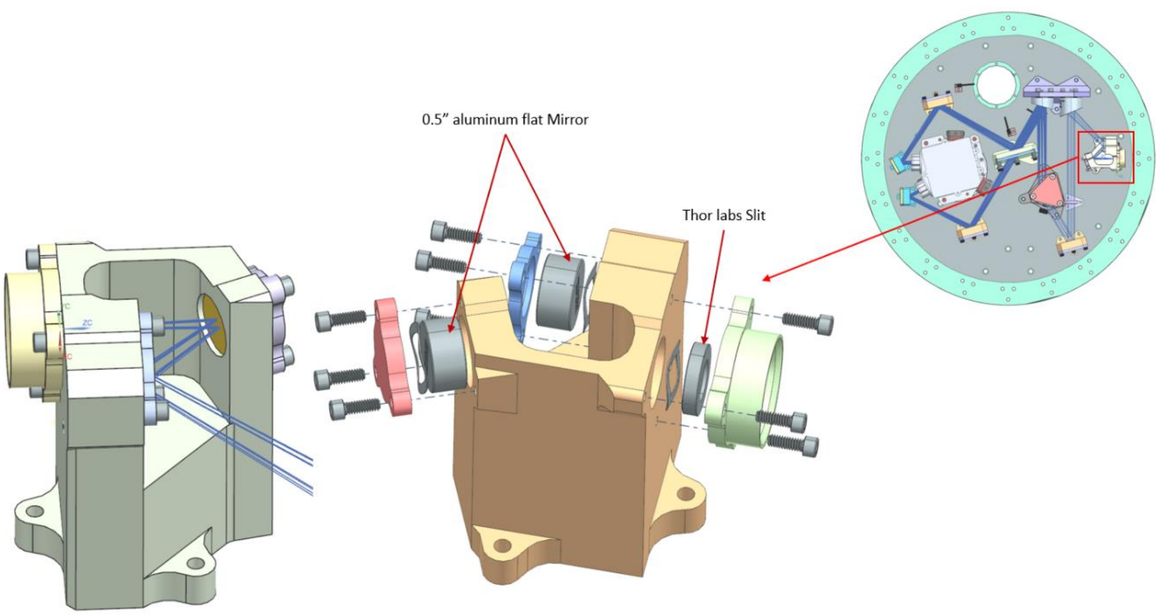

Note. The trimount houses the slit and 2 half inch fold mirrors. The light enters the system through the slit and is reflected off both half inch flat mirrors.

reflective side facing inward, sandwiched between a wave spring and a retaining cap, providing 4 pounds of preload. The inside surface of the mount acts as the reference surface for this optic. The third optic is inserted with its reflective surface facing outward, with a wave spring applying 4 pounds of preload force between the optic and the mount. The retaining cap serves as the reference surface for this mirror, securing it within the mount. The mirrors and slit are made of aluminum stock while the mount is titanium which would result in the optics components contracting more than the mount. This will keep the mount from exerting stress on the optics.

Parabola Mount

The parabola mount accommodates both the 45-degree and 30-degree parabolas on a single surface. A notable challenge arises from the significant mismatch in CTE between the aluminum parabolas and the titanium mount. Off the shelf off-axis parabolas from Thorlabs are chosen due to them being readily available and low cost. Opting for titanium for the mount aims to minimize overall movement of the parabolas as the instrument cools to operating temperatures.

To secure the parabolas to the mount, flexures were designed and machined into the structure, following a similar approach as with the optics bench. Ensuring stability at the center of the parabolas is pivotal to minimizing undesired movement, which is carefully managed with the design of the flexures. Shims are utilized between the mirror and the mount to fine-tune the positioning of the parabolas, while a dowel pin facilitates precise alignment in the mounting location for each parabola. Once the optic is securely

Figure 88

Parabola Mount Overview

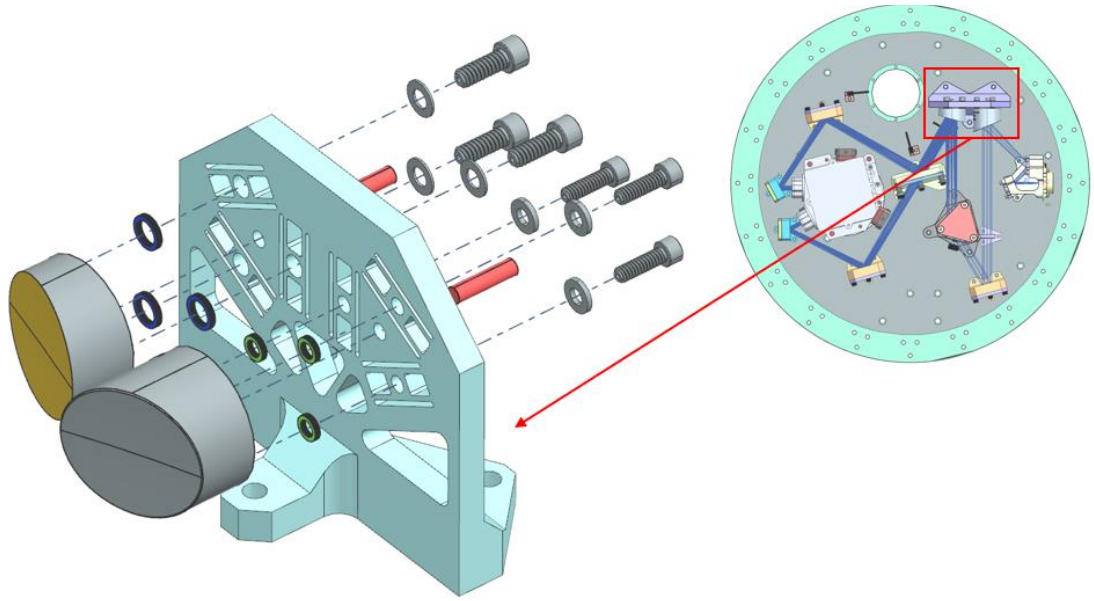

Note. The figure shows an exploded view of the parabola mount. The parabola mount has flexures machined into it to make up for the difference in CTE between the mirrors and the mounts.

fastened in place with screws, the dowel pin is removed, completing the installation process.

A stress analysis is conducted on this mount to verify that the stresses imparted on both the mirrors and the mount remain within acceptable ranges. The assembly starts at room temperature and the stresses of the assembly at 120K are shown in Figure 87. The highest stress observed on the mount was 210 MPa at one of the flexures, resulting in a factor of safety of 3.95, comfortably meeting safety criteria. Regarding the parabolas, the maximum stress point, located on the 45-degree parabola, registered at 68 MPa. Given that the yield strength of 6061-T6 aluminum stands at 276 MPa, with an ultimate yield strength of 310 MPa, the parabolas exhibit a factor of safety of 4, providing ample assurance against potential failures.

Figure 89

Parabola Mount Stress Analysis

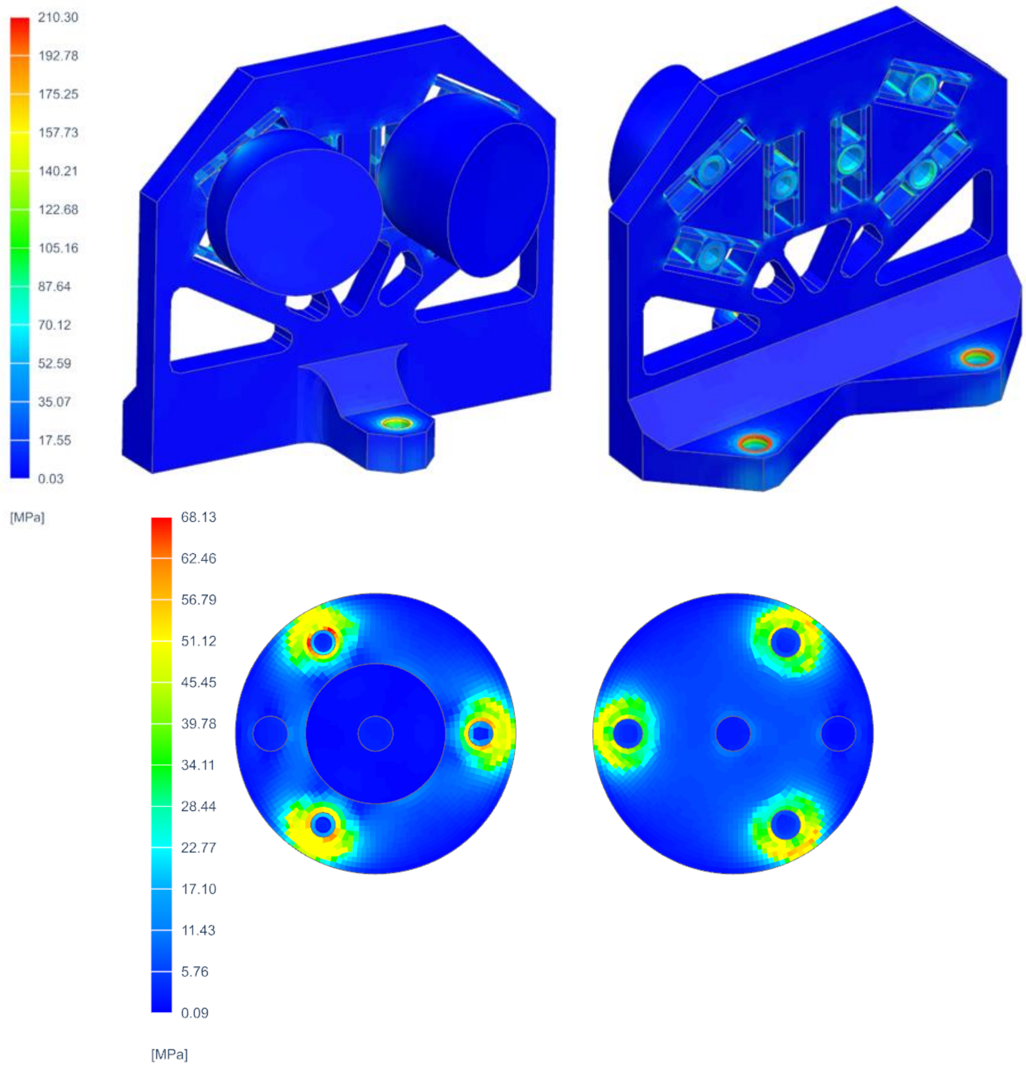

Note. The results from the stress analysis on the parabola mount are seen above. The peak stress is 210 MPa and is found on the titanium flexure. The peak stress on the parabolas is seen around the screw holes with the largest stress being 68 MPa.

Flat Mirror Mounts

The mounts for the half-inch and one-inch flat mirrors employ a similar design approach to that of the trimount for the half-inch mirrors. When installing the half-inch

Figure 90

Flat Mirror Overview

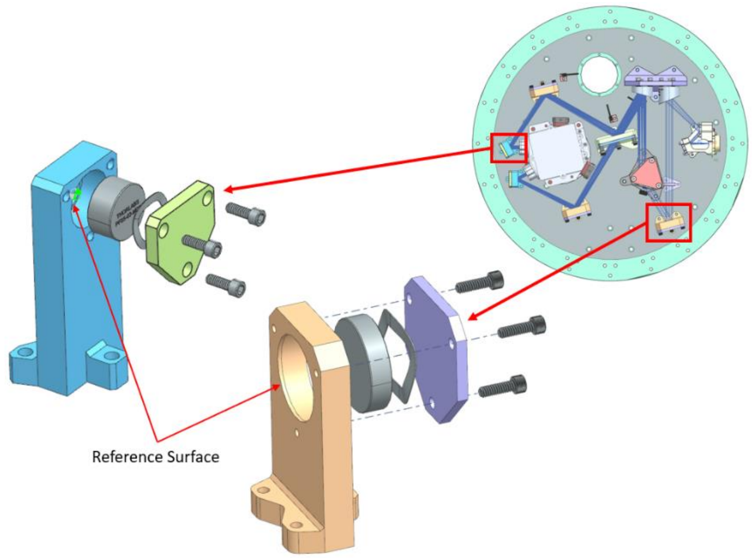

Note. The half inch (left) and 1-inch (right) mounts hold the optics similarly to how the half inch mirrors were held in the trimount.

and one-inch mirrors, they are positioned against a designated reference surface. Subsequently, a circular wave spring is positioned behind the mirror, followed by securing the retaining cap to the back. The wave springs are tailored to provide 4 lbs of preload for the half-inch mirrors and 11 lbs of preload for the one-inch mirrors.

To ensure optimal performance, the mirrors are carefully constrained against the reference surface without being excessively constrained within a cylinder slightly larger than the mirror itself. This setup allows the mirrors a degree of freedom to move slightly across the reference surface. Although this movement may occur, it does not compromise the performance of the mirrors, given their flat nature. This deliberate avoidance of over-constraining the system minimizes stress on the optics, contributing to overall stability and performance.

Semi-Kinematic Prism Mount

The semi-kinematic prism mount constrains all six degrees of freedom without over constraining the prism. The prism mount is a critical component within the optical assembly, tasked with securely housing and positioning the prism while ensuring minimal stress and optimal functionality. With the prism being a delicate optical element, precise engineering and meticulous design considerations are essential to maintain its integrity and performance.

The prism mount design, inspired by principles outlined in "Mounting Optics in Optical Instruments" (Yoder, 2008), adopts a semi-kinematic approach to afford precise control over the prism's positioning without over-constraining its movement. This design strategy balances the need for support without over constraining the prism.

Figure 91

Prism Mount Overview

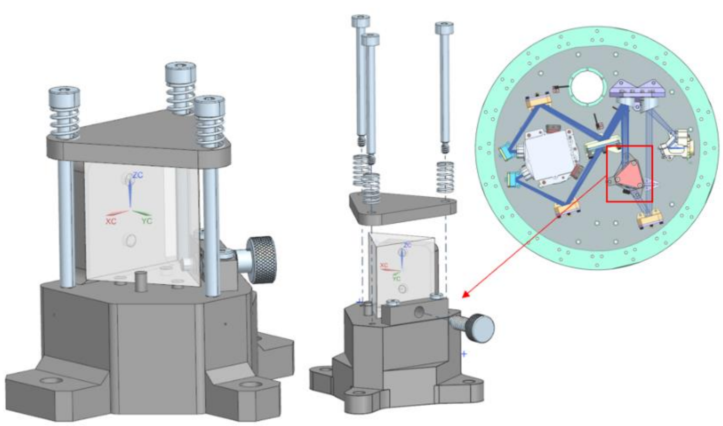

Note. The semi-kinematic prism mount constrains the prism in all 6 degrees of freedom without over constraining the prism.

Strategically positioned pads and pins facilitate control over the prism's movement along various axes. Three pads located on the -Z face define the resting plane for the prism, governing translation along the Z axis and rotation about the X and Y axes. Additionally, two pads on the -Y axis regulate translation along the Y axis and rotation about the Z axis, while a pin on the +X face controls translation along the X axis.

Preload mechanisms ensure the secure fixation of the prism within the mount. The cap provides a preload of 3.4 lbf along the Z axis, achieved through three springs, enabling the prism to withstand forces of up to 37.6 G along this axis. Despite this preload, the stress at the contact area between the mount and prism remains low at 0.27 MPa, well below the material fracture strength of 157 MPa. Additionally, a plunger screw applies a preload of 3 lbf in the X and Y axes, maintaining stability while imposing a stress of 1.98 MPa at the contact area. This preload effectively holds the prism in place and can counteract forces of up to 32 G in the X-Y plane.

The prism mount provides a robust and reliable solution for housing and precisely positioning the prism within the optical assembly, ensuring optimal alignment and stability while maintaining stress levels well within acceptable limits.

Dichroic Mount

The dichroic mount serves to firmly secure the dichroic component within the optical system while allowing controlled movement. Employing a semi-kinematic approach, it ensures precise positioning of the dichroic without overly constraining its mobility. The mount features a reference surface against which the dichroic is positioned. The cutout accommodating the dichroic is deliberately larger than the component itself, preventing stress on the optic during cooling to 120K. This design allows for slight translation of the dichroic across the reference surface without is achieved using three springs, with fasteners compressing them to apply a total preload force of 6.8 lbf.

Figure 92

Dichroic Mount Overview

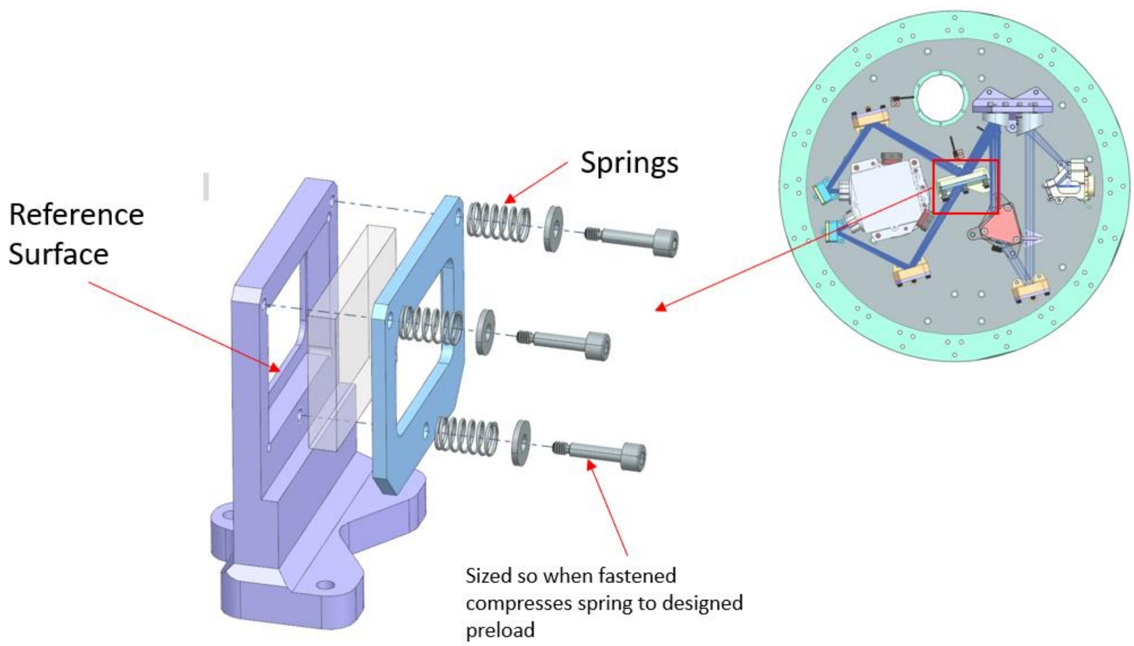

Note. The dichroic mount holds the dichroic against the reference surface of the mount. Springs are used to preload the dichroic against the reference surface.

Assembly Analysis

An assembly FEM is created to analyze the stress distribution within the system. In this FEM, all screws are represented using 1D connectors, with parameters corresponding to 304 stainless steel screws. The material properties utilized in the model are outlined in Table 15. The meshing process is performed individually for each part, ensuring alignment with the CAD model during assembly mapping. Spring forces are applied to preload all optics within the model according to the design specifications. The initial stress-free temperature is set at 20°C (293K), and the system is then cooled to the nominal operating temperature of -153°C (120K).

Figure 93

Spectrograph FEM Overview

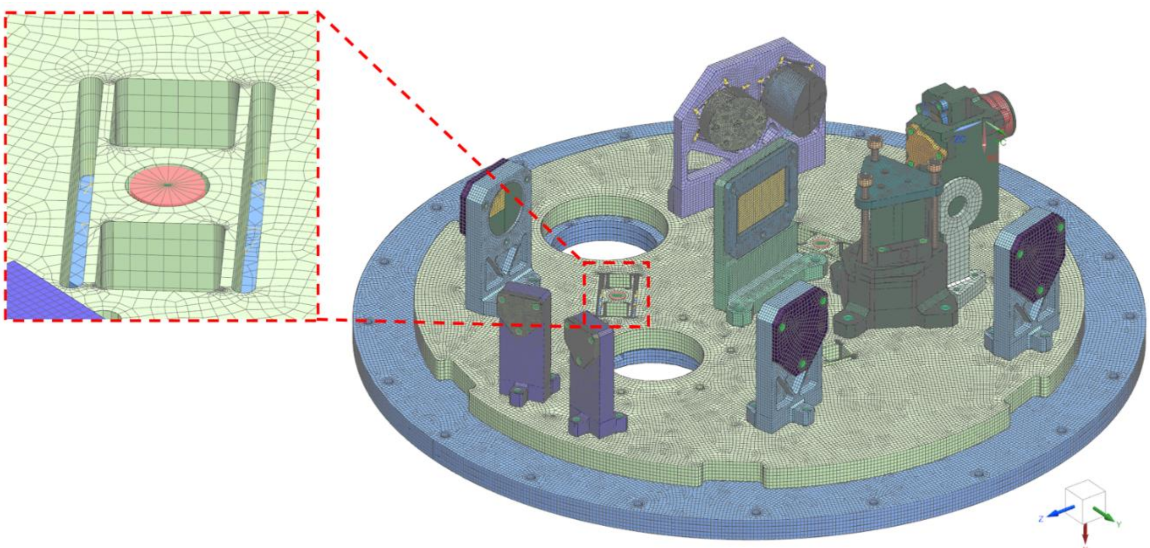

Note. The Assembly FEM model has all optics assemblies mounted to the optics bench. The optics bench is mounted to the cold plate and the cold plate assumed to be able to contract freely towards its center. All bolt connections are modeled using 1D connectors given the bolt or screw parameters.

Table 15

Spectrograph Model Material Properties

Material	Young's Modulus (E), MPA	Poison's Ratio	CTE, °C^{-1}
Aluminum 6061	68980	0.33	2.24E-5
Ti-6Al-4V	121000	0.34	8.60E-6
304 Stainless Steel	190000	0.30	1.66E-5
Calcium Fluoride	76000	0.26	1.84E-9

Note. Table lists the mechanical properties and CTE of the materials in the assembly model. The aluminum is applied to the flat mirrors, slit, parabolas, and cold plate. Titanium is applied to the optics bench and all the mounts. 304 stainless steel is applied to the screws. Calcium fluoride is applied to the prism and the dichroic.

The stress analysis conducted at the assembly level yields results consistent with those predicted at the subassembly level. The highest stress of 455 MPa is observed at the optics bench flexures, maintaining a margin of safety of 1.82. The screwed interfaces on the mounts exhibit a peak stress of 363 MPa, primarily affecting the screws. Given the

Figure 94

Spectrograph Assembly Stress Analysis

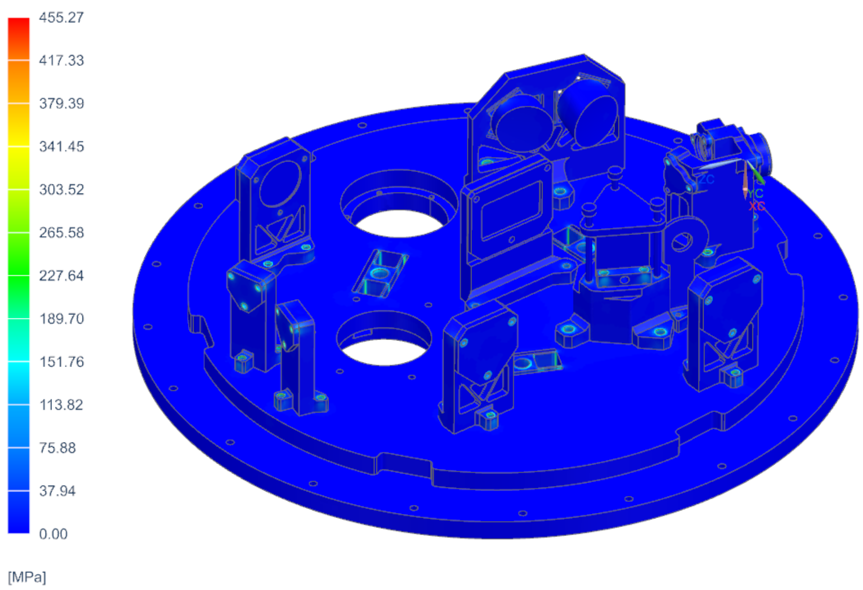

Note. A peak stress of 455 MPa was seen at the flexures. Titanium has a yield strength of 830 MPa leaving a factor of safety of 1.8.

yield strength of 304 stainless steel (600 MPa), a margin of safety of 1.65 is maintained.

Furthermore, a shock analysis is performed to assess the system's ability to withstand the balloon launch, parachute deployment, and landing phases. The shock is not anticipated to exceed a 10 G load. To simulate a 10G random load, a 10 G load is applied along the X, Y, and Z axes of the spectrograph. This analysis confirms that the factor of safety margins remain intact during the 10 G impulse. Figure 93 illustrates the induced stresses on the system from the 10 G load across all three axes, with a peak stress of 38.79 MPa observed at the optics bench flexures. This stress level maintains a substantial factor of safety of 21, ensuring the system's robustness under shock conditions.

Figure 95

Shock Analysis Results

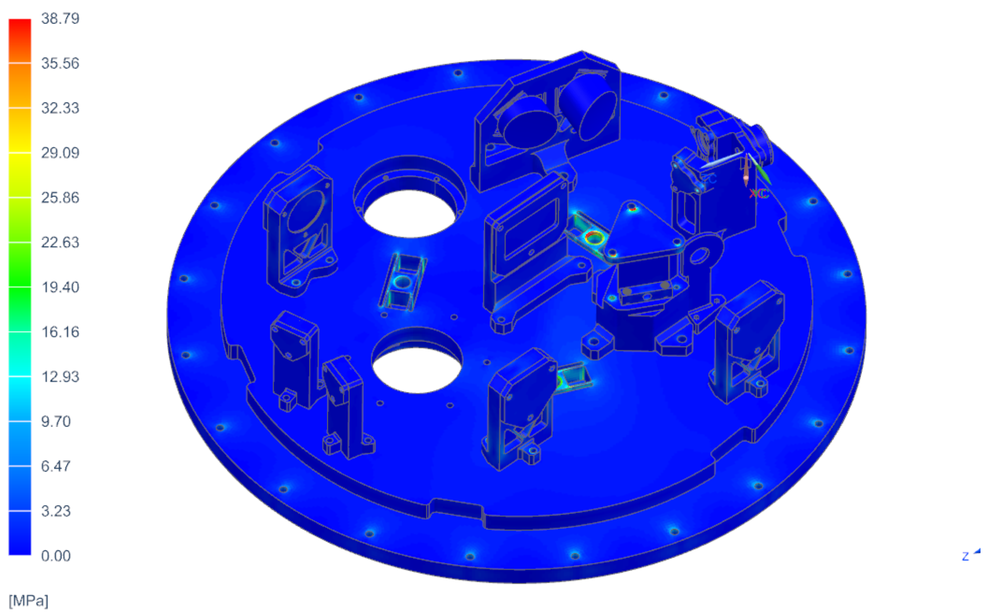

Note. A 10 G load was applied to all three axis in the model. The peak stress was found around one of the screw interfaces for the optics bench and the cold plate.

EXCITE Summary

The design of the EXCITE spectrograph went through many iterations with different arrangements of the optics, material choices and methods to deal with interfaces with large CTE mismatches. In the end a design was found that minimizes stresses as the system is cooled to 120 K while maintaining the position of the optics within tolerance to maintain alignment. It was important to talk to the machine shop early about the design for machineability. Some minor changes were needed in the design for the system to be made but it was caught early enough the changes were able to be incorporated into all the analysis that was done.

CHAPTER 5

REFLECTIONS AND INSIGHTS: CONCLUDING THOUGHTS ON SPARCS, STRUVE, AND EXCITE

Overview

A systems engineering approach focuses on a multidisciplinary perspective to manage and coordinate technical aspects within complex engineering projects. This dissertation applies this approach to three separate projects which are all in different phases in the NASA mission life cycle. The work for SPARCS was directed to prepare and help work through Phase D, the assembly integration and testing of the payload. The work for STRUVE is in Pre-Phase A as it is early in its mission formulation and a concept study. The work for EXCITE took place during Phase B and C as the preliminary design and the final design was finalized for fabrication of the spectrograph. Results from this work include the implementation of thermal control, optic mechanics, and thermal analysis, demonstrating a multidisciplinary skillset for a systems engineer.

One of the most significant lessons I've learned in my time working on these projects is the importance of documenting our work. It may seem like an additional task, but effective documentation serves multiple purposes that greatly benefit the project and the team.

Good documentation helps ensure valuable information about project decisions, methodologies, and outcomes are preserved. This knowledge transfer is essential for maintaining continuity, especially when team members transition or new members join the project. By documenting our work, we ensure that critical information isn't lost when team members move on to other projects.

Documentation also serves as a means of quality assurance. By documenting our work, we create a record of the decisions and actions enabling ourselves and the team to review and verify the accuracy and integrity of our work. This helps maintain a high standard of quality and also provides a basis for continuous improvement by identifying areas for improvement.

Clear documentation supports effective communication and collaboration within the team and with stakeholders. It helps ensure everyone is on the same page, minimizes misunderstandings and helps find any discrepancies. It also enables project management and other team members to provide oversight and guidance, leveraging their expertise to identify potential issues and offer valuable insight.

While creating documentation may initially seem like an additional time investment, it ultimately pays dividends and saves time and effort in the long run. The benefit of good documentation extends beyond the project completion by contributing to the development of a knowledge base, fostering a culture of accountability and transparency, and ultimately delivering a better product. The importance of documentation cannot be overstated. It is a fundamental practice that underscores the success of engineering projects.

SPARCS Concluding Remarks

Testing SPARCS presents a significant challenge due to the high contamination sensitivity of its FUV instrument. To meet the stringent contamination control requirements, a custom testing apparatus was necessary, as testing at a commercial facility proved financially impractical due to the costs associated with chamber rental for decontamination and testing periods. Consequently, a compact TVAC chamber was developed specifically for SPARCS and CubeSat testing, catering to the need for a clean vacuum environment, bake-out capabilities, and contamination monitoring. Additionally, mechanical ground support hardware was meticulously crafted to facilitate the assembly and testing of SPARCS.

While the chamber and test hardware have performed well, refinements to the design were considered during assembly testing to enhance system performance. The existing TVAC chamber boasts a robust heating and cooling system; however, cold testing necessitates cooling the platen, resulting in the chilling of all components mounted on it. This poses challenges when certain hardware components perform optimally at room temperature and do not require cooling, such as the test optics system. To address this, the implementation of additional liquid/gas feedthroughs into the chamber, coupled with the integration of localized heat exchangers in areas requiring cooling, could prove beneficial. By modifying existing large feedthroughs using a Tee or cross flange configuration, the chamber can accommodate more targeted cooling, simplifying the design of test fixtures subjected to significant temperature changes or gradients.

STRUVE Concluding Remarks

STRUVE is currently in the early stages of its mission life cycle and has received funding for a concept study through the NASA H-FOS program. This study addressed various aspects of the mission to demonstrate its feasibility. Specifically, this dissertation contributes to the advancement of the thermal system and optomechanical approaches for securing the optics within the instrument.

Exploration of the thermal environment of both the spacecraft and instrument revealed promising findings. It was determined that the external thermal environment of the spacecraft could serve as stable heat sinks for an instrument radiator, regardless of whether the spacecraft is in the preferred sun-synchronous orbit or in an ISS like orbit, considering the spacecraft's orientation. Additionally, various factors influencing the thermal stability of the instrument were examined, with the modulator identified as a major driver of temperature stability.

Looking ahead, the STRUVE team must prioritize identifying and working with the spacecraft vendor to gain a comprehensive understanding of the system and its operational requirements. The spacecraft's characteristics will significantly impact the upper and lower operating temperatures of the instrument. Currently, the thermal analysis conducted in this concept study lacks detailed information about the spacecraft, resulting in a simplified analysis. Early development of the mechanical interface between the spacecraft and instrument is crucial, as it will greatly influence the mechanical stability of the instrument and the heat flow path from the spacecraft to the instrument, potentially magnifying the effects of temperature changes on thermal stability.

Given the significant impact of the modulator on thermal instability, future efforts should focus on gaining a deeper understanding of its heat dissipation and operational characteristics early in the project. An active thermal design could be implemented to enhance thermal stability where necessary, although it would introduce complexity to the system, necessitating control and power considerations. Furthermore, designing the optomechanical system to be predominantly athermal could expand the operating temperature range and reduce the instrument's sensitivity to temperature fluctuations.

EXCITE Concluding Remarks

EXCITE is a balloon mission featuring a near-infrared spectrograph operating at 120K on the rear of a telescope. A critical aspect of the EXCITE mission was ensuring a stable optics assembly that maintained the beam path length within a change of less than 0.77 mm. To achieve this, materials were meticulously selected for the optomechanical system with low CTE, resulting in an anticipated change of about 0.46 mm, leaving a considerable margin for stability. However, this decision led to a significant CTE mismatch at the interface between the optics bench and the cold plate, as well as some of the optics themselves.

To address this challenge, flexures were intricately designed to constrain the optics bench to the cold plate while allowing for slight independent movement between the two plates in response to temperature fluctuations, thereby preventing catastrophic failures. A similar approach was adopted for the parabola mounts, which also exhibited a substantial CTE mismatch.

The fabrication of the EXCITE optics bench and mounts was successfully completed at the ASU machine shop and subsequently handed over to the assembly integration and testing team. Following this, the spectrograph underwent alignment and integration into the dewar, undergoing successful cold cycling. Currently, EXCITE awaits a test launch scheduled for the summer of 2024.

Figure 96

Delivered EXCITE Spectrograph Assembly

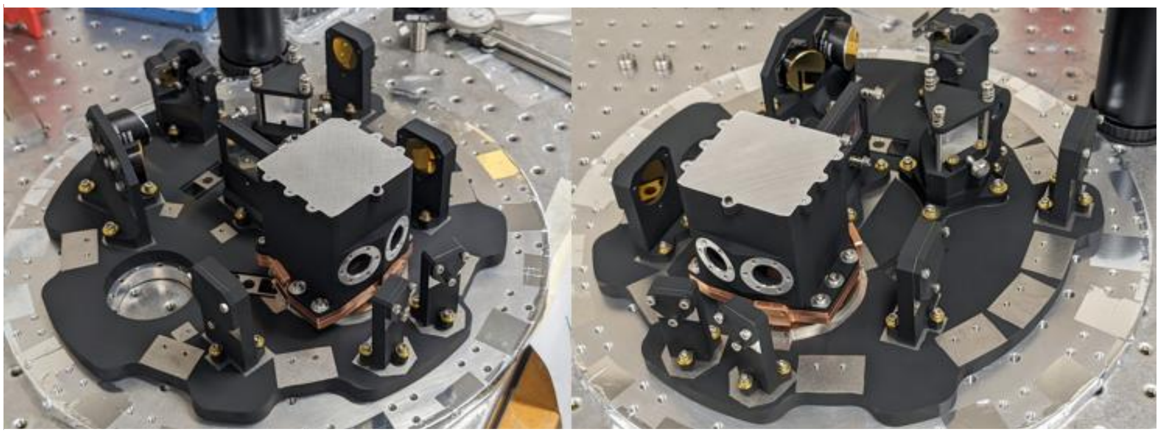

Note. View of the fully assembled spectrograph optics assembly on the optics bench assembled and aligned by Lee Bernard.

REFERENCES

12u satellite - Space Inventor. (n.d.). Space-Inventor. https://space-inventor.com/satellites/12u-satellite/

Ardila, D. R., Shkolnik, E., Scowen, P., Jewell, A., Nikzad, S., Bowman, J., Fitzgerald, M., Jacobs, D., Spittler, C., Barman, T., Peackock, S., Beasley, M., Gorgian, V., Llama, J., Meadows, V., Swain, M., & Zellem, R. (2018). *The Star-Planet Activity Research CubeSat (SPARCS): A Mission to Understand the Impact of Stars in Exoplanets*.

Bernard, L., Jensen, L., Gamaunt, J., Butler, N., Bocchieri, A., Changeat, Q., D'Alessandro, A., Edwards, B., Gong, Q., Hartley, J., Helson, K., Kelly, D., Klangboonkrong, K., Kleyheeg, A., Lewis, N., Li, S., Line, M., Maher, S., McClelland, R., … Waldman, I. (2022). *Design and testing of a low-resolution NIR spectrograph for the EXoplanet Climate Infrared TElescope*. https://doi.org/10.1117/12.2629717

Berner, A., de Wijn, A., Krabbe Jepsen, M., Scowen, P., Gamaunt, J., & Woodruff, R. A. (2022). *Solar transition region ultraviolet explorer (STRUVE) pointing performance modeling*. https://doi.org/10.1117/12.2630789

California Polytechnic State University. (2022). Cubesat Design Specification Rev 14.1. *The CubeSat Program, Cal Poly SLO, 8651*(February).

Cengel, Y. A., & Ghajar, A. J. (2020). Heat and Mass Transfer: Fundamentals and Applications, Fifth Edition. In *news.ge*.

Gamaunt, J., Berner, A., de Wijn, A., Scowen, P., & Woodruff, R. A. (2022). *Solar transition region ultraviolet explorer (STRUVE) requirements flow down to design*. https://doi.org/10.1117/12.2630386

Gilmore, D. (2002). Spacecraft Thermal Control Handbook, Volume I: Fundamental Technologies. In *Spacecraft Thermal Control Handbook, Volume I: Fundamental Technologies*. https://doi.org/10.2514/4.989117

Hale, L. C., & Slocum, A. H. (2001). Optimal design techniques for kinematic couplings. *Precision Engineering*, *25*(2). https://doi.org/10.1016/S0141-6359(00)00066-0

Herbert, J. J. (2006). Techniques for deriving optimal bondlines for athermal bonded mounts. *SPIE Proceedings*. https://doi.org/10.1117/12.680828

Jensen, L., Gamaunt, J., Scowen, P., Beasley, M., Austin, J., Veach, T. J., Shkolnik, E., Struebel, N., Jacobs, D., Bowman, J., & Ramiaramanantsoa, T. (2022). *Star-planet* *activity research CubeSat (SPARCS) science payload assembly, integration, and testing plan*. https://doi.org/10.1117/12.2629562

Jewell, A. D., Hennessy, J., Jones, T., Cheng, S., Carver, A., Ardila, D., Shkolnik, E., Hoenk, M. E., & Nikzad, S. (2018). *Ultraviolet detectors for astrophysics missions: a case study with the star-planet activity research cubesat (SPARC).* https://doi.org/10.1117/12.2312972

Kinematic Encyclopedia. (n.d.). Www.precisionballs.com. Retrieved January 17, 2023, from https://www.precisionballs.com/KINEMATIC_ENCYCLOPEDIA.php#k1

Lambert, M. A., Marotta, E. E., & Fletcher, L. S. (1995). The thermal contact conductance of hard and soft coat anodized aluminum. *Journal of Heat Transfer*, *117*(2). https://doi.org/10.1115/1.2822516

Llis. (1999, February 1). Llis.nasa.gov. https://llis.nasa.gov/lesson/670

Modest, M. F. (2013). *Radiative heat transfer* (3rd ed.). Academic Press.

Monti, C. L. (2007). Athermal bonded mounts: Incorporating aspect ratio into a closed-form solution. *SPIE Proceedings*. https://doi.org/10.1117/12.730275

NASA-STD-7002B. (2023). https://standards.nasa.gov/sites/default/files/standards/NASA/B/1/NASA-STD-7002B-w-Change-1.pdf

Nagler, P. C., Edwards, B., Kilpatrick, B., Lewis, N. K., Maxted, P., Barth Netterfield, C., Parmentier, V., Pascale, E., Sarkar, S., Tucker, G. S., & Waldmann, I. (2019). Observing Exoplanets in the Near-Infrared from a High Altitude Balloon Platform. *Journal of Astronomical Instrumentation, 8*(3). https://doi.org/10.1142/S2251171719500119

Nikzad, S., Hoenk, M. E., Greer, F., Jacquot, B., Monacos, S., Jones, T. J., Blacksberg, J., Hamden, E., Schiminovich, D., Martin, C., & Morrissey, P. (2012). Delta-doped electron-multiplied CCD with absolute quantum efficiency over 50% in the near to far ultraviolet range for single photon counting applications. *Applied Optics, 51*(3). https://doi.org/10.1364/AO.51.000365

Powers, C. (2023, January 31). *OG Data View | Outgassing*. Outgassing.nasa.gov. https://outgassing.nasa.gov/outgassing-data-table

Rehm, T., Bernard, L., Bocchieri, A., Butler, N., Changeat, Q., D’Alessandro, A., Edwards, B., Gamaunt, J., Gong, Q., Hartley, J., Helson, K., Jensen, L., Kelly, D. P., Klangboonkrong, K., Kleyheeg, A., Lewis, N., Li, S., Line, M., Maher, S. F., …

Waldmann, I. (2022). *The design and development status of the cryogenic receiver for the EXoplanet Climate Infrared TELescope (EXCITE)*. https://doi.org/10.1117/12.2629588

The Engineering ToolBox (2003). *Aluminum - Radiation Heat Emissivity*. [online] Available at: https://www.engineeringtoolbox.com/radiation-heat-emissivity-aluminum-d_433.html.

The Engineering Tool Box. (2008). *Linear Thermal Expansion*. The Engineering Tool Box. https://www.engineeringtoolbox.com/linear-thermal-expansion-d_1379.html

Thermal Desktop | C&R Technologies. (n.d.). www.crtech.com. https://www.crtech.com/products/thermal-desktop

Welch, J. W. (2006). Comparison of recent satellite flight temperatures with thermal model predictions. *SAE Technical Papers*. https://doi.org/10.4271/2006-01-2278

Yoder, P. R. (2008). Mounting optics in optical instruments: Second edition. In *Mounting Optics in Optical Instruments: Second Edition*. https://doi.org/10.1117/3.785236

APPENDIX A

STRUVE DETAILED THERMAL MODEL CONTACTOR AND CONDUCTOR TABLES

Contactor Descriptions					
Submodel	Description	Thickness, m	Area, m^2	Conductivity, W/mK	Conductance, W/K
Cross_Disperser	Cross Disperser to Flexure, Epoxy 5 mil thick	0.000127	3.82E-5	1	0.3
Cross_Disperser	Cross Disperser to Flexure, Epoxy 5 mil thick	0.000127	3.82E-5	1	0.3
Cross_Disperser	Cross Disperser to Flexure, Epoxy 5 mil thick	0.000127	3.82E-5	1	0.3
Cross_Disperser_Mount	Cross Disperser mount to Flexures, x6 2-56	---	---	---	1.26
Cross_Disperser_Mount	Cross Disperser mount to Flexures, x3 4-40	---	---	---	0.78
Detector	Detector to Header Board, rough estimate	0.01	1.88E-3	1	0.19
Detector	Detector to Thermal Strap, Epoxy 5 mil thick	0.000127	0.000625	1	4.92
Detector_Board	Detector Board to Mount, x3 4-40 Screws	---	---	---	0.78
Detector_Board_Mount	Detector Mount to Optics bench, x3 4-40 screws	---	---	---	0.78
Echelle	Echelle Flexure, 5 mil thick epoxy	0.000127	8.67E-5	1	0.68
Echelle	Echelle Flexure, 5 mil thick epoxy	0.000127	8.67E-5	1	0.68
Echelle	Echelle Flexure, 5 mil thick epoxy	0.000127	8.67E-5	1	0.68
Echelle_Mount	Echelle Cell to Echelle Mount, x3 4-40 Screws	---	---	---	0.78
Echelle_Mount	Echelle Flexures to Cell, x6 4-40 screws	---	---	---	0.156
Echelle_Mount	Echelle Mount to Optics bench, 3x 4-40 screws	---	---	---	0.78
Filter	Filter to Prism Mount, 5 mil thick epoxy	0.000127	5.42E-5	1	0.43
Fold_Mirror_1	Fold Mirror 1 to Cell, 5 mil thick epoxy	0.000127	3.60E-5	1	0.28
Fold_Mirror_1	Fold mirror cell to Mount, 3x 4-40 screws	---	---	---	0.78

Contactor Descriptions					
Submodel	Description	Thickness, m	Area, m^2	Conductivity, W/mK	Conductance, W/K
Fold_Mirror_1_Mount	Fold Mirror Mount to Optics bench, 3x 4-40 Screws	---	---	---	0.78
Fold_Mirror_2	Fold Mirror 2 to Cell, 5 mil thick epoxy	0.000127	3.00E-5	1	0.24
Fold_Mirror_2	Fold mirror cell to Mount, 3x 4-40 screws	---	---	---	0.78
Fold_Mirror_2_Mount	Fold Mirror Mount to Optics bench, 3x 4-40 Screws	---	---	---	0.78
Modulator	Modulator to Telescope, x4 4-40 screws	---	---	---	1.04
OAP_1	OAP to OAP Mount, Epoxy 5 mil thick	0.00127	3.00e-5	1	0.24
OAP_1_Mount	OAP Mount to optics bench, x3 4-40 screws	---	---	---	0.78
OAP_1_Mount	OAP Ring to Mount,	---	---	---	0.63
Prism	Prism to mount, 5 mill epoxy thickness (both sides)	---	---	---	0.049
Prism_Mount	Prism Mount to Optics bench, x3 4-40 Screws	---	---	---	0.78
Shroud	Shroud to Optics bench, x4 10-32 screws	---	---	---	5.28
Shroud_Caps	Shroud Cap to shroud, x8 4-40 screws	---	---	---	2.08
Shroud_Caps	Shroud Cap to Shroud, x8 4-40 screws	---	---	---	2.08
Telescope	Heat Rejection Mirror to Primary, 5 mil Epoxy	0.000127	5.59eE05	1	0.44
Telescope	Primary Mirror to Barrel and Base, 5 mil Epoxy	0.000127	0.0157	1	124
Telescope	Secondary Mirror to Holder, 5 mil Epoxy	0.000127	0.00044	1	3.46
Telescope	Telescope Piezos to Telescope, 5 mil Epoxy	0.000127	0.0088	1	69
Thermal_Strap	Thermal Strap to +X Panel, 8x 4-40 screws	---	---	---	2.08

Conductor Descriptions		
Submodel	Description	Conductance W/K
DETECTOR_BOARD	Detector Board to Shroud, 1X Stand Off	0.02
DETECTOR_BOARD	Detector Board to Shroud, 1X Stand Off	0.02
DETECTOR_BOARD	Detector Board to Shroud, 1X Stand Off	0.02
DETECTOR_BOARD	Detector Board to Shroud, 1X Stand Off	0.02
TELESCOPE	Telescope to Optics bench, 1X 10-32 Screws	1.32
TELESCOPE	Telescope to Optics bench, 1X 10-32 Screws	1.32
TELESCOPE	Telescope to Optics bench, 1X 10-32 Screws	1.32
THERMAL_STRAP	Detector Clamp to Strap, 2-56 Screw Estimate	0.05
THERMAL_STRAP	Detector Clamp to Strap, 2-56 Screw Estimate	0.05
THERMAL_STRAP	Detector Clamp to Strap, 2-56 Screw Estimate	0.05